Document Version
Final published version

Citation (APA)
Sarafraz, A. (2025). *Nonlinear Mechanics of Suspended Ultra-thin Membranes: From Molecular Dynamics to Continuum Mechanics*. [Dissertation (TU Delft), Delft University of Technology]. https://doi.org/10.4233/uuid:339d56a5-1d83-474d-b591-641391f366fb

NONLINEAR MECHANICS OF SUSPENDED ULTRA-THIN MEMBRANES

FROM MOLECULAR DYNAMICS TO CONTINUUM MECHANICS

NONLINEAR MECHANICS OF SUSPENDED ULTRA-THIN MEMBRANES

FROM MOLECULAR DYNAMICS TO CONTINUUM MECHANICS

Dissertation

for the purpose of obtaining the degree of doctor
at Delft University of Technology,
by the authority of the Rector Magnificus Prof.dr.ir. T. H. J. J. van der Hagen,
chair of the Board for Doctorates,
to be defended publicly on,
Thursday 22 May 2025 at 15:00 o'clock

by

Ali SARAFRAZ

Master of Science in Mechanical Engineering - Applied Design,
Amirkabir University of Technology, Iran,
born in Mashhad, Iran.

This dissertation has been approved by the promotors.

Dr. F. Alijani,	Promotor
Prof. dr. P.G. Steeneken,	Promotor

Composition of the doctoral committee:

Rector Magnificus,	chairperson
Prof. dr. P.G. Steeneken,	Delft University of Technology
Dr. F. Alijani,	Delft University of Technology
Independent members:	
Prof. dr. ir. M. Langelaar,	Delft University of Technology
Dr. G.J. Verbiest,	Delft University of Technology
Prof. dr. Y.M. Blanter,	Delft University of Technology
Prof. dr. D. Vella,	University of Oxford, England
Dr. P. Belardinelli,	Polytechnic University of Marche, Italy

Keywords: nanomechanics, continuum mechanics, molecular dynamics, graphene, two-dimensional materials, nonlinear reduced-order modelling, wrinkling, ultra-thin membranes, Stress distribution, mode shapes, resonance frequency, Nonlinear pressure-frequency response, Stress-strain relations, Hooke's law

Printed by: ProefschriftMaken, The Netherlands.

Front An abstract circular ultra-thin membrane full of wrinkles and corrugations.

Back An abstract wave-like response symbolizing resonance time response of a resonator.

ISBN 978-94-6384-778-0

An electronic version of this dissertation is available at
`http://repository.tudelft.nl/`.

Contents

SUMMARY

Ultra-thin drums play a crucial role in sensing applications due to their slender construction and relatively low bending rigidity. These properties render them highly sensitive to external forces. The emergence of graphene and other 2D materials has profoundly impacted the development of these devices, allowing for the creation of exceptionally thin membranes, even as thin as a single atomic layer. However, the extreme thinness of these structures introduces challenges, such as susceptibility to large deformations and nonlinear behaviour, making linear models unsuitable for mechanical analysis.

To fully harness the potential of ultra-thin resonators in practical applications, it is thus essential to comprehend their nonlinear mechanical behaviour thoroughly. Consequently, mathematical modelling and numerical simulations play a pivotal role in studying the nonlinear mechanics governing the motion and resonant behavior of these devices. This doctoral thesis investigates the nonlinear mechanics of ultra-thin membranes. Its primary objective is to develop analytical and numerical methodologies that will facilitate the future design and analysis of these structures for various applications.

In Chapter 1, we establish the groundwork for understanding the mechanics of ultra-thin membranes. Here, we address the root cause of nonlinearities in 2D material membranes and present the mathematical framework required to account for mechanical nonlinearities from the standpoints of continuum mechanics and molecular dynamics.

Using molecular dynamics (MD) simulations, Chapter 2 investigates the effects of wrinkles on the stiffness and stress-strain behaviour of 2D materials. In order to explain their stress-strain response, we analyze their behaviour under bi-axial loading and demonstrate approaches for developing wrinkles by non-uniform stress and defect creation in MD. We demonstrate that ironing out wrinkles is a nonlinear process, and we propose a phenomenological model to explain this geometric nonlinearity, based on experimentally measurable quantities.

Chapter 3 has a critical look at the uniform pre-stress assumption in the modelling of ultra-thin membranes. Here we develop a methodology to extract the non-uniformity of stress distribution in 2D material membranes. The method predicts the in-plane and out-of-plane static deformation accountable for non-uniform stress distribution following an inverse approach that uses the modal analysis response of the membrane as the input. We showcase the approach based on experimentally obtained mode shapes and resonance frequencies of large graphene drums and highlight the importance of non-uniform stress distribution in the dynamics of these membranes.

In our study of ultra-thin drums, a significant concern arises from pressure differentials affecting their surfaces, causing static deformation and increased resonance frequencies. Chapter 4 addresses this issue by developing a predictive model for pressure-frequency responses by accounting for geometric nonlinearity of the drum. We discuss the influence of static deformation due to pressure and high light the importance of midplane stretching as well as resonant modes about deflected configuration for proper modelling of dynamics. Using this model, we analyse experimental pressure-frequency data from ultra-thin polysilicon drums, determining their Young's modulus. Notably, our Young's modulus values closely align with the literature, affirming our model's reliability.

Chapter 5 serves as the concluding section of this thesis, where we consolidate our findings and highlight the main results. In addition to summarizing our conclusions, we provide insights into prospective research directions within the domain of nonlinear mechanics of ultra-thin drums.

SAMENVATTING

Ultra-dunne membranen spelen een cruciale rol in geavanceerde sensorapplicaties vanwege hun slanke constructie en relatief lage buigstijfheid. Deze eigenschappen maken ze zeer gevoelig voor externe krachten. De opkomst van grafeen en andere 2D-materialen heeft een diepgaande invloed gehad op de ontwikkeling van deze apparaten, waardoor het mogelijk werd om uitzonderlijk dunne membranen te creëren, zelfs zo dun als een enkele atoomlaag. Echter, de extreme dunheid van deze structuren brengt uitdagingen met zich mee, zoals een verhoogde gevoeligheid voor grote vervormingen en niet-lineair gedrag, waardoor lineaire modellen ongeschikt zijn voor mechanische analyse.

Om het volledige potentieel van ultra-dunne resonatoren in praktische toepassingen te benutten, is het essentieel om hun niet-lineaire mechanisch gedrag volledig te begrijpen. Wiskundige modellering en numerieke simulaties spelen daarom een cruciale rol in het bestuderen van de niet-lineaire mechanica die de beweging en resonantie van deze apparaten regelt. Dit proefschrift onderzoekt de niet-lineaire mechanica van ultra-dunne membranen. Het belangrijkste doel is om analytische en numerieke methodologieën te ontwikkelen die de toekomstige ontwikkeling en analyse van deze structuren voor diverse toepassingen zullen vergemakkelijken.

In Hoofdstuk 1 leggen we de basis voor het begrijpen van de mechanica van ultra-dunne membranen. Hier bespreken we de oorzaken van niet-lineariteiten in 2D-materiaal membranen en presenteren we het wiskundige kader dat nodig is om mechanische niet-lineariteiten te verklaren vanuit de perspectieven van de continuümmechanica en moleculaire dynamica.

Met behulp van moleculaire dynamica (MD) simulaties onderzoekt Hoofdstuk 2 de effecten van plooien op de stijfheid en de spanning-rekgedrag van 2D-materialen. Om hun spanning-rekgedrag te verklaren, analyseren we hun gedrag onder bi-axiale belasting en demonstreren we benaderingen voor het ontwikkelen van plooien door middel van niet-uniforme spanningen en defectvorming in MD. We tonen aan dat het gladstrijken van plooien een niet-lineair proces is en stellen een fenomenologisch model voor om deze geometrische niet-lineariteit te verklaren, gebaseerd op experimenteel meetbare grootheden.

Hoofdstuk 3 bekijkt kritisch de aanname van uniforme voor-spanning in het modelleren van ultra-dunne membranen. Hier ontwikkelen we een methode om de niet-uniformiteit van spanningsverdeling in 2D-materiaalmembranen te bepalen. De methode voorspelt de in-plane en uit-plane statische vervorming die verantwoordelijk is voor de niet-uniforme spanningsverdeling, door een inverse benadering te gebruiken waarbij de modale responsanalyse van het membraan als input dient. We illustreren de aanpak op basis van experimenteel verkregen modusvormen en resonantiefrequenties van grote grafeen membranen en benadrukken het belang van niet-uniforme spanningsverdeling in de dynamica van deze membranen.

In onze studie van ultra-dunne membranen vormt het drukverschil dat het oppervlak beïnvloedt een belangrijke uitdaging, aangezien dit statische vervormingen en verhoogde resonantiefrequenties veroorzaakt. Hoofdstuk 4 richt zich op dit probleem door een voorspellend model te ontwikkelen voor druk-frequentieresponsen, waarbij rekening wordt gehouden met de geometrische niet-lineariteit van het membraan. We bespreken de invloed van statische vervorming door druk en benadrukken het belang van middellijnrek en resonantiemodi rond de afgebogen configuratie voor een juiste modellering van de dynamica. Met dit model analyseren we experimentele druk-frequentiedata van ultra-dunne polysilicium membranen en bepalen we hun elasticiteitsmodulus (Young's modulus). Opmerkelijk genoeg liggen onze waarden voor de elasticiteitsmodulus dicht bij die in de literatuur, wat de betrouwbaarheid van ons model bevestigt.

Hoofdstuk 5 dient als afsluitende sectie van dit proefschrift, waarin we onze bevindingen consolideren en de belangrijkste resultaten benadrukken. Naast het samenvatten van onze conclusies bieden we inzichten in toekomstige onderzoeksmogelijkheden binnen het domein van niet-lineaire mechanica van ultra-dunne membranen.

1

1

INTRODUCTION

This chapter provides an overview of the research, highlighting its primary objective, which is the development of theoretical frameworks and tools for understanding the nonlinear mechanics of ultra-thin membranes. The discussion begins with the current state-of-the-art on 2D material nanodevices and focuses on the new applications that emerge from using these novel resonators in sensing applications. The chapter thereafter looks into the complexities of mechanical analysis, focusing on the important role of nonlinearity in understanding the behavior of these devices. A comprehensive discussion of the many root causes of nonlinearity is provided. Following that, the theoretical techniques used in this study, namely continuum mechanics and molecular dynamics, are thoroughly discussed. The chapter closes by explaining the thesis structure. This outline highlights the interconnection of numerous parts and chapters, offering an overview of the overall structure of the thesis.

1.1. MECHANICS AND APPLICATIONS OF 2D MATERIALS

In 2004, Geim and Novoselov used mechanical exfoliation to create graphene flakes from bulk graphite [1]. This landmark discovery not only revealed the potential of employing the properties of atomically-thin crystalline materials, but it also set the path for future two-dimensional (2D) material-based innovations. Since then, researchers have discovered a wide range of other 2D materials, including transition metal dichalcogenides (TMD), h-BN, and phosphorene (black phosphorous). This diverse array of 2D materials exhibits a spectrum of physical properties, including graphene's exceptional conductivity, MoS_2's semi-conductivity, and h-BN's insulating characteristics [2, 3].

These materials possess notable attributes, encompassing features like flexibility, lightweight, and ultimate thinness, with some being no thicker than a single atom [4, 5]. Additionally, their remarkably low mass results in high resonance frequencies, rendering them exceptionally sensitive in sensing applications, and their high surface-to-volume ratio renders them responsive to environmental factors. Moreover, the substantial disparity in stiffness between their in-plane and out-of-plane orientations gives rise to distinctive features such as out-of-plane wrinkles and ripples. Researchers have utilized these distinctive properties to develop nanodevices with groundbreaking applications ranging from energy storage and coating [6] to bio- and pressure sensing [7–9].

As research on 2D materials progressed, scientists uncovered subtle physics governing nanostructures, revealing new features not apparent at larger scales. Despite the advantages of their extreme thinness, these structures are susceptible to significant deformations, leading to fast activation of mechanical nonlinearities [10, 11]. This nonlinear aspect poses challenges for engineers and scientists in the analysis and design, as conventional linear models may not suffice [12]. Therefore, a thorough understanding of nonlinear mechanics becomes crucial for fully harnessing the potential of these devices. Mathematical modeling and numerical simulations play an important role in this understanding, paving the way for the practical and effective application of these ultra-thin devices in cutting-edge technologies and scientific endeavors.

In the subsequent sections of this chapter, we will delve into the origins of nonlinearity in the mechanical behavior of ultra-thin membranes. Our exploration will center on structural nonlinearities, encompassing both geometric and material behaviors, as well as nonlinearities arising from excitation and read-out methods. Our attention will then shift to modeling and simulation techniques, where we will examine nonlinearities through two distinct lenses: continuum mechanics (CM) and molecular dynamics (MD) simulations. These two methodologies will serve as the primary modeling approaches in our investigation of nonlinear mechanical behavior in suspended ultra-thin membranes within this thesis, providing insights into their complex dynamics and properties.

1.2. ORIGINS OF MECHANICAL NONLINEARITIES IN 2D MATERIALS

In the mechanics of materials and structures, the origins of a nonlinear behavior might arise from either intrinsic factors within the structure or extrinsic factors in its surrounding environment. Both of these potential sources of nonlinearities can exhibit themselves in the device's stiffness as well as its dissipation characteristics [13].

1.2.1. INTERNAL SOURCES

GEOMETRIC NONLINEARITY

A slender solid can deform through two primary modes: bending and stretching. To stretch a solid, in-plane expansion is required, while bending involves creating curvature in out-of-plane direction. Although these deformation modes typically occur simultaneously, one often dominates the other in practical cases. The stretching stiffness k_s, representing resistance to stretching, is proportional to thickness ($k_s \propto h$), while the bending stiffness k_b, indicative of resistance to bending, is proportional to thickness cubed ($k_b \propto h^3$). As thickness decreases, these stiffness values diminish, with bending stiffness decreasing even more rapidly. Consequently, in the context of 2D materials and ultra-thin devices, which can be as thin as a few or a single layer of atoms, resistance to bending is literally negligible, which means even minor forces can induce bending deformations, readily leading to finite deformations [14].

In the context of a solid structure or continuum experiencing finite deformation, the strain tensor $\boldsymbol{\epsilon}$ can be expressed in the Cartesian coordinates as [15]

$$\boldsymbol{\epsilon} = \epsilon_{ij} = \frac{1}{2}\left[\frac{\partial u_i}{\partial X_j} + \frac{\partial u_j}{\partial X_i} + \frac{\partial u_i}{\partial X_j}\frac{\partial u_j}{\partial X_i}\right] \tag{1.1}$$

where u_i denotes the displacement field in the i-direction, and X_j is the reference coordinate in j-direction. The strain includes a combination of linear ($\frac{\partial u_i}{\partial X_j}$ and $\frac{\partial u_j}{\partial X_i}$) and nonlinear components ($\frac{\partial u_i}{\partial X_j}\frac{\partial u_j}{\partial X_i}$). In scenarios with infinitesimal deformation, since the magnitude of the deformation gradient is minimal, the nonlinear term can be considered insignificant. Nevertheless, due to the inherent property of ultra-thin membranes to undergo deformation even under minimal stresses, they readily transition into finite deformation regimes, also known as nonlinear geometric regimes. Consequently, geometric nonlinearities emerge as a crucial source of nonlinearity in the mechanical behavior of ultra-thin devices.

MATERIAL NONLINEARITY

In contrast to geometric nonlinearity, appearing in the strain -dislacement reslations, material nonlinearity is intrinsic to the constitutive law governing the relationship between stresses and strains, irrespective of the structure's geometry. This implies that, regardless of its geometry, a material subjected to a specific strain field will exhibit a stress field σ_{ij}, determined by the material's constitutive law, as represented by

$$\sigma_{ij} = \frac{\partial W}{\partial F_{ij}} \tag{1.2}$$

where W is the strain-energy density function, and F_{ij} denotes the deformation gradient tensor which is related to strain field ($\epsilon_{ij} = (1/2)\left(F_{ji}F_{ij} - I_{ij}\right)$, where I_{ij} denotes the identity matrix). It's important to note that while strains may be nonlinear due to finite deformation, the constitutive law might remain linear.

In the case of a linear elastic solid, the constitutive law simplifies to

$$\sigma_{ij} = C_{ijkl}\epsilon_{kl}, \tag{1.3}$$

where C_{ijkl} denotes a fourth-order tensor containing material constants. However, materials often deviate from this assumption in two general ways:

- **Nonlinear Elastic Material:** In this case, the stress-strain relationship is nonlinear. Using different strain-energy density function W can lead to various constitutive models, such as the neo-Hookean or the Mooney-Rivlin models [16] that can result in nonlinearities in the stiffness.

- **Anelastic Material:** These materials exhibit time-dependent elastic behavior, deviating from the instantaneous recovery observed in purely elastic materials. Unlike immediate return to their original shape upon load removal, anelastic materials display a time-dependent recovery, resulting in a delayed response to changes in stress or strain. The time-dependent behavior introduces damping in the mechanical response of the structure [17].

The constitutive law for anelastic materials is typically expressed using a relaxation function [18]

$$\sigma_{ij}(t) = \int_0^t G_{ijkl}(t-\tau, \epsilon_{kl}(\tau))\,\dot{\epsilon}_{kl}(\tau)\,\mathrm{d}\tau. \tag{1.4}$$

This function considers the time-dependent behavior and the strain history, with G_{ijkl} being the relaxation function explicitly dependent on both time and strain history. For linear anelastic materials, G_{ijkl} depends solely on time, while for nonlinear anelastic materials, it additionally relies on strain history. Consequently, the mechanical response of the structure can exhibit linear or nonlinear damping based on the linearity or nonlinearity of the anelastic behavior [19].

1.2.2. EXTERNAL SOURCES

ACTUATION NONLINEARITY

The use of loading or actuation techniques may cause nonlinearity in structural dynamics. Various forms of actuation forces, such as electrostatic forces [20, 21] and optothermal forces [22–25], exhibit nonlinear characteristics. For example, electrostatic force exerted on a membrane for actuation can be assumed as almost uniform force throughout the surface of the membrane. However, if the membrane undergoes large deflections, then this force will not remain uniform and may cause nonlinearities. Although actuation nonlinearities may cause distortions in the resultant signal during readout, it is important to note that these distortions may be successfully corrected and modified using a rather simple calibration technique, if the underlying physical phenomenon is well-understood. In general, by executing a series expansion of the force around the equilibrium position, the impact of nonlinear actuation terms can be systematically studied [26, 27].

READ-OUT NONLINEARITY

In addition to mechanical nonlinearities, higher harmonics can also be generated by the nonlinear readout voltage response function when pushing the membranes to large amplitudes. When the response function is fully known, the time-dependent position can be determined by measuring and correcting for the higher harmonics [28]. A comprehensive strategy comprising rigorous calibration, consideration of sensor properties, and signal processing is required to mitigate and resolve these nonlinear effects in the study of ultra-thin membrane dynamics [29].

INTERACTIONS WITH THE ENVIRONMENT

Ultra-thin membranes do not operate in isolation, but rather interact with their environment; or, at the very least, their behavior is influenced by their surrounding via boundary conditions [30]. While theoretical models frequently simplify these requirements, real-world circumstances introduce non-idealities. The often assumed clamped boundary condition in many manufactured 2D material resonators is challenged by weak van der Waals forces connecting the 2D material to the substrate [31]. These non-ideal boundary conditions contribute to nonlinearities in the mechanical behavior of the resonator, particularly under certain loadings such as those seen in atomic force microscopy experiments [32, 33].

Furthermore, when investigating the dynamics of ultra-thin membranes, it is typical to concentrate entirely on its isolated behavior, ignoring the potential impact of environmental couplings. These couplings can drastically modify the structure's dynamical behavior. When a device's substrate is vibrated to actuate a 2D material drum, for example, the dynamic interplay between the substrate and the drum becomes obvious [34]. Furthermore, it is critical to remember that, in addition to adhering to elasticity theory laws, mechanical deformations of a membrane should also obey thermodynamic laws [35]. This thermodynamic viewpoint introduces couplings between a structure and its surroundings, and such energy transfers can contribute to nonlinearities in the mechancial behavior, leading to nonlinearities in the stiffness and damping [36].

1.3. THEORETICAL MODELLING OF 2D MATERIALS

1.3.1. CONTINUUM MECHANICS

A continuous debate persists among scholars concerning the extent to which nano-scale structures conform to the fundamental principles of solid continuum mechanics (CM). Nevertheless, the effectiveness of techniques and models based on continuum theory has been confirmed by actual evidence, demonstrating their capacity to forecast the mechanical response of extremely thin membranes [12, 37].

The purpose of this section is to provide a review of the fundamental equations that govern the behavior of an elastic body. For illustrative purposes, we make the assumption that the continuum body possesses a generic shape. However, in the following chapters, we will utilize plate and membrane theories to apply these concepts to ultra-thin devices. These theories are specifically developed for slender structures, and offer simpler versions of CM theory. Thus, after presenting the necessary elements of continuum mechanics, the equations of motion of a circular plate will be obtained in details using classical CM theory in the subsequent section.

The equations governing the motion and deformation of a solid body fall into four basic categories:

1. Kinematics (strain-displacement equations)

2. Kinetics (conservation of momenta)

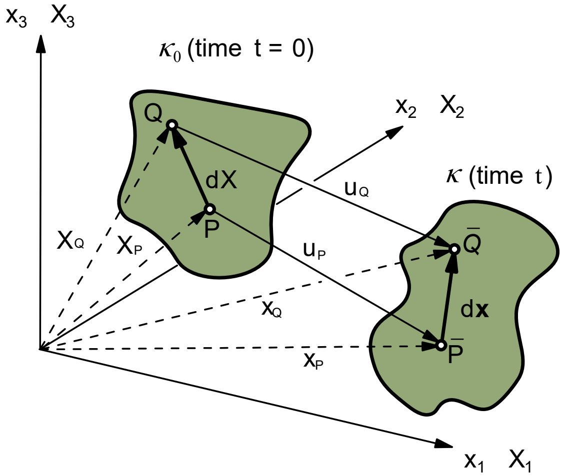

Figure 1.1: Undeformed and deformed configurations of a generic elastic body in continuum mechanics.

3. Thermodynamics (first and second laws of thermodynamics)

4. Constitutive equations (stress—strain relations).

The following sections provide an overview of the above for an elastic body, except for thermodynamic principles. For readers interested in thermal effects, I should note that thermal effects are often manifested as temperature-dependent material behaviour or strains caused by temperature gradients. The constitutive law framework addresses any temperature dependency of the constituent materials. Temperature gradients can cause thermodynamic strains in structures as well; however, in most scenarios, we assume slow energy transfers, which allows us to account for stresses caused by temperature gradients in thermodynamic equilibrium settings. However, if energy transfers are rapid, a coupled solution of elasticity and thermodynamic equations, known as thermoelasticity, is required [38].

KINEMATICS

The term *deformation* in mechanics refers to the relative displacements and changes in geometry experienced by a body. In a rectangular Cartesian frame of reference (X_1, X_2, X_3), each particle X in the body corresponds to a position $\mathbf{X} = (X_1, X_2, X_3)$. Upon deformation, particle X moves to a new position $\mathbf{x} = (x_1, x_2, x_3)$. The displacement of every particle in the body can be expressed as the difference between the deformed configuration κ and the reference configuration κ_0 (see figure 1.1). In the Lagrangian description, displacements $\mathbf{u}$ are expressed in terms of *material coordinates* $\mathbf{X}$

$$\mathbf{u}(\mathbf{X}, t) = \mathbf{x}(\mathbf{X}, t) - \mathbf{X}. \tag{1.5}$$

Deformation can be quantified in terms of the strain tensor $\boldsymbol{\epsilon}$, which is defined to give the change in the square of the length of the material vector $d\mathbf{X}$

$$\begin{aligned}
2d\mathbf{X}\cdot\boldsymbol{\epsilon}\cdot d\mathbf{X} &= d\mathbf{x}\cdot d\mathbf{x} - d\mathbf{X}\cdot d\mathbf{X} \\
&= d\mathbf{X}\cdot(\mathbf{I}+\nabla\mathbf{u})\cdot[d\mathbf{X}\cdot(\mathbf{I}+\nabla\mathbf{u})] - d\mathbf{X}\cdot d\mathbf{X} \\
&= d\mathbf{X}\cdot[(\mathbf{I}+\nabla\mathbf{u})\cdot((\mathbf{I}+\nabla\mathbf{u})^T - \mathbf{I})]\cdot d\mathbf{X},
\end{aligned} \tag{1.6}$$

where ∇ denotes the gradient operator with respect to the material coordinates $\mathbf{X}$, and $\boldsymbol{\epsilon}$ is known as the *Green–Lagrange strain tensor*, defined by equation (1.1). Note that the Green–Lagrange strain tensor is symmetric ($\epsilon_{ij} = \epsilon_{ji}$).

Kinetics

Let's consider a material body $\mathfrak{B}$ occupying a volume Ω with a boundary surface Γ. When subjected to external surface traction $\mathbf{T}$ (per unit surface area) and body forces $\mathbf{f}$ (per unit mass), the conservation of linear momentum asserts that the rate of change of the total linear momentum equals the vector summation of all external forces acting on $\mathfrak{B}$. This is mathematically expressed as

$$\frac{\partial\sigma_{ij}}{\partial X_j} + \rho f_i = \rho\frac{\partial^2 u_i}{\partial t^2}, \tag{1.7}$$

where ρ denotes the material density in its undeformed state, and t denotes time. It is noteworthy that among the two aforementioned forces acting on the body $\mathfrak{B}$, body forces $\mathbf{f}$ are present in equation (1.7), but the surface traction $\mathbf{T}$ is absent. Normal surface traction $\mathbf{T}$ acting on a plane with unit normal $\hat{\mathbf{n}}$ is related to the stress tensor σ by the Cauchy stress formula

$$\mathbf{T}_i = \sigma_{ij} n_j. \tag{1.8}$$

It can be shown that equation (1.7) is obtained using the second law of Newton based on balance of forces acting on the body $\mathfrak{B}$. From the analytical dynamics perspective, an equivalent equation can be obtained using the conservation of linear momentum. A common practice for obtaining the equivalent of equation (1.7) from energy perspective is to use Hamilton's principle. This principle results in [13]

$$\int_{t_1}^{t_2}\left(\int_\Omega \rho\dot{u}_i\delta\dot{u}_i \mathrm{d}\Omega - \int_\Omega \sigma_{ij}\delta\epsilon_{ij}\mathrm{d}\Omega - \int_\Omega \rho f_i \delta u_i \mathrm{d}\Omega\right)\mathrm{d}t = 0, \tag{1.9}$$

where δu denotes virtual displacement vector and $\delta\epsilon$ shows the virtual strains which are related to virtual displacements (see equation (1.1)).

Constitutive Equations

In continuum mechanics, the kinematic relations and fundamental mechanical and thermodynamic principles are applicable to all materials, regardless of their specific physical properties. Central to this understanding are the equations governing how materials respond to applied loads, known as *constitutive equations*. The establishment of these equations for a particular material follows established principles or *constitutive axioms* [39].

In the realm of materials science, a substance is deemed *ideally elastic* if, when subjected to deformation under constant temperature conditions, it fully restores its initial shape once the forces causing the deformation are removed. In this ideal scenario, there exists a direct correspondence between the stress applied to the material and the resulting strain it experiences.

Studies have demonstrated that certain 2D materials may exhibit anisotropic behavior [40]. While further investigation into the effects of anisotropy on the nonlinear mechanics of ultra-thin membranes is undoubtedly worthwhile, this dissertation assumes the constituent materials to be isotropic for simplicity and focus. This assumption further simplifies the linear constitutive law (1.3) to

$$\sigma_{ij} = 2\mu\epsilon_{ij} + \lambda\delta_{ij}\epsilon_{kk}, \tag{1.10}$$

where $\mu = \frac{E}{2(1+\nu)}$ and $\lambda = \frac{E\nu}{(1+\nu)(1-2\nu)}$. As can be seen a linear isotropic material has only two independent material constants (Young's modulus E and Poisson's ratio ν).

1.3.2. PLATE MODEL: CONTINUUM MECHANICS OF SLENDER STRUCTURES

In this section, we detail out the use of continuum mechanics formulations for deriving the equation of motion of a circular plate. These equations are the basis for the theoretical formulations of chapters 3, 4, and 5. The choice of this approach is based on the appropriateness of Kirchhoff plate theory for thin plate bending problems, particularly for 2D nanomaterials like graphene, where the thickness is significantly smaller than the in-plane dimensions. Von Kármán nonlinearities are incorporated to account for large deflections and nonlinear geometric effects, which are critical when modeling ultra-thin materials subjected to loading. This model has been widely adopted in the literature for similar problems and has proven effective in capturing the mechanical behavior of ultra-thin membranes [12, 14].

KINEMATICS

Let the r-coordinate be defined as radial distance from the center of the plate, the z-coordinate as thickness of the plate, and θ-coordinate as angular position along the circumference of the plate. In classical plate theory (CPT), a specific displacement field is often postulated

$$\begin{aligned} u_r(r,\theta,z,t) &= u(r,\theta,t) - z\frac{\partial w}{\partial r}, \\ u_\theta(r,\theta,z,t) &= v(r,\theta,t) - z\left(\frac{1}{r}\frac{\partial w}{\partial \theta}\right), \\ u_z(r,\theta,z,t) &= w(r,\theta,t), \end{aligned} \tag{1.11}$$

where u, v, and w denote the radial, angular, and transverse displacements, respectively, of a point on the midplane ($z = 0$) of the plate. This displacement field (equation (1.11)) is derived from the Kirchhoff hypothesis, which assumes that lines normal to the middle plane before deformation remain (1) inextensible, (2) straight, and (3) normal to the middle surface post-deformation [13].

The nonlinear strains can be derived using equation (1.1). If we consider only the non-zero von Kármán nonlinearity (i.e., excluding all nonlinear terms except those involving only u_z), the following expressions are obtained

$$\begin{aligned}
\epsilon_{rr} &= \frac{\partial u_r}{\partial r} + \frac{1}{2}\left(\frac{\partial u_z}{\partial r}\right)^2, \\
\epsilon_{\theta\theta} &= \frac{u_r}{r} + \frac{1}{r}\frac{\partial u_\theta}{\partial \theta} + \frac{1}{2}\left(\frac{1}{r}\frac{\partial u_z}{\partial \theta}\right)^2, \\
\epsilon_{r\theta} &= \frac{1}{2}\left(\frac{1}{r}\frac{\partial u_r}{\partial \theta} + \frac{\partial u_\theta}{\partial r} - \frac{u_\theta}{r} + \frac{1}{r}\frac{\partial u_z}{\partial r}\frac{\partial u_z}{\partial \theta}\right).
\end{aligned} \tag{1.12}$$

KINETICS

Using Hamilton's principle (1.9) for the circular plate yields

$$\begin{aligned}
0 = &\int_0^T \int_\Lambda \int_{-\frac{h}{2}}^{\frac{h}{2}} \left(\sigma_{rr}\delta\epsilon_{rr} + \sigma_{\theta\theta}\delta\epsilon_{\theta\theta} + \sigma_{r\theta}\delta\gamma_{r\theta}\right) dz\, r\, dr\, d\theta\, dt \\
&- \int_0^T \int_\Lambda \int_{-\frac{h}{2}}^{\frac{h}{2}} \rho\left(\dot u_r \delta \dot u_r + \dot u_\theta \delta \dot u_\theta + \dot u_z \delta \dot u_z\right) dz\, r\, dr\, d\theta\, dt \\
&- \int_0^T \int_\Lambda \int_{-\frac{h}{2}}^{\frac{h}{2}} q\, dz\, r\, dr\, d\theta\, dt
\end{aligned} \tag{1.13}$$

where h represents the plate thickness, $q = q(r,\theta,t)$ denotes the distributed transverse load, Λ signifies the mid-plane of the plate, and the overdot indicates the time derivative. Furthermore, δ denotes variation of the variables.

To derive the governing equations, we start by substituting the virtual strains $\delta\epsilon_{rr}$, $\delta\epsilon_{\theta\theta}$, and $\gamma_{r\theta}$ from equation(1.12) into equation (1.13). Then, integrating over the plate thickness and applying integration by parts to eliminate differentiations with respect to $(\delta u, \delta v, \delta w)$, we set the coefficients of these virtual displacements to zero individually using the fundamental lemma of the calculus of variations. This process yields the following equations

$$\delta u: -\frac{1}{r}\left[\frac{\partial}{\partial r}(rN_{rr}) + \frac{\partial N_{r\theta}}{\partial \theta} - N_{\theta\theta}\right] + I_0\frac{\partial^2 u}{\partial t^2} = 0, \tag{1.14a}$$

$$\delta v: -\frac{1}{r}\left[\frac{\partial}{\partial r}(rN_{r\theta}) + \frac{\partial N_{\theta\theta}}{\partial \theta} + N_{r\theta}\right] + I_0\frac{\partial^2 v}{\partial t^2} = 0, \tag{1.14b}$$

$$\begin{aligned}
\delta w: &-\frac{1}{r}\left[\frac{\partial^2}{\partial r^2}(rM_{rr}) - \frac{\partial M_{\theta\theta}}{\partial r} + \frac{1}{r}\frac{\partial^2 M_{\theta\theta}}{\partial \theta^2} + \frac{2}{r}\frac{\partial}{\partial r}\left(r\frac{\partial M_{r\theta}}{\partial \theta}\right)\right] \\
&+ \frac{\partial}{\partial r}\left(rN_{rr}\frac{\partial w}{\partial r} + N_{r\theta}\frac{\partial w}{\partial \theta}\right) + \frac{1}{r}\frac{\partial}{\partial \theta}\left(N_{\theta\theta}\frac{\partial w}{\partial \theta} + rN_{r\theta}\frac{\partial w}{\partial r}\right) \\
&+ I_0\frac{\partial^2 w}{\partial t^2} - I_2\frac{\partial^2}{\partial t^2}\left[\frac{1}{r}\frac{\partial}{\partial r}\left(r\frac{\partial w}{\partial r}\right) + \frac{1}{r^2}\frac{\partial^2 w}{\partial \theta^2}\right] = q.
\end{aligned} \tag{1.14c}$$

Here, $I_0 = \rho h$ and $I_2 = \rho h^3/12$. The forces $(N_{rr}, N_{\theta\theta}, N_{r,\theta})$ and moments $(M_{rr}, M_{\theta\theta},$

$M_{r,\theta}$) are defined as

$$\begin{aligned} N_{rr} &= \int_{-\frac{h}{2}}^{\frac{h}{2}} \sigma_{rr}\, dz, \quad & N_{\theta\theta} &= \int_{-\frac{h}{2}}^{\frac{h}{2}} \sigma_{\theta\theta}\, dz, \quad & N_{r\theta} &= \int_{-\frac{h}{2}}^{\frac{h}{2}} \sigma_{r\theta}\, dz, \\ M_{rr} &= \int_{-\frac{h}{2}}^{\frac{h}{2}} \sigma_{rr} z\, dz, \quad & M_{\theta\theta} &= \int_{-\frac{h}{2}}^{\frac{h}{2}} \sigma_{\theta\theta} z\, dz, \quad & M_{r\theta} &= \int_{-\frac{h}{2}}^{\frac{h}{2}} \sigma_{r\theta} z\, dz. \end{aligned} \tag{1.15}$$

CONSTITUTIVE EQUATIONS

In order to solve equations (1.14), one should also take into account the relationship between stress and strain fields through a constitutive equation. The constituent material can have complex nonlinear time-dependent behaviour; however, in this dissertation, we assumed materials to be linear isotropic (equation (1.10)). Thus, for a plate made of isotropic material with Young's modulus E, density ρ, and Poisson ratio ν, equation (1.14) can be reformulated into the following compact form

$$\rho h \ddot{w} + D\nabla^4 w - \nabla \cdot (\boldsymbol{N} \nabla w) = 0, \tag{1.16a}$$

$$\rho h \ddot{\boldsymbol{u}} - \nabla \cdot \boldsymbol{N} = 0, \tag{1.16b}$$

where

$$\boldsymbol{N} = [Eh/(1-\nu^2)]\,[(1-\nu)\boldsymbol{\epsilon} + \nu \mathrm{tr}(\boldsymbol{\epsilon})\boldsymbol{I}] \tag{1.17}$$

In this compact form, the rotary inertia I_2 is neglected, which is a common assumption for thin structures. In the equations above, $\boldsymbol{u} = [u; v]$, while w represents the transverse displacement field. Additionally, $\nabla^4 w$, ∇w, and $\nabla \boldsymbol{u}$ denote the biharmonic operator applied to the scalar field w, the vector gradient of the scalar field w, and the tensor gradient of the vector field $\boldsymbol{u}$, respectively. $\nabla \cdot \boldsymbol{N}$ represents the divergence of the tensor field $\boldsymbol{N}$. An overdot indicates differentiation with respect to time, and $D = \frac{Eh^3}{12(1-\nu^2)}$ denotes the bending rigidity. It is usually assumed that when the plate aspect ratio (thickness to radius ratio) is small (i.e., $h/R < 0.001$ [41]), a membrane model is utilized instead of a plate model. In this circumstance, bending energies are removed, resulting in the discarding of the term $D\nabla^4 w$ from the governing equations.

1.3.3. MOLECULAR DYNAMICS SIMULATIONS

This dissertation explores the field of atomically-thin structures, where a comprehensive understanding of molecular interactions is necessary to comprehend the mechanical behavior of ultra-thin membranes. Various tools, including quantum mechanics [42] and Density Functional Theory (DFT) [43], provide valuable insights into atomic and molecular-scale problems. However, the significant computational time required for these methods limits their extensive use in applied research studies. Among atomic-scale techniques, MD simulations emerge as a popular choice due to their reasonable computational efficiency.

A brief explanation of the fundamental concepts underlying MD simulations is presented in the following sections. When appropriate, specific simulation options selected for this dissertation are provided and detailed, including the force field and thermostat choices.

BASIC PRINCIPLES

MD operates as a deterministic evolution of a molecular system over time, rooted in Newton's second law

$$m_i \frac{d^2\mathbf{r}_i}{dt^2} = \mathbf{F}_i, \tag{1.18}$$

where, m_i denotes the mass of particle i, $\mathbf{r}_i$ represents its position, and $\mathbf{F}_i$ stands for the force acting upon it. This brief expression describes the motion of individual particles. Combining these equations for all particles reveals the evolution of the entire molecular system over time.

FORCE FIELDS

Although assuming atoms as point masses may seem an appropriate assumption for modelling a molecular-level system, how these point masses interact with each other significantly affects the temporal trajectory of the system. In MD, a force field (potential function) is utilized for capturing the atomic interactions. These force fields play an important role in defining the potential energy fields that govern the movement of atoms. The force $\mathbf{F}_{ij}$ between particles i and j can be obtained as

$$\mathbf{F}_{ij} = -\nabla U_{ij}(\mathbf{r}_{ij}) \tag{1.19}$$

Here, U_{ij} is the potential energy field between particles and $\mathbf{r}_{ij} = \mathbf{r}_i - \mathbf{r}_j$ denotes the vectorial displacement between particles.

MD interactions are broadly categorized into two fundamental types

- **Bonded Interactions:** They encompass covalent bonds, angles, and dihedral angles.
- **Non-Bonded Interactions:** They include interactions, such as van der Waals forces and electrostatic interactions.

The combined effect of these bonded and non-bonded interactions defines the potential energy U_{ij}, resulting in a system of coupled differential equations that govern the dynamic evolution of molecular systems, as expressed through Eqs. (1.18) and (1.19).

A "standard" modern force field can be formulated as

$$U = \left[\sum_{\text{stretch}} U_{AB} + \sum_{\text{bond}} U_{ABC} + \sum_{\text{dihedral}} U_{ABCD}\right] + \left[\sum_{\text{nonbonded}} U_{LJ} + \sum_{\text{Coulomb}} U_{QQ}\right], \tag{1.20}$$

Where U_{LJ} and U_{QQ} represent potentials for taking into account the van der Waals and electrostatic interactions, respectively. Each of the terms in equation (1.20) are explained and detailed in the following sections.

Bond Stretching: The potential for stretch of bonds U_{AB} can be modeled using Hooke's law in the simplest form as

$$U_{AB} = \frac{1}{2} k_{AB} \left(r_{AB} - r_{e,AB}\right)^2, \tag{1.21}$$

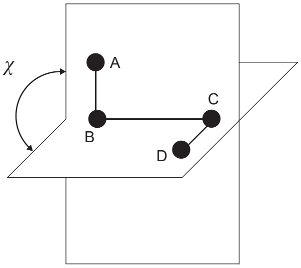

Figure 1.2: Schematic of a dihedral angle in a configuration of particles.

where k_{AB} denotes the bond stiffness, and subscript e denotes equilibrium.

Bond Bending: Linear Hookean law can also be used for bond bending energies, expressed as

$$U_{ABC} = \frac{1}{2} k_{ABC} \left(\theta_{ABC} - \theta_{e,ABC}\right)^2, \tag{1.22}$$

where θ denotes the bond angle, and k_{ABC} shows the bond bending stiffness.

Dihedral Motions: Dihedral angles χ (see figure 1.2) between four bonded atoms are captured using a periodic dihedral potential

$$U_{ABCD} = \frac{1}{2} \left(1 - \cos\left(n\left(\chi - \chi_e\right)\right)\right), \tag{1.23}$$

where, n is the periodicity parameter.

Van der Waals Forces: Van der Waals interactions are often modeled using Lennard-Jones potential

$$U_{LJ} = \frac{C_{12}}{r^{12}} - \frac{C_6}{r^6}, \tag{1.24}$$

where C_{12} and C_6 are constants to be defined for each pair of particles.

Coulomb Interactions: Electronegativity differences between atoms give rise to Coulomb interactions, expressed as

$$U_{QQ} = \frac{1}{4\pi\varepsilon_0} \frac{Q_A Q_B}{r_{AB}}, \tag{1.25}$$

where ε_0 is the permittivity of vacuum, and Q denotes point charge.

The force field components discussed in the present discussion are the fundamental components, while the models used are of the most basic type. Many sophisticated force fields are tailored for simulating atomic interactions in diverse physical contexts. Since all MD simulations in this study focus on graphene, a force field optimized for carbon-carbon interactions is essential. Common potentials for this purpose include REBO [44], AIREBO [45], and LCBOP [46]. Notably, all simulations in this work employ the Tersoff potential [47], which proved to be a computationally efficient and precise force field. A brief overview of this force field and its components is presented next.

Tersoff Force Field:
First, it should be noted that the variables in the second bracket of equation (1.20) that account for non-bonded Wan der Waals and electrostatic interactions are absent from this potential, which solely accounts for bonded interactions. In addition to the Tersoff force field, a non-bonded potential such as Lennard-Jones should be used in simulations where non-bonded interactions are significant, such as when simulating a bi-layer graphene.

The Tersoff potential is formulated as

$$\begin{aligned} U &= \tfrac{1}{2}\sum_{i}\sum_{j\neq i} V_{ij} \\ V_{ij} &= f_C\left(r_{ij}+\delta\right)\left[f_R\left(r_{ij}+\delta\right)+b_{ij}f_A\left(r_{ij}+\delta\right)\right] \end{aligned} \tag{1.26}$$

where

$$f_C(r) = \begin{cases} 1 & r < R-D \\ \frac{1}{2}-\frac{1}{2}\sin\left(\frac{\pi}{2}\frac{r-R}{D}\right) & R-D < r < R+D \\ 0 & r > R+D \end{cases} \tag{1.27}$$

is a cut-off function, and

$$\begin{aligned} f_R(r_{ij}+\delta) &= A\exp(-\lambda_1 r), \\ f_A(r_{ij}+\delta) &= -B\exp(-\lambda_2 r), \\ b_{ij} &= \left(1+\beta^n \varsigma_{ij}^n\right)^{-\frac{1}{2n}}, \\ \varsigma_{ij} &= \sum_{k\neq i,j} f_C(r_{ik}+\delta)\cdot g\left(\theta_{ijk}(r_{ij},r_{ik})\right)\exp\left(\lambda_3^m (r_{ij}-r_{ik})^m\right), \\ g(\theta) &= \gamma_{ijk}\left(1+\frac{c^2}{d^2}-\frac{c^2}{d^2+(\cos(\theta)-\cos(\theta_0))^2}\right). \end{aligned} \tag{1.28}$$

Here, f_R represents a repulsive bond stretch energy, and f_A denotes an attractive bond stretch energy term. Moreover, b_{ij} encompasses a "three-body" bond bending where three atoms form a bond angle of θ together. The cutoff function f_C is incorporated to reduce computational costs by excluding interactions among atoms that are sufficiently distant from each other. The parameters R, D, and δ represent the base cutoff radius, scaling factor, and characteristic length scale, respectively, which can be set by the user of any MD software package. Parameters A, B, λ_1, λ_2, β, n, λ_3, m, γ, c, d, and θ_0 are specific to the material being simulated and are typically provided by the user based on empirical data or theoretical considerations. Notably, Tersoff force field does not contain any potential term for taking into account the dihedral angle distortions which is not a significant issue for simulating graphene membranes.

INTEGRATION ALGORITHMS

In order to solve the equations of motion in an MD setting, a numerical integration technique is necessary. In this dissertation, we utilized the Velocity Verlet algorithm. This algorithm integrates both the positions $\mathbf{r}_i$ and velocities $\mathbf{v}_i$ of particles in discrete time steps Δt.

The Velocity Verlet technique combines position and velocity updates to capture the dynamic evolution of particles throughout time. The position of particle i at time $t+\Delta t$ is determined by a complicated interplay of its present position $\mathbf{r}_i(t)$, the previous position $\mathbf{r}_i(t-\Delta t)$, the force acting on it $\mathbf{F}_i$, and the particle's mass m_i

$$\mathbf{r}_i(t+\Delta t) = 2\mathbf{r}_i(t) - \mathbf{r}_i(t-\Delta t) + \frac{\mathbf{F}_i}{m_i}(\Delta t)^2. \tag{1.29}$$

Simultaneously, the velocity of particle i at time t is computed by evaluating the difference in position at $t+\Delta t$ and $t-\Delta t$ and scaling it appropriately with $2\Delta t$

$$\mathbf{v}_i(t) = \frac{\mathbf{r}_i(t+\Delta t) - \mathbf{r}_i(t-\Delta t)}{2\Delta t}. \tag{1.30}$$

THERMODYNAMIC ENSEMBLES

In the context of MD simulations, classical Newtonian mechanics provides the fundamental principles for understanding particle motion within a system. However, to align these dynamic processes with the principles of statistical thermodynamics, MD simulations operate within the framework of thermodynamic ensembles. Each ensemble within this framework is characterized by distinct thermodynamic constraints, coordinating the simulation under specific conditions. The micro-canonical ensemble (NVE) stands as the most fundamental, conserving particle number N, volume V, and energy E. Under NVE, where energy is conserved, the application of classical Newtonian mechanics remains straightforward. In contrast, the canonical ensemble (NVT) and isothermal-isobaric ensemble (NPT) introduce additional controls to reflect real-world scenarios. The NVT ensemble maintains particle number while introducing temperature T control, and the NPT ensemble, while conserving particle number, regulates both temperature T and pressure P.

Controlling temperature and pressure within a system necessitates the introduction of new concepts, namely thermostats and barostats. Unlike the NVE ensemble, where energy conservation simplifies the application of classical mechanics, the NVT and NPT ensembles require the implementation of these specialized tools to ensure accurate temperature and pressure regulation throughout the simulation. In this way, thermodynamic ensembles serve as a bridge, allowing MD simulations to adhere to both the principles of classical mechanics and the rules of statistical thermodynamics.

Thermostats: Temperature control is achieved through algorithms that couple the system to a thermostat, ensuring that the temperature remains constant. A widely used thermostat is the Nose-Hoover thermostat [48]. It introduces an additional generalized coordinate s, to the system which characterizes the stretching in the time scale between the time scale of the bath and the membrane's time scale. The mathematical formulation of the Nose-Hoover thermostat includes the following equations

- **Equation of Motion for the Thermostat Variable:**

$$\dot{s} = \frac{1}{M}\left(\sum_i \frac{p_i^2}{m_i} - Nk_B T\right).$$

where $\dot{s}$ represents the time derivative of s, M is a user-defined parameter determining the strength of the coupling, N is the number of particles, k_B is the Boltzmann constant, and T is the target temperature.

- **Modified Equations of Motion for Particles:**

$$\dot{p}_i = -\frac{\partial U}{\partial q_i} - s\frac{p_i}{M},$$
$$\dot{q}_i = \frac{p_i}{m_i}.$$

Here, p_i and q_i are the momentum and position of particle i, m_i is its mass, U is the potential energy, and the dot denotes the time derivative.

Additionally, barostats in MD simulations are employed to control and maintain the pressure of a simulated system. There are many different barostats available to be employed. For example, one commonly used barostat is the Berendsen barostat [49], which involves a mathematical formulation to dynamically adjust the system's volume at each time step. Since we did not use NPT ensemble in this dissertation, we do not delve into the details of barostating the system.

1.4. OUTLINE OF THE THESIS

In previous sections, I highlighted the importance of ultra-thin membranes, particularly in sensing applications, due to their unique properties. Given the complex mechanical behaviors and inherent nonlinearities of these devices, it is critical to emphasize the need for comprehensive modeling and predictive techniques.

A common method in the study of 2D materials is to consider them as flat and uniformly pre-stressed. Chapters 2 and 3 thoroughly analyze these typical underlying assumptions. We investigate whether a more comprehensive model can outperform existing ones by employing a nonlinear modeling method that avoids such simplifications.

The fourth chapter studies how pressure gradients between membrane surfaces influence vibration behavior. We demonstrate how disregarding nonlinear static deformation can result in significant errors in predicting resonance frequencies. Simultaneously, we show the importance of mid-plane stretching and higher mode interactions to obtain pressure-frequency responses with high accuracy. This chapter demonstrates a nonlinear mechanics problem involving simultaneous static and dynamic loading.

The final chapter summarises the findings, providing a comprehensive overview of the work as well as the outlook for future research. We investigate further nonlinear mechanics problems that have yet to be effectively modelled, utilizing the capabilities of CM and MD. This discussion goes beyond mechanical analysis to include mechanical design issues for these devices, as well as prospective tools for proposing new designs in the world of nonlinear mechanics. The chapter also considers the intrinsic strengths and limitations of CM and MD in addressing nonlinear mechanics problems.

BIBLIOGRAPHY

[1] Geim, A.K., 2009. Graphene: status and prospects. science, 324(5934), pp.1530-1534.

[2] Butler, S.Z., Hollen, S.M., Cao, L., Cui, Y., Gupta, J.A., Gutiérrez, H.R., Heinz, T.F., Hong, S.S., Huang, J., Ismach, A.F. and Johnston-Halperin, E., 2013. Progress, challenges, and opportunities in two-dimensional materials beyond graphene. ACS nano, 7(4), pp.2898-2926.

[3] Bhimanapati, G.R., Lin, Z., Meunier, V., Jung, Y., Cha, J., Das, S., Xiao, D., Son, Y., Strano, M.S., Cooper, V.R. and Liang, L., 2015. Recent advances in two-dimensional materials beyond graphene. ACS nano, 9(12), pp.11509-11539.

[4] Akinwande, D., Brennan, C.J., Bunch, J.S., Egberts, P., Felts, J.R., Gao, H., Huang, R., Kim, J.S., Li, T., Li, Y. and Liechti, K.M., 2017. A review on mechanics and mechanical properties of 2D materials—Graphene and beyond. Extreme Mechanics Letters, 13, pp.42-77.

[5] Das, S., Kim, M., Lee, J.W. and Choi, W., 2014. Synthesis, properties, and applications of 2-D materials: A comprehensive review. Critical Reviews in Solid State and Materials Sciences, 39(4), pp.231-252.

[6] Fiori, G., Bonaccorso, F., Iannaccone, G., Palacios, T., Neumaier, D., Seabaugh, A., Banerjee, S.K. and Colombo, L., 2014. Electronics based on two-dimensional materials. Nature nanotechnology, 9(10), pp.768-779.

[7] Tian, H., Shu, Y., Wang, X.F., Mohammad, M.A., Bie, Z., Xie, Q.Y., Li, C., Mi, W.T., Yang, Y. and Ren, T.L., 2015. A graphene-based resistive pressure sensor with record-high sensitivity in a wide pressure range. Scientific reports, 5(1), p.8603.

[8] Peña-Bahamonde, J., Nguyen, H.N., Fanourakis, S.K. and Rodrigues, D.F., 2018. Recent advances in graphene-based biosensor technology with applications in life sciences. Journal of nanobiotechnology, 16, pp.1-17.

[9] Liu, W., Lv, J., Peng, L., Guo, H., Liu, C., Liu, Y., Li, W., Li, L., Liu, L., Wang, P. and Bodepudi, S.C., 2022. Graphene charge-injection photodetectors. Nature Electronics, 5(5), pp.281-288.

[10] Sun, H., Mukherjee, S., Daly, M., Krishnan, A., Karigerasi, M.H. and Singh, C.V., 2016. New insights into the structure-nonlinear mechanical property relations for graphene allotropes. Carbon, 110, pp.443-457.

[11] Lu, Q. and Huang, R., 2009. Nonlinear mechanics of single-atomic-layer graphene sheets. International Journal of Applied Mechanics, 1(03), pp.443-467.

[12] Davidovikj, D., Alijani, F., Cartamil-Bueno, S.J., van der Zant, H.S., Amabili, M. and Steeneken, P.G., 2017. Nonlinear dynamic characterization of two-dimensional materials. Nature Communications, 8(1), p.1253.

[13] Reddy, J.N., 2006. Theory and analysis of elastic plates and shells. CRC press.

[14] Sajadi, B., Wahls, S., van Hemert, S., Belardinelli, P., Steeneken, P.G. and Alijani, F., 2019. Nonlinear dynamic identification of graphene's elastic modulus via reduced order modeling of atomistic simulations. Journal of the Mechanics and Physics of Solids, 122, pp.161-176.

[15] Amabili, M., 2008. Nonlinear vibrations and stability of shells and plates. Cambridge University Press.

[16] Ogden, R.W., 1997. Non-linear elastic deformations. Courier Corporation.

[17] Li, D. and Wagoner, R.H., 2021. The nature of yielding and anelasticity in metals. Acta Materialia, 206, p.116625.

[18] Flügge, W., 1975. Viscoelasticity, 2nd edition (pp. 95–120). New York: Springer.

[19] Gutierrez-Lemini, D., 2014. Engineering viscoelasticity (pp. 23-52). New York: Springer.

[20] Sajadi, B., Alijani, F., Davidovikj, D., Goosen, J.H., Steeneken, P.G. and van Keulen, F., 2017. Experimental characterization of graphene by electrostatic resonance frequency tuning. Journal of Applied Physics, 122(23).

[21] De Alba, R., Massel, F., Storch, I.R., Abhilash, T.S., Hui, A., McEuen, P.L., Craighead, H.G. and Parpia, J.M., 2016. Tunable phonon-cavity coupling in graphene membranes. Nature nanotechnology, 11(9), pp.741-746.

[22] Inoue, T., Anno, Y., Imakita, Y., Takei, K., Arie, T. and Akita, S., 2017. Resonance control of a graphene drum resonator in a nonlinear regime by a standing wave of light. ACS omega, 2(9), pp.5792-5797.

[23] Dolleman, R.J., Houri, S., Chandrashekar, A., Alijani, F., Van Der Zant, H.S. and Steeneken, P.G., 2018. Opto-thermally excited multimode parametric resonance in graphene membranes. Scientific Reports, 8(1), p.9366.

[24] Dolleman, R.J., Belardinelli, P., Houri, S., van der Zant, H.S., Alijani, F. and Steeneken, P.G., 2019. High-frequency stochastic switching of graphene resonators near room temperature. Nano letters, 19(2), pp.1282-1288.

[25] Houri, S., Cartamil-Bueno, S.J., Poot, M., Steeneken, P.G., Van der Zant, H.S.J. and Venstra, W.J., 2017. Direct and parametric synchronization of a graphene self-oscillator. Applied Physics Letters, 110(7).

[26] Samanta, C., Arora, N. and Naik, A.K., 2018. Tuning of geometric nonlinearity in ultrathin nanoelectromechanical systems. Applied Physics Letters, 113(11).

[27] Dash, A., Samanta, C., Ranganath, P., Selvaraja, S.K. and Naik, A.K., 2019. Optical gradient force for tuning, actuation, and manipulation of nonlinearity in graphene nanomechanical resonator. Journal of Optics, 21(6), p.065803.

[28] Verbiest, G.J., Kirchhof, J.N., Sonntag, J., Goldsche, M., Khodkov, T. and Stampfer, C., 2018. Detecting ultrasound vibrations with graphene resonators. Nano letters, 18(8), pp.5132-5137.

[29] Dolleman, R.J., Davidovikj, D., Van Der Zant, H.S. and Steeneken, P.G., 2017. Amplitude calibration of 2D mechanical resonators by nonlinear optical transduction. Applied Physics Letters, 111(25).

[30] Mao, X.Y., Ding, H. and Chen, L.Q., 2017. Vibration of flexible structures under nonlinear boundary conditions. Journal of Applied Mechanics, 84(11), p.111006.

[31] Boddeti, N.G., Koenig, S.P., Long, R., Xiao, J., Bunch, J.S. and Dunn, M.L., 2013. Mechanics of adhered, pressurized graphene blisters. Journal of Applied Mechanics, 80(4), p.040909.

[32] Davidovitch, B. and Guinea, F., 2021. Indentation of solid membranes on rigid substrates with van der Waals attraction. Physical Review E, 103(4), p.043002.

[33] Lee, J., Hu, X., Voevodin, A.A., Martini, A. and Berman, D., 2018. Effect of substrate support on dynamic graphene/metal electrical contacts. Micromachines, 9(4), p.169.

[34] Smith, A.D., Niklaus, F., Paussa, A., Vaziri, S., Fischer, A.C., Sterner, M., Forsberg, F., Delin, A., Esseni, D., Palestri, P. and Ostling, M., 2013. Electromechanical piezoresistive sensing in suspended graphene membranes. Nano letters, 13(7), pp.3237-3242.

[35] Eichler, A., Moser, J., Chaste, J., Zdrojek, M., Wilson-Rae, I. and Bachtold, A., 2011. Nonlinear damping in mechanical resonators made from carbon nanotubes and graphene. Nature nanotechnology, 6(6), pp.339-342.

[36] Zaitsev, S., Shtempluck, O., Buks, E. and Gottlieb, O., 2012. Nonlinear damping in a micromechanical oscillator. Nonlinear Dynamics, 67, pp.859-883.

[37] Steeneken, P.G., Dolleman, R.J., Davidovikj, D., Alijani, F. and Van der Zant, H.S., 2021. Dynamics of 2D material membranes. 2D Materials, 8(4), p.042001.

[38] Eslami, M.R., Hetnarski, R.B., Ignaczak, J., Noda, N., Sumi, N. and Tanigawa, Y., 2013. Theory of elasticity and thermal stresses (Vol. 197, p. 786). Dordrecht: Springer.

[39] Darijani, H. and Naghdabadi, R., 2010. Hyperelastic materials behavior modeling using consistent strain energy density functions. Acta mechanica, 213(3-4), pp.235-254.

[40] Siskins, M., Lee, M., Alijani, F., Van Blankenstein, M.R., Davidovikj, D., Van Der Zant, H.S. and Steeneken, P.G., 2019. Highly anisotropic mechanical and optical properties of 2D layered As2S3 membranes. ACS nano, 13(9), pp.10845-10851.

[41] Mansfield, E. (1989). The Bending and Stretching of Plates. Cambridge University Press.

[42] Kutzelnigg, W., 2006. Density Functional Theory (DFT) and ab-initio Quantum. Trends and Perspectives in Modern Computational Science, 6, p.23.

[43] Argaman, N. and Makov, G., 2000. Density functional theory: An introduction. American Journal of Physics, 68(1), pp.69-79.

[44] Brenner, D.W., 1990. Empirical potential for hydrocarbons for use in simulating the chemical vapor deposition of diamond films. Physical review B, 42(15), p.9458.

[45] Stuart, S.J., Tutein, A.B. and Harrison, J.A., 2000. A reactive potential for hydrocarbons with intermolecular interactions. The Journal of chemical physics, 112(14), pp.6472-6486.

[46] Los, J.H. and Fasolino, A., 2003. Intrinsic long-range bond-order potential for carbon: Performance in Monte Carlo simulations of graphitization. Physical Review B, 68(2), p.024107.

[47] Tersoff, J., 1988. New empirical approach for the structure and energy of covalent systems. Physical review B, 37(12), p.6991.

[48] Nosé, S., 1984. A unified formulation of the constant temperature molecular dynamics methods. The Journal of chemical physics, 81(1), pp.511-519.

[49] Berendsen, H.J., Postma, J.V., Van Gunsteren, W.F., DiNola, A.R.H.J. and Haak, J.R., 1984. Molecular dynamics with coupling to an external bath. The Journal of chemical physics, 81(8), pp.3684-3690.

2

2

NONLINEAR MECHANICS OF IMPERFECT MEMBRANES

Owing to their atomic thickness and low bending rigidity, suspended two-dimensional (2D) materials are prone to wrinkle formation. Here, we use molecular dynamics (MD) simulations to probe the effect of these wrinkles on the nonlinear elasticity of atomically thin graphene membranes. We observe a stress-strain response that consists of two linear regions that are separated by a transition. It is found that this transition is sharp in membranes where wrinkles are formed by uneven stresses at the boundaries. However, when wrinkles are formed by crystal defects, this nonlinear transition is seen to be more gradual. To capture these effects, we use a phenomenological model based on experimentally measurable quantities. We demonstrate the model's fidelity by fitting it to the MD simulated nonlinear response of many graphene membranes providing evidence that the sharpness of the transition between the linear regions in the stress-strain response is a measure of the type of wrinkles and can be quantified by our model.

This chapter was published as:
Sarafraz, A., Arjmandi-Tash, H., Dijkink, L., Sajadi, B., Moeini, M., Steeneken, P.G. and Alijani, F., 2021. Nonlinear elasticity of wrinkled atomically thin membranes. *Journal of Applied Physics*, 130(18).

2.1. INTRODUCTION

Wrinkles are out-of-plane deviations from flat configuration that are frequently observed in the fabrication of 2D material membranes. These corrugations manifest themselves in both suspended [1] and substrate-supported [2, 3] 2D materials and can significantly influence their electronic and mechanical properties [4–6]. Therefore, thorough understanding of the influence of wrinkles in 2D material membranes is key to the development of high-performance 2D nanomechanical devices.

Multiple wrinkled regions with different patterns may coexist in a single 2D membrane [7–13]. These regions often comprise static wrinkles that can be the consequence of uneven stress at the boundaries of the membrane [10, 14, 15], surface functionalization with molecules [16–18], or crystal defects [19, 20]. Among them, the latter is particularly shown to reduce the stiffness of 2D membranes and lead to auxetic properties such as negative Poisson's ratio [21]. Entropic fluctuations due to Brownian motion are another source of wrinkles intrinsic to these materials that can give rise to exotic properties such as negative thermal expansion coefficient [22] and size-dependent elastic constants [23, 24].

The stretching of a wrinkled 2D material is a two-level process and exhibits a bilinear stress-strain response that consists of two linear parts, each with a different effective stiffness. At relatively low tensile strains, the applied force "irons out" the wrinkles and results in low effective stiffness [25]. Once the wrinkles are suppressed, high stiffness is observed due to the stretching of the atomic bonds [26]. Recent experimental observations also suggest a nonlinear transition state between these two stiffness levels that so far is not well-understood [10, 25, 26].

This work aims at clarifying the nature of this nonlinear behavior via molecular dynamics (MD) simulations. We perform our simulations on graphene as a model system to develop a general procedure for probing the elasticity of wrinkled 2D materials. We create wrinkles both by compressive forces at the boundaries and by introducing crystal defects. While pre-stress is the root cause of wrinkle formation in the presence of compressive forces at the boundaries, 2D crystal defects in a stress-free membrane, generate a wrinkled state that is solely the result of the 2D lattice imperfections.

The proposed approach for probing the nonlinear elasticity of wrinkled graphene is as follows: In Section 2, we use a theoretical model to qualitatively describe the nonlinear elasticity of wrinkled membranes. In Section 3, we employ MD simulations for modelling and comparing the response of membranes that are either wrinkled by compressive forces at the boundaries or by crystal defects. Finally, in Section 4, we discuss the effects of these wrinkles on the stress-strain response of graphene and propose a phenomenological model that captures the nonlinear elasticity of wrinkled membranes and identifies the differences between the effect of lattice defects and compressive stress via the stress-strain response.

2.2. ANALYTICAL MODELING

From linear elasticity it is known that isotropic materials follow Hooke's law. According to this law, material stiffness is characterized by the biaxial modulus $E_{2D}^{f} = Eh/(1-\nu)$ (E is the Young's modulus, ν Poisson's ratio and h is the thickness) in a standard equi-biaxial

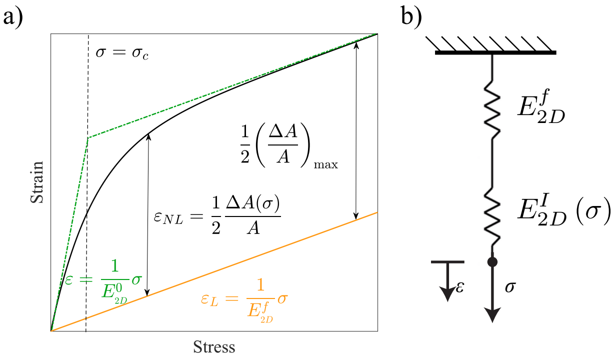

Figure 2.1: Phenomenological model of the effective stress-strain response of biaxially tensioned wrinkled graphene membranes. a) Schematic representation of the bilinear approximation and its independent and dependent parameters. The solid black line is the response of a wrinkled membrane following equation (2.1)-(2.3), the solid orange line represents a pristine unwrinkled membrane and the dash-dot green lines are the tangents to the curve close to the origin and at maximum stress (bilinear approximation, equation (2.4)); b) Spring-in-series system with a linear spring with constant stiffness representing the intrinsic stiffness of flat pristine graphene E^f_{2D} and nonlinear spring with a stress dependent stiffness $E^I_{2D}(\sigma)$ representing the stiffness of the wrinkles.

test. However, for wrinkled membranes, experimental results show that the stress-strain response deviates from Hooke's law, and the observed slopes do not depend on the *material stiffness* but instead are *geometrical effects* that can be influenced by the boundary forces and morphological imperfections [27].

In order to model such effects in a simple way, we assume Hooke's law for the material, use plane-stress condition and determine the engineering strain ε in the following way [10]:

$$\varepsilon(\sigma) = \frac{1}{E^f_{2D}}\sigma + \frac{1}{2}\frac{\Delta A(\sigma)}{A}, \tag{2.1}$$

where σ is the engineering stress, A is the surface area of the flat lattice in the absence of external forces, and ΔA is the "hidden area" which is defined as the difference between the total surface area of the membrane and the area projected onto the plane containing the boundaries. Unlike equi-biaxial straining of a flat membrane that solely yields in-plane stretching, the straining of a wrinkled membrane involves in-plane stretching and out-of-plane bending, simultaneously. Thus, equation 2.1 has an additional term with respect to conventional linear Hooke's law to capture the bending deformations. Since equation 2.1 shows 1D strain in an equi-biaxial tension test, to convert the 2D area change to 1D extension, a coefficient of ½ is multiplied by $(\Delta A/A)$. We also note that equation 2.1 is not a constitutive law but rather a phenomenological model that can capture the geometric nonlinearity of wrinkled membranes during equi-biaxial straining.

As shown in figure 2.1, the typical stress-strain curve of a wrinkled membrane is composed of a linear part ($\varepsilon_L = \left(1\middle/E^f_{2D}\right)\sigma$), and a nonlinear part ($\varepsilon_{NL} = (1/2)\,(\Delta A(\sigma)/A)$), which converges to $(1/2)\,(\Delta A/A)_{\max}$ at large strains. From equation (2.1), it is then possible to obtain the effective stiffness of the membrane as

$$\frac{1}{E_{\mathrm{eff}}}=\frac{\mathrm{d}\varepsilon}{\mathrm{d}\sigma}=\frac{1}{E_{2D}^{f}}+\frac{1}{E_{2D}^{I}(\sigma)},\tag{2.2}$$

where $E_{2D}^{I}(\sigma)$ can be seen as a stress-dependent nonlinear stiffness term that is in series with a linear spring with constant E_{2D}^{f} (see figure 2.1(b)). Comparing equations (2.1) and (2.2), the hidden area then obeys the relation:

$$\frac{1}{2}\frac{\Delta A(\sigma)}{A}=\int\frac{1}{E_{2D}^{I}(\sigma)}\mathrm{d}\sigma.\tag{2.3}$$

Our goal is to find a symbolic function that best represents the hidden area throughout the wrinkle ironing out process. To capture the physics associated with $E_{2D}^{I}(\sigma)$, we start from the bi-linear model shown schematically in figure 2.1(a)

$$\varepsilon(\sigma)=\begin{cases}\frac{1}{E_{2D}^{0}}\sigma & \sigma\le\sigma_c\\ \frac{1}{E_{2D}^{f}}\sigma+\frac{1}{2}\left(\frac{\Delta A}{A}\right)_{\max} & \sigma_c<\sigma\end{cases}.\tag{2.4}$$

We note that this model's stress-strain curve has two slopes, that are given by the experimentally measurable tangential stiffness E_{2D}^{0} of the wrinkled state at low stress and the intrinsic biaxial modulus of graphene E_{2D}^{f} at high stress. The strain-axis-intercept $(\Delta A/A)_{max}$ of the high stress line can be determined experimentally by analyzing the stress-strain curves of 2D materials and can also be obtained by performing complementary Raman spectroscopy and interferometric profilometry measurements on wrinkled 2D membranes [26]. Therefore, the unknown transition stress σ_c can be obtained from equation (2.4) and the continuity condition of the stress-strain curve, which results in:

$$\sigma_c=\frac{\frac{1}{2}\left(\frac{\Delta A}{A}\right)_{\max}E_{2D}^{0}E_{2D}^{f}}{\left(E_{2D}^{f}-E_{2D}^{0}\right)}.\tag{2.5}$$

To estimate the nonlinear spring response corresponding to wrinkle suppression, we replace $(\Delta A/A)$ in equation (2.3) with $(\Delta A/A)_{\max}\mathrm{g}(\sigma/\sigma_c)$, where $\mathrm{g}(\sigma/\sigma_c)$ is a function that captures the transition between the two linear regions due to the "ironing out" of the wrinkles which will be determined by comparison to MD simulations and experiments in section 4.

2.3. ATOMISTIC MODELING

MD simulations are found to be a powerful tool for investigating the influence of wrinkles on the mechanics and material properties of 2D materials, under different loading conditions [28–34]. Here, to investigate the influence of different wrinkling patterns on the nonlinear mechanics of 2D membranes, we perform MD simulations where we create wrinkles by two means, as shown in figures 2.2(a) and 2.2(b), respectively. Either we apply external force at the boundary to deform the membrane, generate wrinkles and

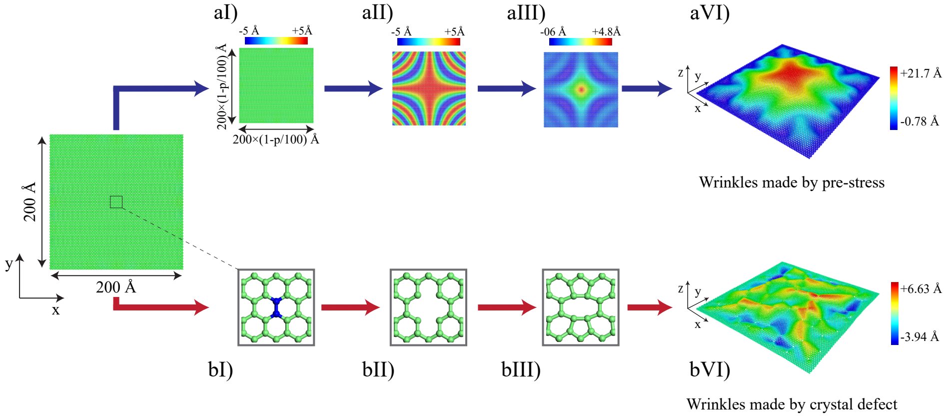

Figure 2.2: The procedure for wrinkle creation in MD simulations. aI) The x, y coordinates are compressed by p%. aII) pre-defined shape functions are employed to impose deviation from flat configuration. aIII) the shape obtained in aII is projected on a Kernel to suppress boundary wrinkles. aIV) the pre-stressed pattern obtained in LAMMPS after minimizing the energy and thermalizing the system. bI) Neighboring atoms are randomly chosen and marked through the lattice. bII) The marked atoms in step bI are removed from the lattice. bIII) Bonds are created manually, and then the bond angles and lengths are modified locally using Materials Studio software. bIV) wrinkled pattern due to crystal defect obtained in LAMMPS after minimizing the energy and thermalizing the system.

subsequently constrain the boundary to preserve them, or we induce crystal defects to obtain out-of-plane imperfections in the absence of boundary force.

In figure 2.2, we detail out the wrinkle creation process in our study. We start by realizing an initial honeycomb square lattice of graphene (200 Å by 200 Å), comprising 15744 atoms. To simulate clamped boundary conditions, we fix atoms within a range of 5 Å from each edge. We then create the wrinkles by two methods. In the first method, the wrinkles are created by compressing the boundary coordinates by p% ($0.5 \le p \le 7$) in both directions (figure 2.2(aI)) and use different shape functions to displace the atoms in the z-direction as a function of x and y coordinates (see figure 2.2(aII)). Finally, to have flat smooth boundaries, we project the obtained shape in figure 2.2(aII) on a kernel that suppresses the wrinkles' height towards boundaries (figure 2.2(aIII)). We label these wrinkled membranes "pre-stressed" samples throughout the manuscript. The details of the wrinkling patterns and the kernel for suppressing boundary wrinkles are given in Appendix 2.A1.

In the second method, we create stress-free wrinkles using crystal defects, following the procedure mentioned in [21]. Briefly, to achieve this second type of wrinkles, we first arbitrarily select sets of two neighboring atoms (d% of total atoms; $0.5 \le d \le 3$) (figure 2.2(bI)) and remove them from the initial lattice (figure 2.2(bII)). Next, we generate the so-called 5-8-5 defects [21] by creating relevant bonds using Materials Studio software (figure 2.2(bIII)).

The resulting atomic coordinates of wrinkled graphene samples are then used as the input for the LAMMPS software [35]. We use Tersoff potential to evaluate atomic interactions [36]. The simulation box walls are built far enough from the graphene edges to avoid numerical interaction between atoms adjacent to the walls, and the boundary conditions are set as periodic. The energy of the system is then minimized with the conjugate-gradient method. To ensure a steady configuration, the created membranes also undergo a canonical ensemble (NVT) for 500 ps. This simulation is carried out using the velocity Verlet integrator with a time step of 1 fs and Nosé-Hoover thermostat with a time constant of 0.01 ps at 4 K. This relatively low temperature is intentionally chosen to suppress thermodynamical ripples in the lattice [37], so as to solely study the effect of statically generated wrinkles by pre-stress or crystal defect. We should note that the presence of static wrinkles can mask the influence of thermal ripples. This is mainly because the contraction due to thermal ripples is much smaller than contractions caused by compressive forces at the boundary [10, 26]. We should also highlight that $T = 4\,\mathrm{K}$ is chosen over $T = 1\,\mathrm{K}$ merely to decrease computational cost and speed up the thermalization process in the wrinkle creation and equilibration after equi-biaxial loading steps. During the minimization and thermalization of the pre-stressed samples, we fix the boundaries in all directions to prevent the stress release. For the samples with crystal defects, though, we only fix the boundaries in the z-direction and allow movement in x- and y to ensure a stress-free configuration. Typical thermalized wrinkled graphene membranes are shown in figures 2.2(aIV) and 2.2(bIV). It is important to note that the formation of pre-strained wrinkles depends on both the initial atomic positions, which are artificially designed as shown in Figure 2.2(aIII), and the thermalization parameters. Consequently, the thermalized configuration depicted in Figure 2.2(aIV) may not represent the only possible configuration. However, the focus of this chapter is not on proving that the pre-strained thermalized configurations are the unique solution, but rather on demonstrating how the ironing out of an initial wrinkle pattern affects the stress-strain response of the membrane.

Moreover, to study the effect of both pre-stress and crystal defects simultaneously, we performed additional simulations in which after creating defects, we compressed the samples and then fixed the boundary coordinates in x, y, and z directions. We shall also emphasize that the pre-stressed wrinkles are made only by compression, and the samples are sufficiently equilibrated in LAMMPS to ensure isotropic behaviour. Moreover, the location of crystal defects are chosen randomly to avoid possible anisotropy of the stress-free wrinkles.

2.4. RESULTS AND DISCUSSION

2.4.1. MD SIMULATIONS

To probe the elasticity of the created samples upon biaxial stretching, we apply pseudo-static tensile strains to the four boundaries in discrete steps of 0.1 ns, (rate of 0.5 Å/ns), with a relaxation period of 0.1 ns. This rate is slow enough to mimic a pseudo-static loading. The stepwise strain-increment is repeated many times to achieve stretching in x- and y-directions. The average biaxial stresses are then obtained by calculating the average normal force at the boundaries and dividing it by the perimeter. The tangential biaxial stiffness is merely the slope of the stress-strain curve at every applied strain.

Figure 2.3(a) shows the stress-strain response of the pre-stressed and defected samples obtained in figure 2.2, along with the elastic response of pristine graphene. We

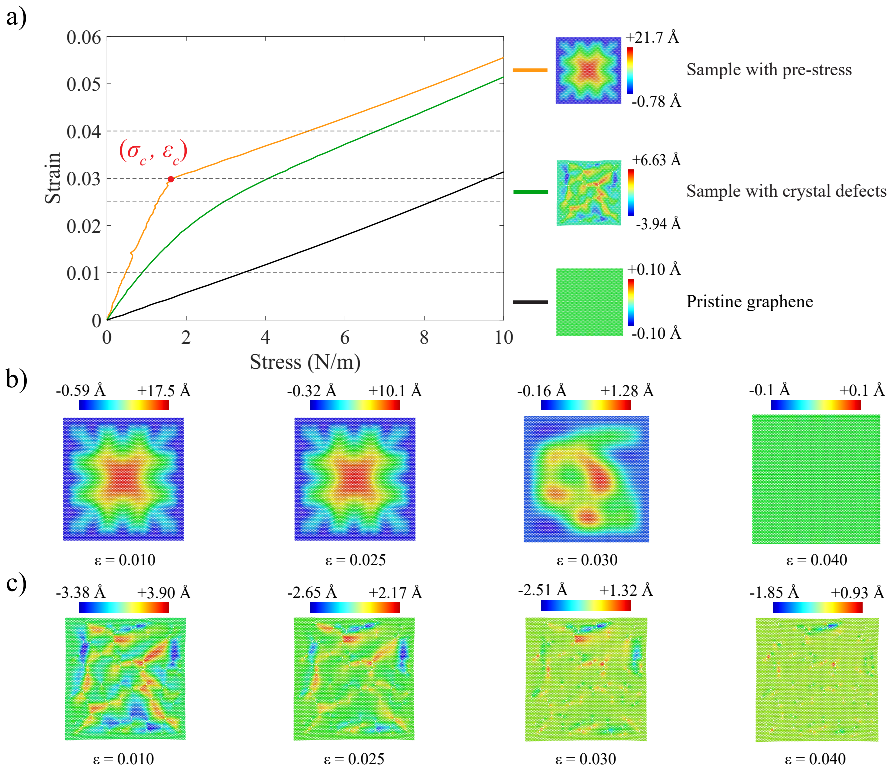

Figure 2.3: Biaxial tensile response of wrinkled graphene with pre-stress (achieved by 2.3% compressive strain in both x and y-directions) and 5-8-5 crystal defects (achieved by 1% defects): a) stress-strain response. Snapshots of the pre-stressed sample upon tension, corresponding to the dashed lines shown in figure 2.3(a), are shown for b) pre-stressed and c) stress-free wrinkled sample. The color-scales demonstrate the local height of wrinkles. The orange line represents the sample with pre-stress, and the green line shows the sample with crystal defects. Moreover, the black line despicts pristine graphene data.

note that the pristine and the defected sample are at their stress-free state at the origin, while the pre-stressed sample is at a compressed state ($p = 2.3$). A linear relationship can be observed between stress and strain for the pristine graphene with a slope of $E^f_{2D} = 330\,\mathrm{N/m}$ that corresponds to the stretching of carbon-carbon bonds. The obtained value of E^f_{2D} matches well the acclaimed high biaxial stiffness of graphene [38–40]. In contrast, for the pre-stressed sample, the stress-strain response is characterized by two slopes, and the sample with crystal defects exhibits nonlinear behavior. We note that the observed nonlinearity is at relatively low strains and is different from the nonlinear response characterized by the negative third-order elastic modulus of graphene [41, 42]. The latter nonlinear response comes into play only at high strains.

To understand how wrinkling patterns evolve with the applied strain, in figures 2.3(b)-(c), we trace the morphology of our graphene samples while straining them. It is interesting to note that for the pre-stressed sample, the wrinkling shape only changes at a critical strain ε_c associated with critical stress σ_c before which only the height of the created wrinkle shrinks. At ε_c, a change in the wrinkling pattern can be observed in figure 2.3(b). We note that the observed pattern is unstable and with a slight additional strain the membrane flattens completely. However, in the sample with crystal defect (see figure 2.3(c)), even at relatively high strains e.g. 4%, the sheet still has buckled regions locally. Movies of the MD simulations associated with the stretching process for both samples are shown in Appendix 2.A2.

To explain the observed morphology change, in figure 2.4(a)-(b), we show the average bond length and the average wrinkle height as a function of the applied biaxial strain, respectively. Interestingly, unlike the sample with crystal defects where a nonlinear trend in the average bond length variation is apparent, for the pre-stressed sample before the critical strain ε_c, the average bond length is $\approx 1.46\,\text{Å}$, that is the stable bond length of the Tersoff potential at 4 K. The reason for this behavior is that the initial thermalization of the wrinkle patterns primarily leads to large-scale bending rather than localized significant strains. As a result, the pre-strain is distributed over the curvatures, creating small tensile and compressive strains. The presence of both compressed and elongated bonds results in an average bond length close to that of pristine graphene at 4 K. This observation suggests that for the pre-stressed sample beyond ε_c, only the atomic bonds of graphene are being stretched, while before ε_c, graphene is subjected to both in-plane and out-of-plane deformation. A similar conclusion can be drawn by tracing the average wrinkle height of the pre-stressed sample (See figure 2.4(b)), where a gradual decrease can be observed till ε_c, after which the wrinkles are ironed out. It is also apparent from the figures that throughout the straining procedure, pristine graphene stays planar, and its bond length varies linearly as a function of strain.

2.4.2. SYMBOLIC REGRESSION OF MD DATA

Next, to obtain an analytic expression that captures the observed nonlinearity, we determine $\mathrm{g}(\sigma/\sigma_c)$. For this, we convert the $\varepsilon(\sigma)$ curves from the MD data into $\Delta A(\sigma)/A$ curves using equation (2.4). By doing so we can eliminate the contribution of Hooke's law from the data-sets and use Eureqa to determine only the hidden area symbolically. We also make the data-sets dimensionless by dividing stress by σ_c, and to retain only $\mathrm{g}(\sigma/\sigma_c)$ in the fitting procedure, we divide the strain by $(1/2)\,(\Delta A/A)_{\max}$. We obtain the

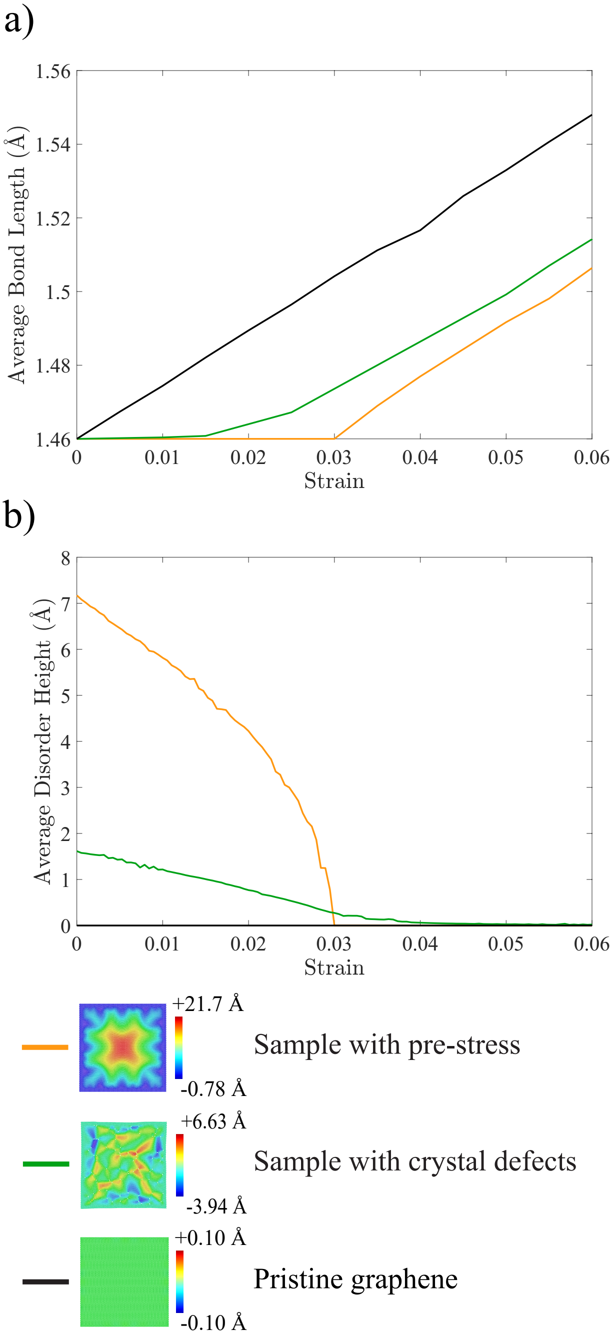

Figure 2.4: Average bond length and wrinkle height as a function of strain. a) Average carbon-carbon bond-length of the samples; b) Average sample height calculated by $\frac{1}{N}\sum_{i=1}^{N}\left|z_i\right|$ (N: total number of atoms, z_i: the z-coordinate of the atom i). The color-scales demonstrate the local height of wrinkles. The orange line represents the sample with pre-stress, and the green line shows the sample with crystal defects. Moreover, the black line depicts pristine graphene data.

normalized function g(σ/σ_c) for 38 wrinkling configurations. These patterns include 24 wrinkled membranes with pre-stress created in a similar fashion to figure 2.2(aIV), 10 samples with crystal defects obtained similar to figure 2.2(bIV), and 4 graphene membranes that have both pre-stress and crystal defect (see Appendix 2.A1). In figure 2.5 we show the normalized response of seven of these membranes, and in table 2.1 we report the corresponding bi-linear fits using equation (2.4). It is interesting to note that all the samples created by crystal defects follow the same trend of nonlinearity irrespective of the shape and height of wrinkles (samples D, E, and F). The same observation holds true for the samples made by pre-stress (samples A, B, and C) where a bi-linear response is apparent. We note that the stress-strain response of samples with both pre-stress and crystal defects lies within the response of the wrinkled membranes made by crystal defect and those made by pre-stress only (see sample G).

To analytically describe the stress-strain characteristics of membranes with different types of wrinkles, it is thus interesting to obtain a phenomenological equation that can capture all the observed curves g(σ/σ_c) . To this end, we import the normalized stress-strain data (g(σ/σ_c)) into the Eureqa symbolic regression software to automatically search for a function space using a selected set of operators and operands [43]. Eureqa uses genetic programming to search for mathematical equations that best describe a set of data and has been successfully used to distill physical laws of motion from experimental data [43, 44]. The output of Eureqa is a set of possible fitting functions (Pareto Front) ranked based on the mean absolute error and a complexity index that balances the complexity of the proposed models, measured as the number of terms included in the model (see Appendix 2.A3). The obtained models from Eureqa were either overfitting the MD data or contained few fitting parameters. Among the proposed models the following symbolic function is found to fit both samples with pre-stress and crystal defects with high accuracy:

$$\varepsilon = \frac{1}{E_{2D}^{f}}\sigma + \frac{1}{2}\left(\frac{\Delta A}{A}\right)_{\max}\left[\frac{\sigma}{\sigma_c + \exp\left(-\left(\frac{\sigma}{\sigma_c}\right) - \beta\left(\frac{\sigma}{\sigma_c}\right)^4\right)}\right] \tag{2.6}$$

In this model, the nonlinear spring can be well-approximated by three physically meaningful and measurable parameters namely E_{2D}^{f}, σ_c and $(\Delta A/A)_{\max}$ in addition to the fitting parameter β that determines the degree of nonlinearity. We note that in the limit of $\beta \rightarrow 1$, equation (2.6) is seen to represent the response of wrinkled membranes made by pre-stress well, while in the limit of $\beta \rightarrow 0.1$, stress-free wrinkled membranes can be best fitted (See figure 2.5). Moreover, we observe that the mechanical response of samples made by a combination of pre-stress and crystal defects can be well-captured by $0.1 < \beta < 1$ (see table 2.A4 in the Appendix). We also note that for $\beta \rightarrow -\infty$, the nonlinear term of equation (2.6) tends to zero and Hooke's law is retrieved. The fits to all 38 samples using equation (2.6) are given in the Appendix. The presented phenomenological model can capture the nonlinear response of a large set of wrinkled membranes, with functional form being obtained directly from MD fits . It is important to note that there might be wrinkling patterns that cannot be captured by equation 2.6, e.g., wrinkles made by shear. Thus, more MD work will be needed to establish the range of validity of

Table 2.1: Bilinear approximation (equation (2.4)) parameters corresponding to the samples A-G, explained in figure 2.5.

	$E_{2D}^{f}(\mathrm{N\,m^{-1}})$	$(\Delta A/A)_{max}$	$\sigma_c(\mathrm{N\,m^{-1}})$
Sample A	326.3	0.047	1.244
Sample B	332.7	0.046	1.321
Sample C	308.6	0.042	1.971
Sample D	282.5	0.031	1.858
Sample E	258.2	0.045	2.621
Sample F	286.0	0.029	1.941
Sample G	309.3	0.043	1.478

the presented phenomenological model.

It is interesting to note that in statistical mechanics studies [45], there also exists a parameter α that expresses the degree of nonlinearity in wrinkled membranes, and it was shown that in stress-free wrinkled membranes, irrespective of wrinkling pattern, the nonlinear behavior can be modelled as:

$$\varepsilon(\sigma) = \frac{1}{E_{2D}^{f}}\sigma + \frac{\sigma_*}{\alpha E_{2D}^{f}}\left(\frac{\sigma}{\sigma_*}\right)^{\alpha}, \tag{2.7}$$

with $\alpha \approx 0.1$ for statically wrinkled membranes, and σ_* being a re-normalization parameter set as the stress at which $E_{2D}^{I}(\sigma) = E_{2D}^{f}(\sigma/\sigma_*)^{1-\alpha}$, that is when the nonlinear stiffness of equation (2.7) is equal to the linear stiffness term E_{2D}^{f} [45] .

It was found that it is difficult to accurately fit the MD data with the physics based equation (2.7), which is why the phenomenological equation (2.6) is introduced, that matches the MD simulations with high accuracy.

2.4.3. VALIDATION OF THE MODEL USING EXPERIMENTAL DATA

In order to show the applicability of equation (2.6) in fitting experimental data and to compare its outcome to equation (2.7), we fit the stress-strain measurements for single-layer graphene membranes reported in [26] using both equation (2.6) (in figure 2.6(b)) and equation (2.7) (in figure 2.6(a)). The graphene membranes in the experiments [26] were suspended over 5μm circular cavities and pressurized by nitrogen gas while their strain was probed by both Raman spectroscopy and interferometric profilometry. Before fitting, first the Raman spectroscopy values for the strain were subtracted from interferometric measurements. Thus, the experimental data of Ref. [26] only contain the nonlinear strain ε_{NL} corresponding to $(1/2)(\Delta A(\sigma)/A)$ (see figure 2.1(a)). In order to account for the offset seen in the data at the beginning of the measurements, σ and σ_* in equation (2.7) were replaced with $\sigma - \sigma_0$ and $\sigma_* - \sigma_0$, respectively with σ_0 being an un-known pre-stress. Then, α, σ_* and σ_0 were chosen as the fitting parameters. The obtained values from the fits in [26] were $\alpha = 0.12 \pm 0.02$, $\sigma_* = 0.8 \pm 0.1$ N/m, and $\sigma_0 = 0.07 \pm 0.01$ N/m.

Although the obtained fits provide good insight and confirm deviation from Hooke's law in wrinkled membranes, it appears that with increasing stress, the fitted curves in

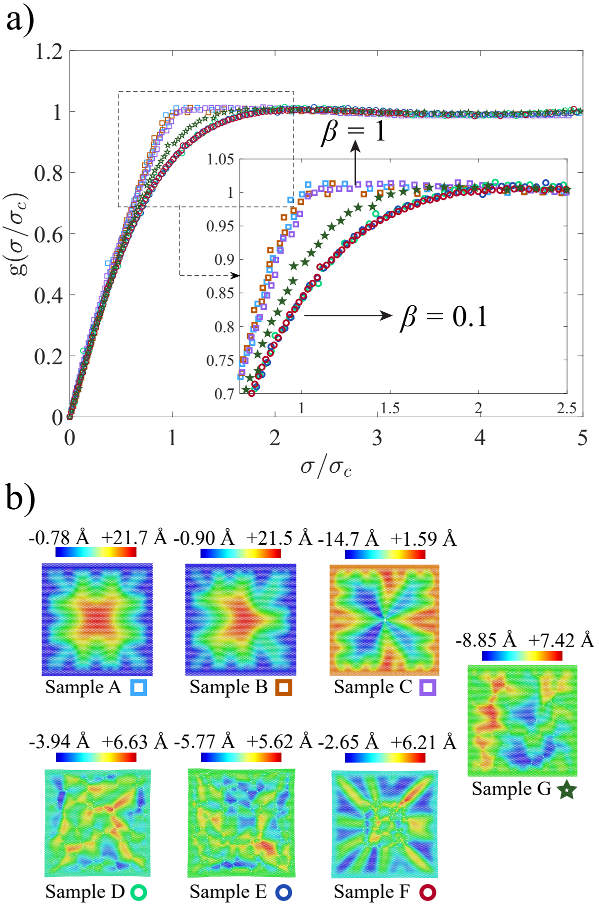

Figure 2.5: Uniqueness of degree of nonlinearity for samples with pre-stress and crystal defects. a) $g(\sigma/\sigma_c)$ for seven different samples including: A, B, and C pre-stressed graphene with 2.3%, 2.3%, and 2.1% pre-stress; D, and E, graphene with randomly distributed 1% and 2% crystal defects; F, graphene with 1% locally created defects; G, graphene with 2.1% pre-stress and 0.5% crystal defects. b) Corresponding graphene samples with different wrinkle types/patterns at the start of stretching. The color-scales demonstrate local wrinkle height and the color symbols shown below each sample represents the corresponding data in figure 2.5(a). The corresponding parameters obtained from MD simulations, and used for normalizing the stress-strain data are presented in table 2.1.

figure 2.6(a) deviate from the experimental data. A possible reason for this deviation is that the model proposed in [45] is derived for membranes that exhibit stress-free out-of-plane fluctuations and does not account for the pre-stress often present after the fabrication of graphene membranes. Another reason might be the finite bending rigidity of graphene which results in the non-zero stiffness that samples show at low stress, before ironing out the wrinkles (see Figure 2.6).

For comparison, in figure 2.6 (b) we show the fits of experimental data using equation (2.6). To capture the nonlinear behavior, we use $(\Delta A/A)_{\max}$ and σ_c as the fitting parameters and fix $\beta = 1$, that is the degree of nonlinearity obtained from our MD simulations for pre-stressed wrinkled membranes. Similar to the procedure performed in [26], we also add a constant term σ_0 to equation (2.6) to account for the offset observed at the onset of experiments. Using these fitting parameters, we find $(\Delta A/A)_{\max} = 0.008 \pm 0.002$, $\sigma_c = 0.45 \pm 0.2$ N/m, $\sigma_0 = 0.065 \pm 0.065$ N/m and find good fits to the nonlinear stress-strain trends observed experimentally.

It is worth noting that the parameter β is a qualitative measure of the smoothness of the transition between the two straight parts of the stress-strain curve. For $\beta = 1$ this transition is a sharp kink, a situation that corresponds to pre-stressed graphene, whereas for $\beta = 0.1$, the transition is more smooth, a situation that is representative of crystal defect induced wrinkles. Further theoretical work is required to clarify the physical origin of the proposed functional form for the hidden area of wrinkled 2D materials, and the effect of defects and wrinkles on the value of β. Such theoretical work should be carried out using statistical mechanics theory of membranes with crystalline or hexatic order similar to [45] or [46] accounting for the pre-stress effect. It would be interesting to see if such models obtain a nonlinear function for wrinkle ironing out process similar to our symbolic regression approximation.

We shall stress that the fits presented are aimed at demonstrating that the force-deflection curves of experimental data can be well-captured by the presented phenomenological model; thus the range of applicability of the model is not limited to MD simulations. However, the fitting values obtained for the experimental data are certainly not comparable to the values obtained for the MD results, especially since the exact experimental wrinkling structure is unknown and different from the MD simulations.

2.5. CONCLUSIONS

In conclusion, we study the effect of wrinkles on the mechanics of graphene using molecular dynamics simulations and obtain bilinear stress-strain characteristics consisting of 2 linear regions, a low stress region that is related to the ironing out of the wrinkles and a high-stress region which is governed by the intrinsic stiffness of graphene. We show that the type of wrinkles influences the smoothness of the transition between these regions. Whereas wrinkles created by crystal defects in stress-free membranes result in a smooth and gradual transition, wrinkles generated by pre-stressing of graphene by its edges result in a much sharper transition. To capture and characterize these observations, we present a phenomenological model in terms of physically measurable quantities and a fitting parameter β, that determines the degree of nonlinearity and sharpness of the transition. Using this model, we find that membranes with crystal defects and pre-stress each exhibit their unique degrees of nonlinearity irrespective of their wrinkling patterns.

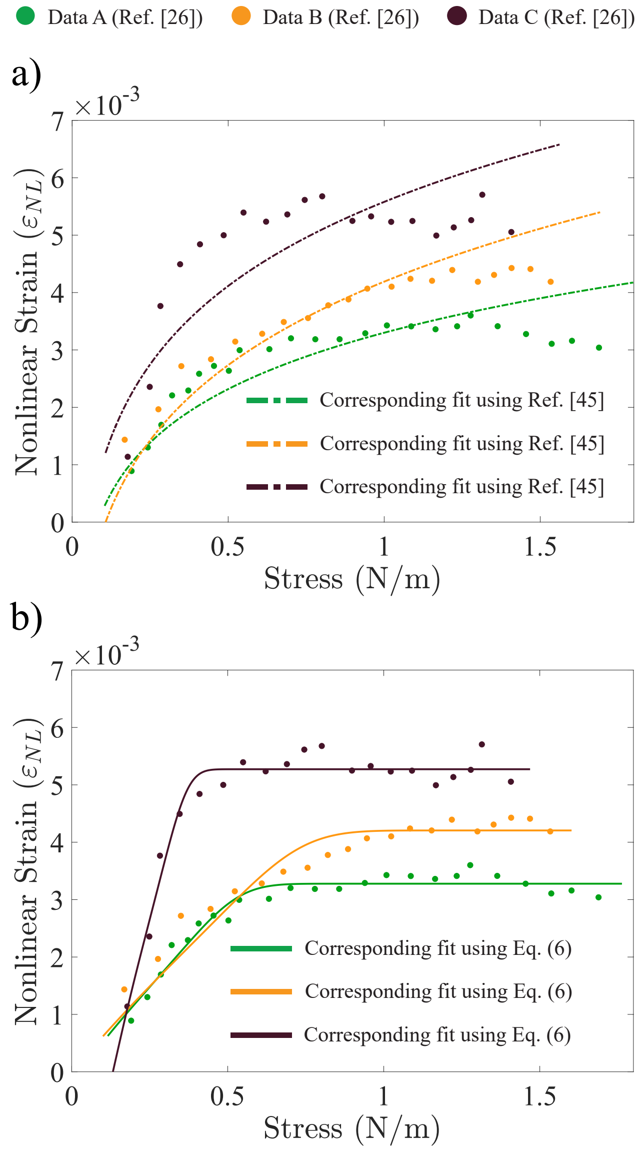

Figure 2.6: Fits of the experimental stress-strain data reported in reference [26]. a) Fits obtained using the power-law relation proposed by Gornyi et al. [45]. b) Curves obtained by fitting the data with (equation (2.6)).

Our results suggest that the proposed model can be potentially used to estimate the type of disorder in suspended 2D material membranes by experimentally probing their nonlinear elasticity.

APPENDIX

2.A1. WRINKLE CREATION

The initial configuration of graphene (atoms' coordinates), alongside the force field, are the inputs for the LAMMPS software. We use shape kernels to obtain a desired initial shape with non-uniform stress distribution along x and y-direction (figure 1-aII). We also use the following three shape functions (figures 2.A1a-c) to induce out-of-plane deviations:

$$\begin{aligned} P_a &= \cos\left(\lambda\pi\frac{1}{\sqrt{2}}\sqrt{\frac{\left(x-\frac{a}{2}\right)^2}{\frac{a}{2}}+\frac{\left(y-\frac{a}{2}\right)^2}{\frac{a}{2}}}\right) & \lambda &= 2n+1 \\ P_b &= \cos\left(\lambda\pi\frac{\left(x-\frac{a}{2}\right)}{\frac{a}{2}}\times\frac{\left(y-\frac{a}{2}\right)}{\frac{a}{2}}\right) & \lambda &= 2n+1 \\ P_c &= \cos\left(\frac{\lambda\pi}{2}\arctan\left(\frac{\left(x-\frac{a}{2}\right)}{\left(y-\frac{a}{2}\right)}\right)\right) & \lambda &= 2n \end{aligned} \tag{2.A1}$$

where a is the length of the side of the square lattice (here 200 Å), and $n \in \mathbb{N}$. P_a, P_b, and P_c are the z-coordinates of the patterns obtained by the above-mentioned shape functions.

Since the functions induce large deflections throughout the lattice,together with them we use a smoothing kernel to suppress deflections close to the boundaries (figure 1-aIII). The smoothing kernel is defined as

$$S = \exp\left(-C\frac{1}{\sqrt{2}}\sqrt{\left(\frac{\left(x-\frac{a}{2}\right)}{\frac{a}{2}}\right)^2+\left(\frac{\left(y-\frac{a}{2}\right)}{\frac{a}{2}}\right)^2}\right) \tag{2.A2}$$

where C is a constant determining the degree of smoothness. In order to avoid any edge deflection, we should use high values of C. However, in some of the samples, C is assigned to lower values to obtain different wrinkling patterns.

The final lattice configuration, used as the input to LAMMPS, is obtained by:

$$Z = H \times P_i \times S \quad i = a, b, c \tag{2.A3}$$

where $H = a/10$ is the maximum height of wrinkle pattern.

Using the aforementioned shape functions, we input the coordinates into LAMMPS and created 24 pre-stressed samples shown in figure 2.A2. Additionally, we created 10 samples with crystal defects following the procedure mentioned in [21], and 4 samples containing both defects and pre-stress, simultaneously. The thermalized stable configuration for all samples after using LAMMPS is shown in figures 2.A3 and 2.A4.

2.A2. SYMBOLIC REGRESSION

In order to find the function $g(\sigma/\sigma_c)$, we used Eureqa symbolic regression toolbox. The normalized data corresponding to the nonlinear part of the stress-strain curves (shown

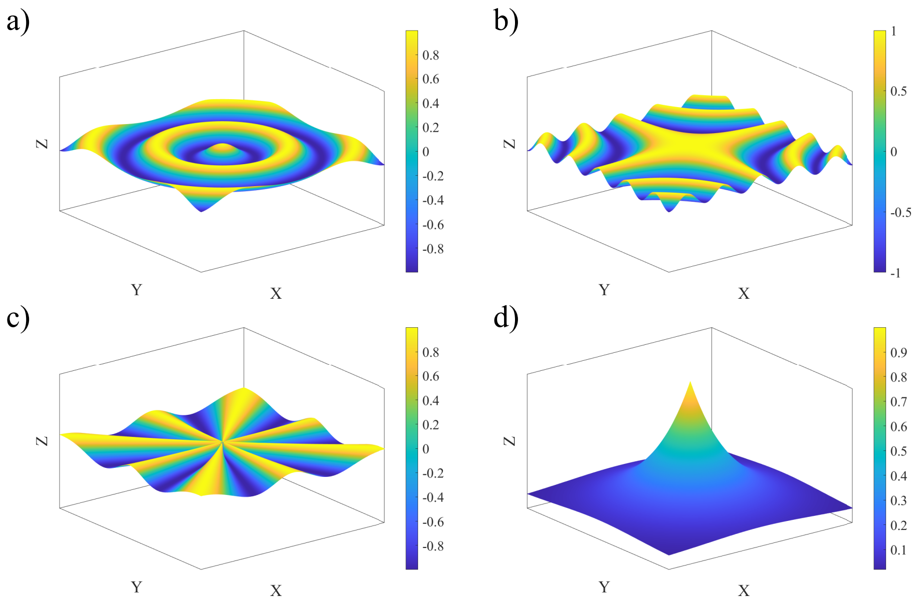

Figure 2.A1: Shape kernels, corresponding to equation 2.A1 (a-c) and smoothing kernel, corresponding to equation 2.A2 (d).

Table 2.A1: The symbolic functions proposed by Eureqa's Pareto front using the nonlinear curve of figure 5, to approximate g(σ/σ_c).

	Absolute Error	Complexity	g(x)
1	0.00828	5	$\tanh(x)$
2	0.02169	8	$1-\exp(-x)$
3	0.01170	11	$\frac{x}{x+\exp(-x)}$
4	0.00732	14	$1-\frac{1}{x+\exp\left(x^2\right)}$
5	0.00433	18	$\frac{x}{x+\exp\left(-x-\beta x^4\right)}$
6	0.00223	40	$1.26+0.01x^2-0.1x-1.3\exp(-1.7x)-x\exp(-\frac{0.003}{0.2-x}-1.8x)$

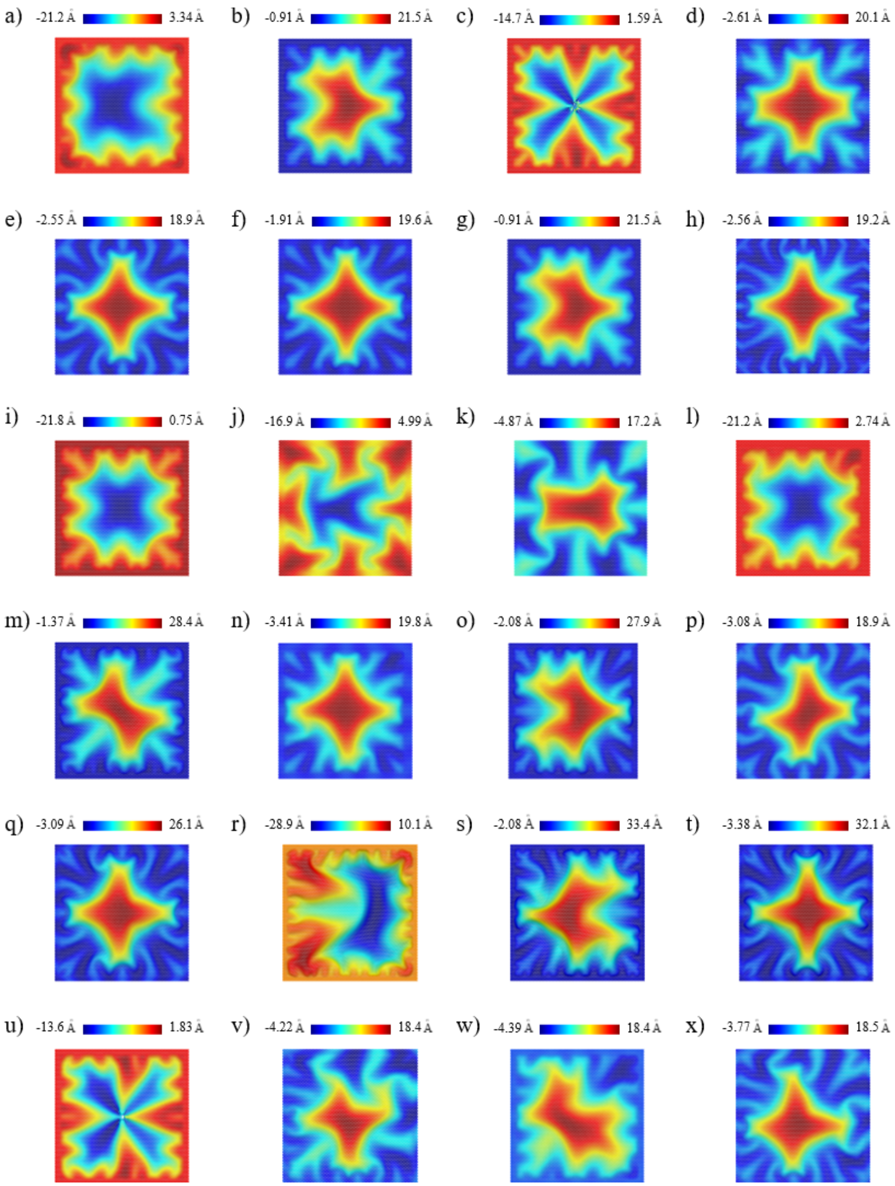

Figure 2.A2: Wrinkled samples made by compressive force at the boundaries visualized by OVITO [47]. Samples are labelled for future reference (see table 2.A2).

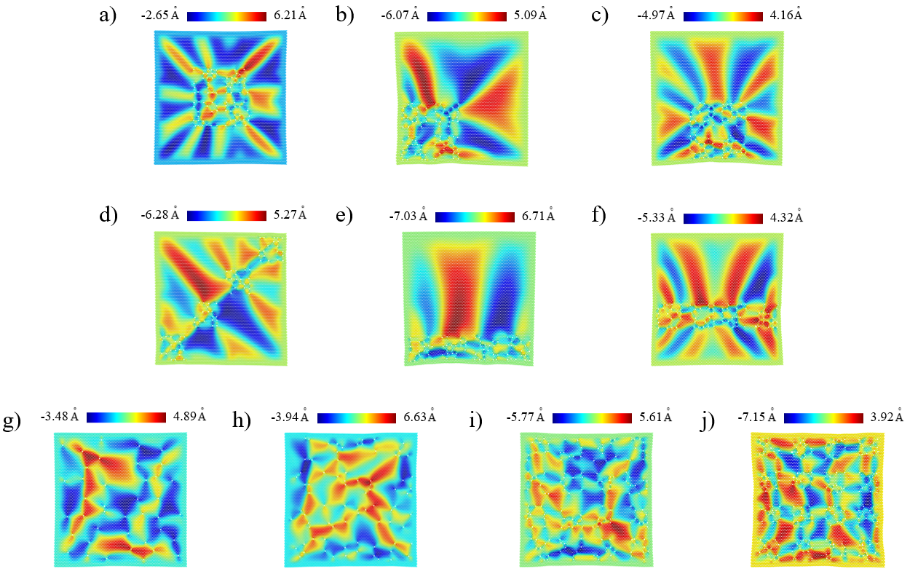

Figure 2.A3: Wrinkles made by crystal defects visualized by OVITO [47]. Samples are labelled for future reference (see table 2.A3).

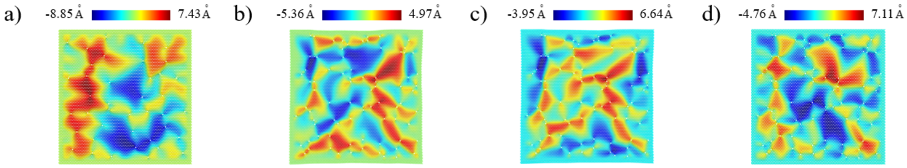

Figure 2.A4: Wrinkles made by combination of compressive force and crystal defects visualized by OVITO [47]. Samples are labelled for future reference (see table 2.A4).

in figure 5 of the main text), is used as the input for the algorithm. For symbolic regression of the data, we limited The choice of functions in order to avoid high computation times. For example, we did not choose the sine or cosine function in the fits since there was no periodicity in our datasets. Other than polynomials which are the default functions used by Eureqa, different operators, operands, and functions were chosen for approximating $g(\sigma/\sigma_c)$. These included $\{+,-,*,/,\exp\}$, $\{+,-,*,/,\log\}$, $\{+,-,*,/,\sqrt[2]{}\}$, $\{+,-,*,/,\tanh\}$, and $\{+,-,*,/,\mathrm{asinh},\mathrm{acosh}\}$.

The bilinear and the nonlinear datasets (shown in figure 5 of the manuscript) corresponding to the wrinkled samples made by pre-stress and crystal defects were then fitted to find the desired function. A limited list of proposed expressions by Eureqa, their absolute errors and complexities is shown in table 2.A1. Constant numbers are rounded up or down with a roundoff error of 0.1. Some of the obtained expressions overfit the data by containing too many fitting parameters. Function number 6 in table 2.A1 is an example of one such functions that overfit the stress-strain data. Among the obtained expressions only function 5 appeared to fit both the data of samples with crystal defects and pre-stress. In particular, this function could capture the bilinear dataset (wrinkles made by pre-stress) with $\beta = 1$ and the nonlinear data (wrinkles made by crystal defects) with $\beta = 0.1$. Using graphene samples with a combination of defects and pre-stress, still this function was found in the Pareto front; however, with different β values, that vary between 0.1 to 1. These observations led us to select the 6th expression of table S1 as the outcome of symbolic regression and for predicting the stress-strain relationship of disordered graphene.

2.A3. FITTING VALUES OBTAINED FROM MD DATA

The stress-strain data corresponding to the samples shown in figures 2.A2 to 2.A4 are fitted using equation 6 of table S1, and the resulting fitting parameters are presented in tables 2.A2 to 2.A4.

BIBLIOGRAPHY

[1] Yang, L., Niu, T., Zhang, H., Xu, W., Zou, M., Xu, L., Cao, G. and Cao, A., 2017. Self-assembly of suspended graphene wrinkles with high pre-tension and elastic property. 2D Materials, 4(4), p.041001.

[2] Meng, L., Li, Y., Liu, T.S., Zhu, C., Li, Q.Y., Chen, X., Zhang, S., Zhang, X., Bao, L., Huang, Y. and Xu, F., 2020. Wrinkle networks in exfoliated multilayer graphene and other layered materials. Carbon, 156, pp.24-30.

[3] Lanza, M., Wang, Y., Bayerl, A., Gao, T., Porti, M., Nafria, M., Liang, H., Jing, G., Liu, Z., Zhang, Y. and Tong, Y., 2013. Tuning graphene morphology by substrate towards wrinkle-free devices: Experiment and simulation. Journal of Applied Physics, 113(10), p.104301.

[4] Chen, W., Gui, X., Yang, L., Zhu, H. and Tang, Z., 2019. Wrinkling of two-dimensional materials: methods, properties and applications. Nanoscale horizons, 4(2), pp.291-320.

Table 2.A2: Fitting parameters of the proposed equation 6 to the samples of figure 2.A2.

	Proposed equation			
	$E_{2D}^{f}(\mathrm{N\,m^{-1}})$	$(\Delta A/A)_{\max}$	$\sigma_c(\mathrm{N\,m^{-1}})$	β
a	335.3	0.04631	1.296	1
b	333.3	0.04597	1.322	1
c	322.3	0.04382	1.542	1
d	326.8	0.04568	1.174	1
e	319.9	0.04528	1.136	1
f	328.7	0.04623	1.151	1
g	333.3	0.04597	1.322	1
h	314.0	0.04536	1.132	1
i	326.9	0.04679	1.245	1
j	312.2	0.04481	1.115	1
k	307.5	0.04377	1.234	1
l	334.3	0.04350	1.525	1
m	314.9	0.08731	2.308	1
n	343.0	0.04344	1.517	1
o	316.5	0.08828	2.332	1
p	319.7	0.04538	1.060	1
q	311.8	0.0889	1.828	1
r	319.3	0.1291	3.521	1
s	328.0	0.1313	3.659	1
t	310.0	0.1321	2.742	1
u	308.6	0.0418	1.971	1
v	307.9	0.0443	1.218	1
w	312.5	0.0425	1.541	1
x	306.3	0.0449	1.070	1

Table 2.A3: Fitting parameters of the proposed equation 6 to the samples of figure 2.A3.

	Proposed equation			
	$E^{f}_{2D}(\mathrm{N\,m^{-1}})$	$(\Delta A/A)_{\max}$	$\sigma_c(\mathrm{N\,m^{-1}})$	β
a	279.6	0.02786	1.814	0.1
b	253.6	0.01705	1.639	0.1
c	257.4	0.01709	1.342	0.1
d	279.5	0.02391	1.581	0.1
e	255.3	0.01534	1.761	0.1
f	261.5	0.02292	2.011	0.1
g	271.7	0.01605	1.186	0.1
h	277.5	0.02932	1.746	0.1
i	247.3	0.04128	2.399	0.1
j	224.8	0.05495	3.734	0.1

Table 2.A4: Fitting parameters of the proposed equation 6 to the samples of figure 2.A4.

	Proposed equation			
	$E^{f}_{2D}(\mathrm{N\,m^{-1}})$	$(\Delta A/A)_{\max}$	$\sigma_c(\mathrm{N\,m^{-1}})$	β
a	309.6	0.04248	1.479	0.3
b	272.5	0.02871	1.665	0.11
c	274.1	0.02872	1.719	0.12
d	292.3	0.04039	1.731	0.28

[5] Guinea, F., Horovitz, B. and Le Doussal, P., 2009. Gauge fields, ripples and wrinkles in graphene layers. Solid State Communications, 149(27-28), pp.1140-1143.

[6] Deng, S. and Berry, V., 2016. Wrinkled, rippled and crumpled graphene: an overview of formation mechanism, electronic properties, and applications. Materials Today, 19(4), pp.197-212.

[7] Pereira, V.M., Neto, A.C., Liang, H.Y. and Mahadevan, L., 2010. Geometry, mechanics, and electronics of singular structures and wrinkles in graphene. Physical review letters, 105(15), p.156603.

[8] Gao, W. and Huang, R., 2014. Thermomechanics of monolayer graphene: Rippling, thermal expansion and elasticity. Journal of the Mechanics and Physics of Solids, 66, pp.42-58.

[9] Lee, S., 2015. Effect of intrinsic ripples on elasticity of the graphene monolayer. Nanoscale research letters, 10(1), pp.1-9.

[10] Nicholl, R.J., Conley, H.J., Lavrik, N.V., Vlassiouk, I., Puzyrev, Y.S., Sreenivas, V.P., Pantelides, S.T. and Bolotin, K.I., 2015. The effect of intrinsic crumpling on the mechanics of free-standing graphene. Nature communications, 6(1), pp.1-7.

[11] Rakshit, B. and Mahadevan, P., 2010. Absence of rippling in graphene under biaxial tensile strain. Physical Review B, 82(15), p.153407.

[12] Fasolino, A., Los, J.H. and Katsnelson, M.I., 2007. Intrinsic ripples in graphene. Nature materials, 6(11), pp.858-861.

[13] Sajadi, B., Wahls, S., van Hemert, S., Belardinelli, P., Steeneken, P.G. and Alijani, F., 2019. Nonlinear dynamic identification of graphene's elastic modulus via reduced order modeling of atomistic simulations. Journal of the Mechanics and Physics of Solids, 122, pp.161-176.

[14] Vandeparre, H., Piñeirua, M., Brau, F., Roman, B., Bico, J., Gay, C., Bao, W., Lau, C.N., Reis, P.M. and Damman, P., 2011. Wrinkling hierarchy in constrained thin sheets from suspended graphene to curtains. Physical Review Letters, 106(22), p.224301.

[15] Janssens, S.D., Sutisna, B., Giussani, A., Kwiecinski, J.A., Vázquez-Cortés, D. and Fried, E., 2020. Boundary curvature effect on the wrinkling of thin suspended films. Applied Physics Letters, 116(19), p.193702.

[16] Ho, D.T., Park, H.S., Kim, S.Y. and Schwingenschlogl, U., 2020. Graphene origami with highly tunable coefficient of thermal expansion. ACS nano, 14(7), pp.8969-8974.

[17] Zhao, S., Zhang, Y., Yang, J. and Kitipornchai, S., 2021. Significantly improved interfacial shear strength in graphene/copper nanocomposite via wrinkles and functionalization: A molecular dynamics study. Carbon, 174, pp.335-344.

[18] Wang, Z.F., Zhang, Y. and Liu, F., 2011. Formation of hydrogenated graphene nanoripples by strain engineering and directed surface self-assembly. Physical Review B, 83(4), p.041403.

[19] Akinwande, D., Brennan, C.J., Bunch, J.S., Egberts, P., Felts, J.R., Gao, H., Huang, R., Kim, J.S., Li, T., Li, Y. and Liechti, K.M., 2017. A review on mechanics and mechanical properties of 2D materials—Graphene and beyond. Extreme Mechanics Letters, 13, pp.42-77.

[20] Qin, H., Sun, Y., Liu, J.Z. and Liu, Y., 2016. Mechanical properties of wrinkled graphene generated by topological defects. Carbon, 108, pp.204-214.

[21] Grima, J.N., Winczewski, S., Mizzi, L., Grech, M.C., Cauchi, R., Gatt, R., Attard, D., Wojciechowski, K.W. and Rybicki, J., 2015. Tailoring graphene to achieve negative Poisson's ratio properties. Advanced materials, 27(8), pp.1455-1459.

[22] Yoon, D., Son, Y.W. and Cheong, H., 2011. Negative thermal expansion coefficient of graphene measured by Raman spectroscopy. Nano letters, 11(8), pp.3227-3231.

[23] Katsnelson, M.I. and Fasolino, A., 2013. Graphene as a prototype crystalline membrane. Accounts of chemical research, 46(1), pp.97-105.

[24] Sajadi, B., van Hemert, S., Arash, B., Belardinelli, P., Steeneken, P.G. and Alijani, F., 2018. Size-and temperature-dependent bending rigidity of graphene using modal analysis. Carbon, 139, pp.334-341.

[25] Cao, K., Feng, S., Han, Y., Gao, L., Ly, T.H., Xu, Z. and Lu, Y., 2020. Elastic straining of free-standing monolayer graphene. Nature communications, 11(1), pp.1-7.

[26] Nicholl, R.J., Lavrik, N.V., Vlassiouk, I., Srijanto, B.R. and Bolotin, K.I., 2017. Hidden area and mechanical nonlinearities in freestanding graphene. Physical review letters, 118(26), p.266101.

[27] Yoo, C.H. and Lee, S., 2011. Stability of structures: principles and applications. Elsevier.

[28] Baimova, J.A., Dmitriev, S.V., Zhou, K. and Savin, A.V., 2012. Unidirectional ripples in strained graphene nanoribbons with clamped edges at zero and finite temperatures. Physical Review B, 86(3), p.035427.

[29] Neek-Amal, M. and Peeters, F.M., 2010. Graphene nanoribbons subjected to axial stress. Physical Review B, 82(8), p.085432.

[30] Baimova, J.A., Dmitriev, S.V. and Zhou, K., 2012. Strain-induced ripples in graphene nanoribbons with clamped edges. physica status solidi (b), 249(7), pp.1393-1398.

[31] Duan, W.H., Gong, K. and Wang, Q., 2011. Controlling the formation of wrinkles in a single layer graphene sheet subjected to in-plane shear. Carbon, 49(9), pp.3107-3112.

[32] Jing, N., Xue, Q., Ling, C., Shan, M., Zhang, T., Zhou, X. and Jiao, Z., 2012. Effect of defects on Young's modulus of graphene sheets: a molecular dynamics simulation. Rsc Advances, 2(24), pp.9124-9129.

[33] He, L., Guo, S., Lei, J., Sha, Z. and Liu, Z., 2014. The effect of Stone–Thrower–Wales defects on mechanical properties of graphene sheets–A molecular dynamics study. Carbon, 75, pp.124-132.

[34] Leyssale, J.M. and Vignoles, G.L., 2014. A large-scale molecular dynamics study of the divacancy defect in graphene. The Journal of Physical Chemistry C, 118(15), pp.8200-8216.

[35] Plimpton, S., 1995. Fast parallel algorithms for short-range molecular dynamics. Journal of computational physics, 117(1), pp.1-19.

[36] Tersoff, J.J.P.R.B., 1989. Modeling solid-state chemistry: Interatomic potentials for multicomponent systems. Physical review B, 39(8), p.5566.

[37] Zhang, Y. and Wang, L., 2018. Thermally stimulated nonlinear vibration of rectangular single-layered black phosphorus. Journal of Applied Physics, 124(13), p.135101.

[38] Kudin, K.N., Scuseria, G.E. and Yakobson, B.I., 2001. C 2 F, BN, and C nanoshell elasticity from ab initio computations. Physical Review B, 64(23), p.235406.

[39] Davidovikj, D., Alijani, F., Cartamil-Bueno, S.J., van der Zant, H.S., Amabili, M. and Steeneken, P.G., 2017. Nonlinear dynamic characterization of two-dimensional materials. Nature communications, 8(1), pp.1-7.

[40] Sajadi, B., Alijani, F., Davidovikj, D., Goosen, J., Steeneken, P.G. and van Keulen, F., 2017. Experimental characterization of graphene by electrostatic resonance frequency tuning. Journal of Applied Physics, 122(23), p.234302.

[41] Cadelano, E., Palla, P.L., Giordano, S. and Colombo, L., 2009. Nonlinear elasticity of monolayer graphene. Physical review letters, 102(23), p.235502.

[42] Lee, C., Wei, X., Kysar, J.W. and Hone, J., 2008. Measurement of the elastic properties and intrinsic strength of monolayer graphene. science, 321(5887), pp.385-388.

[43] Schmidt, M. and Lipson, H., 2009. Distilling free-form natural laws from experimental data. science, 324(5923), pp.81-85.

[44] Bongard, J. and Lipson, H., 2007. Automated reverse engineering of nonlinear dynamical systems. Proceedings of the National Academy of Sciences, 104(24), pp.9943-9948.

[45] Gornyi, I.V., Kachorovskii, V.Y. and Mirlin, A.D., 2016. Anomalous Hooke's law in disordered graphene. 2D Materials, 4(1), p.011003.

[46] Roldán, R., Fasolino, A., Zakharchenko, K.V. and Katsnelson, M.I., 2011. Suppression of anharmonicities in crystalline membranes by external strain. Physical Review B, 83(17), p.174104.

[47] Stukowski, A., 2009. Visualization and analysis of atomistic simulation data with OVITO–the Open Visualization Tool. Modelling and simulation in materials science and engineering, 18(1), p.015012.

3

3

STRESS DISTRIBUTION IN SUSPENDED MEMBRANES

Suspended drums made of 2D materials hold potential for sensing applications. However, the industrialization of these applications is hindered by significant device-to-device variations presumably caused by non-uniform stress distributions induced by the fabrication process. Here we introduce a methodology to determine the stress distribution from their mechanical resonance frequencies and corresponding mode shapes as measured by a laser Doppler vibrometer (LDV). To avoid limitations posed by the optical resolution of the LDV, we leverage a manufacturing process to create ultra-large graphene drums with diameters of up to 1000 μm. *We solve the inverse problem of a Föppl–von Kármán plate model by an iterative procedure to obtain the stress distribution within the drums from the experimental data. Our results show that the generally used uniform pre-tension assumption overestimates the pre-stress value, exceeding the averaged stress obtained by more than 47%. Moreover, it is found that the reconstructed stress distributions are bi-axial, which likely originates from the transfer process. The introduced methodology allows one to estimate the tension distribution in drum resonators from their mechanical response and thereby paves the way for linking the used fabrication processes to the resulting device performance.*

This chapter was published as:
Sarafraz, A., Liu, H., Cvetanović, K., Spasenović, M., Vollebregt, S., Manzaneque Garcia, T., Steeneken, P.G., Alijani, F., and Verbiest, G., 2024. Quantifying stress distribution in ultra-large graphene drums through mode shape imaging. *npj 2D Materials and Applications,* 8(1), p.45.

The author’s contribution to this chapter is limited to model development and theoretical studies. Other colleagues carried out the experimental endeavors.

3.1. INTRODUCTION

The exceptional mechanical properties of suspended two-dimensional (2D) materials such as graphene make them ideal materials for applications such as force, mass, and sound sensing [1–4]. Their unique opto- and electromechanical coupling has enabled studies into phase transitions [5], heat transport [6, 7] and even measuring the biological forces of micro-organisms [8]. However, the industrial realization of 2D materials is currently hindered by significant device-to-device variations observed in practice [9]. Addressing this variability is crucial for enhancing the reproducibility and reliability of 2D material based devices. A key factor contributing to this variability is the built-in stress arising from the fabrication process [9–11].

During the transfer of 2D materials onto target substrates, non-uniform stress distributions inevitably occur [12, 13], resulting in surface defects like wrinkles in the fabricated drums [14–16]. Currently, Raman spectroscopy and Atomic Force Microscopy (AFM) are the methods of choice for analyzing the stress distribution in 2D materials [17–19]. Raman spectroscopy monitors the strain-sensitive position of Raman active phonon modes [20]. However, due to its limited spatial and strain resolution, it only provides a relatively coarse strain measurement, making it less suitable for the quantification of the initial stress in suspended 2D materials. AFM is a contact-based technique that is challenging to perform and applies a force to the membrane during measurement. This force potentially affects the morphology and distribution of tension in the membrane. Consequently, development of new non-contact methods that can determine the stress distribution in 2D membranes is highly desirable.

Determining the stress distribution in 2D materials has received limited attention within the literature. Common practice in the field is to assume a uniform stress distribution throughout the membrane [21–25]. This assumption is valid when the aspect ratio (thickness to radius ratio) of 2D material membranes increase, resulting in a bending rigidity dominated mechanical response of the membrane. However, given that the primary advantage of 2D materials is in their high sensitivity for sensing applications, it is common that the aspect ratio is relatively small [26], such that the membrane energy dominates the mechanical response [27, 28], which makes non-uniformities in the stress distribution significant [29]. This deviation can significantly alter the mechanical behavior of the membranes, also leading to inaccuracies estimating mechanical properties [16, 30–33]. However, the modes of vibration of membranes are found to be very sensitive to spatial changes in the membrane[29, 34], thus providing the opportunity to use them for characterizing the non-uniform stress distribution.

In this paper, we propose a methodology to quantify the stress distribution of ultrathin suspended drums by using nanomechanical resonances and their mode shapes. We use Laser Doppler Vibrometry (LDV) [35] to measure graphene drums, with large diameters from 60 μm to 1000 μm, capturing their dynamics with picometer-amplitude resolution. Subsequently, we create an analytical model to calculate resonance frequencies and mode shapes. We then follow a reverse-path by using experimental data to predict both in-plane and out-of-plane displacements, as well as the stress distribution of the 2D drum. Our results highlight that 2D material drums are not uniformly tensioned which challenges the current methodologies for estimating the built-in stress of these drums [19, 20]. The presented methodology allows fabrication techniques to be opti-

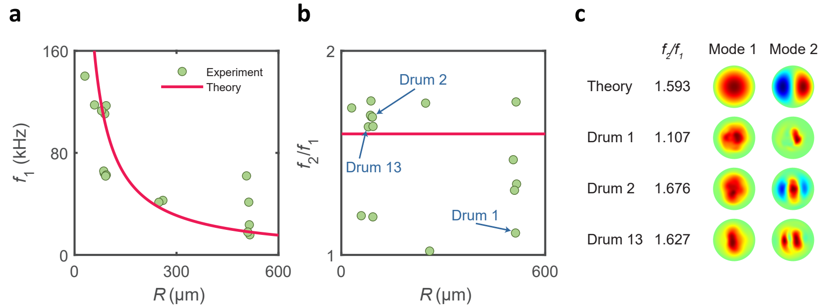

Figure 3.1: Comparison of experimental results with uniform pre-tension. (a) The relationship between the fundamental frequency f_1 and the drum radius R for devices D1−D16 is observed to exhibit an inverse trend. Resonance frequency estimation using equation (3.1) is shown in red, by assuming thickness $h = 15$ nm and pre-tension $n_0 = 0.02$ N/m. (b) The ratio of the second to the first frequency (f_2/f_1) as a function of R for all studied devices. The theoretical value of f_2/f_1 for drums having uniform pre-tension is shown by red line. (c) The first and second mode shapes and the corresponding frequency ratio of three of the measured devices and their comparison to theoretical estimates based on equation (3.1). All mode shapes are normalized with respect to the maximum value of their displacement, and the colorbar ranges between -1 and 1.

mized for improving the uniformity and reproducibility of stress distributions, thus improving yield and performance of sensing applications based on suspended 2D material membranes.

3.2. RESULTS

3.2.1. EXPERIMENTAL SIGNS OF NON-UNIFORM STRESS DISTRIBUTION

We created 16 suspended graphene devices and measured their resonance response (see Methods). To extract their resonances, we employ a fitting procedure based on a linear harmonic oscillator model. The frequency characteristics of the first mode ($f_1 = \frac{\omega_1}{2\pi}$) in devices D1-D16, as a function of the radius R, are depicted in Fig. 3.1(a). The observed dependence on R aligns with the behavior reported earlier on the fundamental frequencies of circular drums [36]. The relationship governing the resonance frequencies is described by the equation

$$f_i = \frac{\gamma_i}{2\pi R}\sqrt{\frac{n_0}{\rho h}}, \tag{3.1}$$

where γ_i represents a constant, n_0 denotes the pre-tension applied to the drum, ρ signifies the mass density, and h stands for the thickness of the drum. Theory gives $\gamma_1 = 2.4048$, with higher resonance frequencies corresponding to increased values of γ_i relative to γ_1. Since R and h are known for our samples from optical microscopy and AFM measurements, we can extract n_0 of the devices using the first resonance frequency f_1 by utilizing Eq. (3.1). We note that the obtained n_0, varies from 2×10^{-3} to 3×10^{-1} N m^{-1}, which is comparable to the range of values reported in the literature [37, 38]. The corresponding strain ε_0 extracted from $n_0 = \sigma_0 h = E h \varepsilon_0/(1-\nu)$ is below 0.0013% for all our devices, which is much lower than the resolution limits of Raman spectroscopy [39].

In Fig. 3.1(b), we plot the ratio between the second and the first resonance frequency of 16 fabricated devices. We also show in Fig. 3.1(b) the f_2/f_1 obtained analytically for circular drums (red line). We note that the experimental values of f_2/f_1 significantly deviate from this red line with a minimum ratio of 1.019 and a maximum ratio of 1.754. To gain insight into these deviations, in Fig. 3.1(c) we show the experimental mode shapes, as determined by the MSA-400 vibrometer, for three of the devices. We note clear differences between the second theoretical mode shape of a circular drum and the experimental mode shape, which emphasizes the substantial influence of non-uniform stress on the dynamics of these drums. In addition, we analyse the ratios f_3/f_1 and f_4/f_1 for a specific subset of our drums (see Appendix 3.A1), in which we also observe a significant difference between the experimental findings and the theoretical predictions based on the assumption of uniform pre-tension.

In addition, it has been theoretically predicted that when a stress distribution is uniform, it results in the emergence of asymmetric mode shapes that are defined by n nodal lines rotated by $2\pi/n$ relative to each other, and possess equal resonance frequencies [27]. Nevertheless, as the level of stress non-uniformity increases, these mode shapes undergo substantial changes resulting in a loss of resemblance between them. Consequently, the non-uniformity in tension distribution has a substantial effect on the mode-shapes, and therefore these mode-shapes contain important information on the stress distribution. In the subsequent section, we introduce a method to deduce the non-uniform tension distribution based on the experimentally acquired mode shapes and resonance frequencies.

3.2.2. THEORY FOR QUANTIFYING STRESS DISTRIBUTION

To analyze the effect of stress distributions on the mode-shapes of the drums, we employ a circular plate model characterized by radius R and thickness h. This model assumes the material to be homogeneous and isotropic, having a density ρ, Young's modulus E, and Poisson's ratio ν. It is worth noting that plate and membrane models have demonstrated accuracy in predicting the mechanical behavior of 2D material membranes [31, 40]. To date, there is no evidence indicating their inapplicability to single- or few-layer 2D materials. Moreover, we assume the structure to be relatively thin, i.e. $h/R \leq 0.1$ [27], such that we can utilize the Föppl–von Kármán plate model. Employing this model enables us to capture the dynamics of drums with a wide range of thickness-to-radius ratio (aspect ratio). The governing equations are expressed in cylindrical coordinates (r, θ, z), with r representing the radial, θ the azimuthal, and z the transverse coordinate. The equations governing transverse and in-plane motions, derived through Hamilton's principle, are given by [41]:

$$\rho h \ddot{w} + D\nabla^4 w - \operatorname{div}(\boldsymbol{N}\boldsymbol{\nabla} w) = 0, \tag{3.2a}$$

$$\rho h \ddot{\boldsymbol{u}} - \mathbf{div}\,\boldsymbol{N} = 0, \tag{3.2b}$$

where

$$\begin{aligned} \boldsymbol{N} &= [Eh/(1-\nu^2)]\,[(1-\nu)\boldsymbol{\epsilon} + \nu \operatorname{tr}(\boldsymbol{\epsilon})\boldsymbol{I}]\,, \\ \boldsymbol{\epsilon} &= \frac{1}{2}\left(\nabla \boldsymbol{u} + \nabla^T \boldsymbol{u} + \nabla w \otimes \nabla w\right). \end{aligned} \tag{3.3}$$

In the equations above, $\boldsymbol{u} = [u; v]$, with u and v denoting the radial and azimuthal displacement fields, while w represents the transverse displacement field. Additionally,

$\nabla^4 w$, ∇w, and $\nabla \boldsymbol{u}$ denote the biharmonic operator applied to the scalar field w, the vector gradient of the scalar field w, and the tensor gradient of the vector field $\boldsymbol{u}$, respectively. $\mathbf{div}\, \boldsymbol{N}$ is vector divergence of the tensor field $\boldsymbol{N}$. Furthermore, $\nabla w \otimes \nabla w$ corresponds to the tensor product between vectors ∇w and ∇w. An overdot indicates differentiation with respect to time, and $D = \frac{Eh^3}{12(1-\nu^2)}$ denotes the bending rigidity. It is noteworthy that, as per the notation presented here, the strain tensor $\boldsymbol{\epsilon}$ and stress resultant tensor $\boldsymbol{N}$ can be identified as second-order tensors in a two-dimensional framework.

In practice, fabricated drums may exhibit deformations that deviate from the conventional assumption of uniform radial deformation, often associated with uniform pretension. Consequently, when these drums undergo transverse dynamic actuation, their displacement fields comprise both static and dynamic components. The static deformation originates from the pre-actuation displacement history, while the dynamic component represents the displacement induced by the actuation process. To gain a comprehensive understanding of the mechanical response in such situations, it becomes essential to incorporate both static and dynamic displacements within the overall displacement field [42–44]. However, the substantial difference in magnitude between in-plane and transverse inertia (proportional to R/h) necessitates the exclusion of dynamic deformation in the in-plane direction. This is due to the fact that based on Newton's second law, higher inertia leads to lower acceleration and dynamical response. Thus, in-plane motion is negligible compared to the out-of-plane dynamics when studying bending vibrations of thin membranes. Therefore, we assume $\boldsymbol{u} = \boldsymbol{u}_s$, but $w = w_s + w_d$, where the subscript s refers to static components and the subscript d represents dynamic deformations.

To capture the vibrational response (w_d) of these drums, we conduct a modal analysis using Eq. (3.2a) centered around the statically deformed configuration (u_s, v_s, w_s). However, since Eq. (3.2a) involves $\boldsymbol{N}$ and is not expressed in terms of displacement fields, we initially reformulate the equation in the context of static and dynamic displacement fields. The detailed derivation procedure for this can be found in Appendix 3.A2. Next , we assume the dynamic transverse deformation w_d to be harmonic and express it as $w_d(r,\theta,t) = w_0^d \varphi(r,\theta)\exp(i\omega t)$, where w_d^0 represents the maximum spatial amplitude of the drum at time $t = 0$, $\varphi(r,\theta)$ denotes the mode shape normalized with respect to maximum displacement, and ω is the corresponding resonance frequency. Next, we make the equations dimensionless (see Appendix 3.A2) and discretize them over a mesh with N nodes in the radial direction and M nodes (M should be odd) in the azimuthal direction (see Appendix 3.A3), which leads to the compact form of the transverse governing equation

$$\mathbf{D_U} U_{i,j} + \mathbf{D_V} V_{i,j} + \sum_k \left(\bar{\mathbf{D}}^k_{\mathbf{W}} W_{i,j}\right) \cdot \left(\bar{\bar{\mathbf{D}}}^k_{\mathbf{W}} W_{i,j}\right) = \left(\bar{\omega}^2 I - \mathbf{D_W}\right) \Phi_{i,j}, \tag{3.4}$$

where $U_{i,j}$, $V_{i,j}$, and $W_{i,j}$ represent the unknown static deformations at spatial node (i,j). Additionally, $\Phi_{i,j}$ is the given (or known) normalized mode shape extracted from the experiments, $\bar{\omega}$ denotes the corresponding non-dimensional resonance frequency, and I is the identity matrix. Moreover, the matrices $\mathbf{D_U}$, $\mathbf{D_V}$, $\mathbf{D_W}$, $\bar{\mathbf{D}}^k_{\mathbf{W}}$, and $\bar{\bar{\mathbf{D}}}^k_{\mathbf{W}}$ denote linear differential operators dependent on the mode shapes and discretization weighting coefficients. Comprehensive details regarding this step can be found in Appendix 3.A3. After a convergence study, we choose $N = 161$ and $M = 91$ to ensure a good balance between computational speed and accuracy of the results. It should be mentioned that this selection may change for drums with different aspect ratios.

Unlike the conventional modal analysis, where predefined static deformations $U_{i,j}$, $V_{i,j}$, and $W_{i,j}$ are used to deduce resonance frequencies $\bar{\omega}$ and mode shapes $\Phi_{i,j}$, in our approach, we follow a reverse-path, and deduce these deformations from measured resonance frequencies and mode shapes. Given the existence of three unknown displacement fields, specifically $U_{i,j}$, $V_{i,j}$, and $W_{i,j}$ ($3 \times M \times N$ unknowns), the extraction of these displacement fields necessitates a minimum of $3 \times M \times N$ equations. This underscores the significance of having no fewer than three sets of mode shapes ($\Phi^1_{i,j}, \Phi^2_{i,j}, \Phi^3_{i,j}$), along with their corresponding non-dimensional frequencies ($\bar{\omega}_1, \bar{\omega}_2, \bar{\omega}_3$) for estimating the built-in stress, which collectively provide $3 \times M \times N$ equations across the mesh (see Eq. (3.A32)). However, in practice, an additional mode shape becomes a crucial requirement. The underlying rationale for this is rooted in the observation that equations linked to boundary nodes yield a trivial $0 = 0$ relationship. Consequently, introducing supplementary equations is necessary to fulfill the requisite rank of the algebraic equation system. In pursuit of accurately determining stress distributions from experimental mode shapes and frequencies, it thus becomes essential to consider at least four mode shapes alongside their corresponding resonance frequencies.

To validate our numerical methodology and equations, we performed finite element simulations on a flat circular plate characterized by a predefined non-uniform stress distribution. The computed mode shapes and resonance frequencies were then employed to reconstruct the stress distribution using the methodology we have introduced (for detailed discussion, see Appendix 3.A4).

By simultaneously using the governing Eq. (3.A32) for a minimum of four mode shapes and the respective resonance frequencies, it becomes possible to determine the static displacement fields and the associated stress distribution fields. The flowchart presented in Fig. 3.A5 explains the sequential approach for obtaining stress distributions from experimental mode shapes and frequencies. The technique commences by fitting a surface to the experimental mode shapes. This is important as Eq. (3.A32) involves derivative operators and any non-smoothness and noise in experimental mode shapes leads to numerical inaccuracies [30]. In order to guarantee the compliance of boundary conditions, we utilize the mode shapes of a uniformly-tensioned plate as the basis for our fitting function (see Appendix 3.A5).

Subsequently, utilizing the smoothed mode shapes, we aim to extract the static displacement fields. However, due to the nonlinearity of Eq. (3.A32) with respect to $W_{i,j}$, extracting the solution without a suitable initial approximation poses a challenge. As a possible solution, we assume a parabolic form for the static transverse displacement, characterized by an undetermined deflection amplitude at the center of the drum ($W_{i,j} = W_0(1 - \bar{R}^2_{i,j})$), where W_0 signifies the deflection at the center, and $\bar{R}_{i,j}$ represents the $\bar{r}$-coordinate of node (i, j). By solving Eq. (3.A32) using the experimentally acquired mode shapes $\Phi^1_{i,j}$, $\Phi^2_{i,j}$, $\Phi^3_{i,j}$, and $\Phi^4_{i,j}$, we can determine the unknowns $U_{i,j}$, $V_{i,j}$, and W_0. It is crucial to recognize that due to the influence of noise and measurement inaccuracies, achieving 100% accuracy in solving for displacements is unattainable. Therefore, employing a least-squares method becomes necessary. This method enhances accuracy by incorporating more equations, namely additional mode shapes and frequencies, into

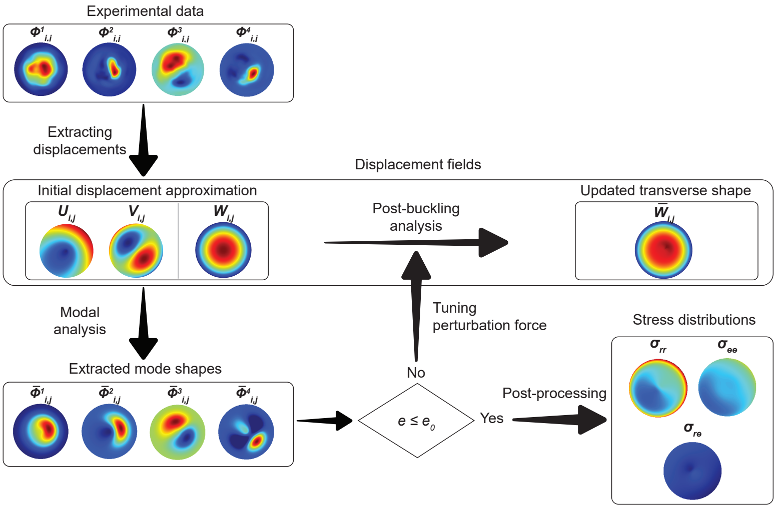

Figure 3.2: The flowchart for deriving stress distributions from experimental mode shapes and resonance frequencies. Assuming a parabolic deformation in the transverse direction, the experimental mode shapes are first employed to extract initial displacement fields. Then a modal analysis is performed. If the extracted mode shapes do not match the experimental ones sufficiently ($e > e_0$), the perturbation force is tuned and using a post-buckling analysis, the transverse shape is modified. After that, using in-plane displacement fields and the updated transverse displacement, we again obtain theoretical mode shapes and resonance frequencies. If the mode shapes do not satisfy the criterion (3.A37), we recalculate the transverse shape by adjusting the perturbation force to the post-buckling step. From there we return to the modal analysis. When the convergence criterion is met, the obtained displacement fields are used to calculate stress distributions. Here, $i = 1, 2, \ldots, N$, and $j = 1, 2, \ldots, M$ denotes the node number in radial, and azimuthal directions.

the solution process.

It is imperative to acknowledge that assuming an axisymmetric parabolic deflection for the transverse displacement has inherent limitations. The presence of non-uniform displacements in the studied membranes might lead to static deformation and the creation of a buckling pattern, owing to their ultra-thin nature. Due to experimental and numerical inaccuracies, the displacement fields that are obtained from solving Eq. (3.A32) don't always meet the requirements of the in-plane Eq. (3.2b). Therefore, it is crucial to identify a stable out-of-plane configuration that fulfills Eq. (3.2). In response to potential static transverse asymmetries and to rectify our initial assumption of parabolic static deformation, we perform a post-buckling analysis. This analysis utilizes the in-plane displacement fields $U_{i,j}$, $V_{i,j}$, and $W_{i,j}$, which are obtained from the experimental mode shapes to update transverse displacement $W_{i,j}$ to $\bar{W}_{i,j}$. In the context of this post-buckling analysis, a minor perturbing uniform transverse force is introduced, which serves to update the drum's transverse shape and accounts for its nonlinear behavior [45].

In order to perform the post-buckling analysis, it is recommended to utilize equations (3.2) or alternatively, incorporate the in-plane displacement fields ($U_{i,j}$ and $V_{i,j}$) into a finite element method (FEM) software that is capable of handling nonlinear structural analysis. This will enable an analysis of the post-buckling response of the drum and the establishment of its modified transverse shape $\bar{W}_{i,j}$. It is crucial to highlight that as a result of the non-uniform characteristics of $U_{i,j}$ and $V_{i,j}$, the post-buckling analysis results in an asymmetric transverse shape $\bar{W}_{i,j}$ that deviates from the axisymmetric shape $W_{i,j}$.

Since, the experimental displacement field is not known for the drums and in order to ensure accurate computation of both in-plane and transverse displacement fields, we conduct modal analysis to extract mode shapes and resonance frequencies from the static displacements ($U_{i,j}$, $V_{i,j}$, and $\bar{W}_{i,j}$). It should be noted that Eq. 4 shows a one-to-one mapping between mode shapes and displacement fields, thus the comparison between the mode shapes can directly reflect the comparison between the static displacement fields. In order to quantitatively assess the fidelity of the reconstructed mode shapes compared to their experimental counterparts, we employ an error metric denoted by e. This metric e characterizes the average spatial deviation between the reconstructed and experimental mode shapes and is defined as follows

$$e = \frac{1}{\bar{N}} \sum_{n=1}^{\bar{N}} \left[\frac{\int_0^{2\pi} \int_0^1 \left(\bar{\varphi}_n - \varphi_n\right)^2 r \mathrm{d}r \mathrm{d}\theta}{\int_0^{2\pi} \int_0^1 \left(\varphi_n\right)^2 r \mathrm{d}r \mathrm{d}\theta} \right]^{1/2} \leq e_0, \tag{3.5}$$

where e_0 serves as an error threshold. In this equation, $\bar{\varphi}_n$ is the n-th normalized mode shape obtained from modal analysis, φ_n signifies the n-th normalized experimental mode shape, and $\bar{N}$ represents the total number of mode shapes used in the fitting procedure. It's important to note that both $\bar{\varphi}_n$ and φ_n are the continuous forms of $\Phi^n_{i,j}$ and $\bar{\Phi}^n_{i,j}$, respectively.

If the criterion (3.A37) is satisfied ($e \leq e_0$), the solution is considered to be converged. Conversely, if $e > e_0$, the post-buckled configuration is re-calculated with a new perturbation in the transverse direction, leading to the acquisition of an updated transverse mode shape. This iterative process continues until the convergence criterion is met.

To determine an appropriate value for e_0, we initiate the iterative process without applying any perturbation force and gradually increase it step-by-step. The observed trend reveals an initial decrease in the error metric e as the perturbation force rises until it reaches the minimum value e_0 at a perturbation force of δp_m. Beyond this point, further increments in the perturbation force result in an increase in the error. Consequently, the minimum achievable error for each set of experiments corresponds to e_0, which varies among different drums. For instance, device D1 exhibits an error threshold of $e_0 \simeq 0.19$. A more detailed and comprehensive discussion regarding the determination of e_0 can be found in Appendix 3.A6.

Once the solution has converged, the numerical displacement field effectively approximates the experimental displacement field, which enables us to compute the strain field and subsequently derive the stresses within the drum's mid-plane using Supplementary Eqs. (3.A2) and (3.A3). For a more comprehensive overview of the described procedure, including a detailed flowchart, please consult the Appendix 3.A5.

3.2.3. FITTING PROCEDURE

As elaborated in the previous section, the numerical procedure necessitates an initial assumption of a parabolic transverse displacement field. However, this assumption does

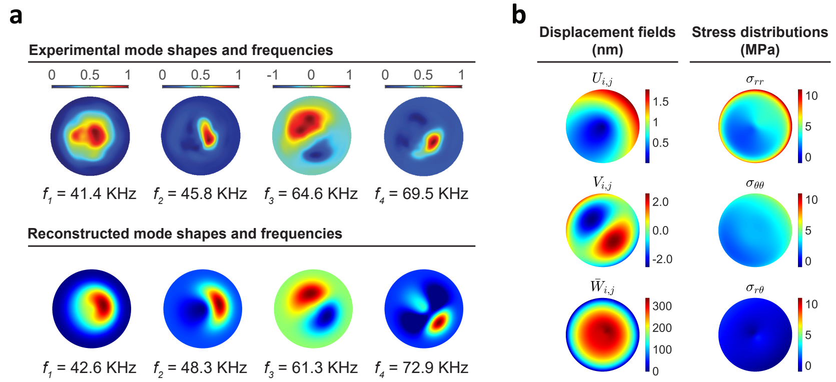

Figure 3.3: (a) Reconstruction of stress distributions based on experimental mode shapes for device D1. As described in the main text, the experimental mode shape and frequencies are utilised to derive displacement fields and stress distributions. For the purpose of determining the validity of the results, the theoretical mode shapes are reconstructed using the displacement field. (b) Displacement fileds and Stress distributions predicted by current method. As can be seen assumption of uniform stress distribution is not valid for the manufactured device.

not universally apply to all manufactured devices. Some of the manufactured devices exhibit significant complex wrinkling patterns that deviate noticeably from the parabolic approximation. Consequently, the proposed method is not applicable to drums that deviate from this assumption.

Among the devices produced for this study, four of them (D1, D2, D6, and D13) exhibited minimal or negligible wrinkling patterns, making them well-suited candidates for the proposed solution outlined in this study. For these four drums, we quantified stress distributions and validated their accuracy by reconstructing mode shapes using the derived stresses. In Fig. 3.3, we provide an illustrative example showcasing both the experimental mode shapes and the reconstructed mode shapes for device D1, utilizing the first four distinct mode shapes. It is evident that the obtained stress distribution was able to accurately reconstruct the experimental mode shapes with a high level of accuracy. The results for devices D2, D6, and D13 are presented in Appendix 3.A7.

Moreover, to highlight the fidelity of the proposed method, we present the extracted displacement field and the corresponding non-uniform stress distributions in Fig. 3.3. Note that Raman spectroscopy, which we utilized for stress measurement, is limited in its ability to detect the non-uniformity of stress within the drum (see Appendix 3.A8). The predicted stress distribution obtained through Raman spectroscopy appears to be nearly constant and uniform, with large uncertainty across the drum surface. This is due to the fact that the strain values ($\varepsilon < 0.0013\%$) are lower than the resolution limit (0.1%) of Raman spectroscopy [20, 39, 46] (See Methods). In the Appendix 3.A8, a thorough discussion of the Raman spectroscopy measurements and the obtained stress distributions for device D1 is provided. In contrast, the presented methodology is founded upon continuum mechanics which is not dimension-dependent. As a result, the resolution of this method is primarily constrained by the measurement device's capability to discern mode shapes. Consequently, the method's efficacy remains unaffected by the size of the drum or the scale of its strain distributions. This implies that even for small drums with radii on the order of a few micrometers, our methodology can measure strain and stress distributions, regardless of the magnitude of the strains. Hence, this approach remains applicable across a range of scales, encompassing relatively small drums.

To compare the extracted stress distributions and the nominal stress values obtained assuming a uniform tension distribution, we calculated the spatial averages of normal and shear stresses by

$$\tilde{\sigma}_{ij} = \frac{\int_0^{2\pi}\int_0^R \sigma_{ij} r \mathrm{d}r \mathrm{d}\theta}{\pi R^2}, \tag{3.6}$$

where $i, j = \{r, \theta\}$. To measure the robustness of our findings, we systematically adjusted the level of mode shape fitting during the preliminary stage (see Eq. (3.A3)). This variation allowed us to quantitatively determine the associated standard deviation and obtain valuable insights into the sensitivity of our stress distribution analysis. To determine the nominal stress σ_0 under the assumption of a uniform tension distribution, we employed the first resonance frequencies, considering them as resonances of an ideal theoretical drum subjected to uniform tension (see Eq. (3.1)). Notably, the spatial average of shear stress for all four drums was found to be negligible. However, this was not the case for the values of $\tilde{\sigma}_{rr}$ and $\tilde{\sigma}_{\theta\theta}$, which demonstrated appreciable differences. The computed average stress values, obtained through our analysis and assuming uniform stress distribution, are both presented in Table (3.1).

The differences observed between the average values of $\tilde{\sigma}_{rr}$ and $\tilde{\sigma}_{\theta\theta}$ in Table (3.1) contradict the uniform stress assumption, which posits that $\tilde{\sigma}_{rr} = \tilde{\sigma}_{\theta\theta} = \sigma_0$. Notably, a greater deviation of $\tilde{\sigma}_{rr}$ from $\tilde{\sigma}_{\theta\theta}$ indicates a higher degree of non-uniformity in the stress distribution within the drum. The observed differences between the average values of $\tilde{\sigma}_{rr}$ and $\tilde{\sigma}_{\theta\theta}$ raise doubts about the validity of the uniform stress assumption. Specifically, σ_0 is at least 47% greater than the mean value of $\tilde{\sigma}_{rr}$ for each of the drums. This finding suggests that spatially averaging the stress distributions will not yield a uniform stress representation of the overall behavior of the studied drums. Therefore, accounting for the non-uniformities is essential for proper estimation of the built-in stress in ultra-thin membranes.

Our method's effectiveness is further evident in Fig. 3.3, where we observe the influence of a free edge on the displacement and stresses of the drum. The microscope image of device D1, as depicted in Fig. 3.4(d), clearly demonstrates that one side of the drum is clamped, while the other side remains unclamped and capable of free movement. Surprisingly, this free edge has influenced the results by exhibiting less radial displacement

Table 3.1: Spatial average value of non-uniform stress distribution in comparison with nominal stress value assuming uniform stress distribution in the drums.

Device	$\tilde{\sigma}_{rr}$ (MPa)	$\tilde{\sigma}_{\theta\theta}$ (MPa)	σ_0 (MPa)
D1	3.76 ± 0.25	2.80 ± 0.29	7.05
D2	0.65 ± 0.06	0.53 ± 0.08	1.36
D6	0.54 ± 0.09	0.33 ± 0.07	0.94
D13	1.03 ± 0.21	0.49 ± 0.10	1.52

and consequently lower stresses on the free side. This finding supports the intuition that a free edge allows the drum to mechanically release stresses near the edge.

3.3. DISCUSSION

The proposed methodology addresses a system of nonlinear equations (Eq. (3.A32)), under the assumption of a parabolic transverse static displacement field. However, when the drum exhibits initial corrugations or wrinkles that cannot be adequately characterized by such a parabolic displacement field, the system of equations becomes challenging to solve. In such scenarios, the equations need to be solved by providing a suitable initial guess for the transverse displacement field $W_{i,j}$. To estimate the static transverse displacement field of the drum in the presence of these non-parabolic deformations, corrugations should be experimentally probed. Several techniques are available for measuring these out-of-plane deformations [47, 48], and can aid with quantifying the tension distribution.

Notably, microscopic images of the drums (see Fig. 3.A13) do not always reveal signs of transverse bulge or wrinkles, despite their presence. Although the transverse displacement is relatively small compared to the drum's radius ($W_0/R \leq 0.001$), neglecting it in the modal analysis can lead to inaccurate mode shape estimations and ultimately even to failure in reconstructing the experimental mode shapes. Moreover, even minor static transverse asymmetries can affect the expected mode shapes [45, 49], emphasizing the need for an accurate solution capturing these deviations. This emphasizes the importance of the transverse displacement field when reconstructing the stress distribution.

Owing to inherent experimental uncertainties and noise, there exists a lower bound on the threshold e_0. For device D1, the estimated experimental noise on each mode shape is 3%, 4%, 18%, and 20%, respectively, leading to a lower average bound for e_0 of 11%. To enhance the precision of measuring e_0, employing measurement devices with higher spatial resolution and lower noise levels is recommended.

The comprehensive study of drums yielded valuable insights into their stress distributions. These drums experience uniaxial or biaxial loading with different loadings along the two axes, suggesting non-uniform biaxial tension induced in the manufacturing process. This understanding is crucial for optimizing manufacturing processes to achieve uniform stress distribution and flatness in the drums.

The proposed method is specifically tailored for thin drums, taking into account both stretching and bending energies to derive the governing equations and ensure numerical stability. As a result, two distinct mechanisms govern the mode shapes and resonance frequencies. In cases where stretching dominates the deformation of the drum, the pre-stresses play a significant role in influencing its vibrational behavior. This scenario is particularly relevant for drums with a height-to-radius ratio $h/R \leq 0.001$. Conversely, as bending deformation becomes more prevalent over stretching, the vibrational behavior of the drum is primarily governed by bending energies, with pre-stresses having a marginal role. In such instances, the accuracy of the proposed method may be compromised, as the mode shapes are predominantly influenced by bending effects rather than stress distributions. However, it is important to mention that when the aspect ratio is large, the mechanics of the drums are mostly influenced by the bending mechanism, while the effect of stress distribution becomes insignificant. Nevertheless, the maximum ratio of thickness to radius (h/R) observed in the drums manufactured in our study is roughly 0.00023 (see Table 3.1), which confirms that the drums analyzed in our work are membranes with negligible bending rigidity. Therefore, the established model proves suitable for addressing the problem.

Despite this limitation, in practical applications, the first scenario ($h/R \leq 0.001$) is often encountered, rendering the proposed method suitable and reliable for analyzing the vibrational behavior of drums. It is worth noting that as h/R increases, the bending deformations become more energy costly, resulting in drums with fewer corrugations and wrinkles. Unfortunately, this also leads to reduced sensitivity to transverse loadings and masses. Hence, the choice of h/R becomes critical in designing circular drums to achieve the desired vibrational characteristics and performance for specific applications.

It is important to assure that the method proposed is applicable to thinner devices or membranes of smaller dimensions. Here, we should highlight that our approach is based on continuum mechanics and thus size-independent. Yet, to affirm the applicability of our method to thinner and smaller graphene membranes, we utilized the experimental data of [34] for a graphene drum ($h = 10\,\text{nm}$, $d = 5\,\mu\text{m}$), and reconstructed the non-uniform tension successfully (see Appendix 3.A9).

It is also noteworthy that the methodology proposed herein is not limited solely to graphene membranes but is applicable to a broader range of thin films and 2D material membranes. In our analysis, we adopted a linear isotropic material model to predict material behavior. However, if other 2D material membranes exhibit discrepancies in material behavior, such as anisotropy [50], these can be incorporated into the proposed method through constitutive law (Eq. 3.A3). This allows for the extension of the formulation to accommodate studying of various types of 2D material membranes.

In conclusion, we presented a methodology for quantitative determination of the tension distribution in ultra-thin 2D material drums based on experimental mode shapes and resonance frequencies. By utilizing a circular plate model, we derived governing equations that capture the static and dynamic deformation of the drums. The proposed approach successfully accounts for both stretching and bending energies, providing an effective solution for analyzing the vibrational behavior of circular drums.

The validation of the method through finite element simulations on known stress distributions demonstrates its accuracy and reliability. We applied the methodology to four fabricated drums and gained valuable insights into their stress distributions. The findings revealed the presence of non-uniform biaxial tension induced during the manufacturing process. Understanding these stress distributions is critical for optimizing the fabrication processes to achieve uniform stress distribution and flatness in the drums.

Additionally, we discussed the limitations related to the assumption of a parabolic transverse static displacement field and the need for an appropriate initial guess for the transverse displacement field in cases where initial corrugations or wrinkles are present. The insights gained from this study can aid in achieving better performance and reliability in 2D drum fabrication and contribute to accurate and robust mechanical characterization of ultra-thin materials.

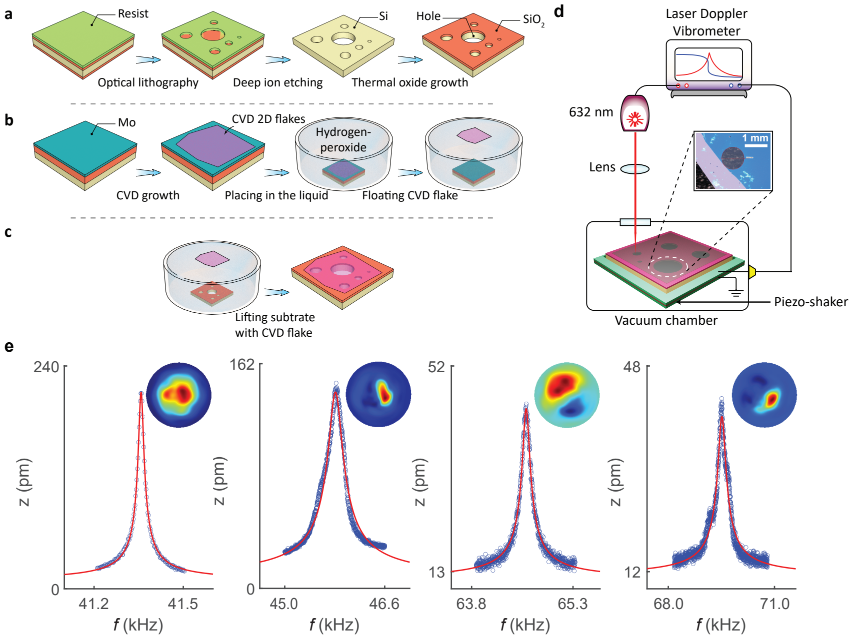

Figure 3.4: Fabrication and vibration measurement of graphene drums. (a) Fabrication process of SiO_2/Si substrate with etched holes. (b) Growth and exfoliation of large-scale CVD graphene flake. (c) Wet transfer method to suspend CVD graphene on substrate. (d) Schematic of measurement setup comprising a MSA400 Polytec Laser Doppler Vibrometer (LDV) for detection and read-out. The sample is placed in the vacuum chamber and driven by a piezo shaker. The inset: optical image of device D1; purple region, Si/SiO_2 substrate; blue region, supported graphene; transparent region, suspended graphene. (e) The first four resonances of device D1; the damped linear harmonic oscillator fit is shown by red line.

3.4. METHODS

3.4.1. FABRICATION METHOD

The fabrication procedure of the devices is illustrated in Figs. 3.4(a)-(c). As Fig. 3.4(a) shows, we first prepare a Si (100) target substrate containing through holes made using deep reactive ion etching with diameters ranging from 60 μm to 1000 μm. Next, we deposit multi-layer graphene using chemical vapor deposition (CVD) on a thin-film Mo catalyst, as shown in Fig. 3.4(b). The final stage of the fabrication procedure is the transfer of CVD-grown graphene from the growth substrate to the target substrate using a wet transfer process, as depicted in Fig. 3.4(c).

The fabrication process resulted in the production of a set of 16 unique devices, denoted as D1 to D16, which were spread among different chips. For a comprehensive description of the fabrication method, please refer to Appendix 3.A10. The drums had a range of radii (R) from 61 to 1032 μm. We measured the thickness (h) of the CVD graphene on all chips using an atomic force microscopy (AFM) and found that h ranges from 7 to 13.8 nm (see Appendix 3.A11).

3.4.2. MEASUREMENT METHODOLOGY

To probe nanomechanical vibrations of the devices, we use a piezo shaker to drive the drums into resonance and a Polytec MSA400 Laser Doppler Vibrometry (LDV) system to measure their velocity in the out-of-plane direction (see Fig. 3.4(d)). The LDV actuates the piezo shaker at a specific frequency f while simultaneously recording the position-dependent displacement z_f of the device using a 632 nm He-Ne laser with a spot diameter of ~5 µm. All measurements are conducted at room temperature inside a vacuum chamber at 10^{-4} mbar. It should be noted that even though measurements are performed at room temperature, local heating from the laser can alter membrane properties and stress field, especially in the nonlinear regime. To circumvent this problem we performed our measurements at very low laser powers and ensured that the motion is probed in the linear regime of operation (see Refs. [51, 52]). Fig. 3.4(e) displays the measured first four resonances of device D1.

APPENDIX

3.A1. MEASURED FREQUENCY RATIOS OF EXPERIMENTALLY MEASURED GRAPHENE DRUMS

Here, we evaluate the ratios of f_3/f_1 and f_4/f_1 within a particular group of drums. The results of our investigation demonstrate a notable disparity between the experimental observations and the theoretical predictions made under the assumption of uniform pre-tension. Fig. 3.A1 shows this analysis for 7 different drums.

3.A2. GOVERNING EQUATIONS

As previously mentioned in the main text, the circular plate model employed in this study is defined by its radius, denoted as R, and its thickness, denoted as h. The underlying assumption of the model is that the drum is composed of a uniformly distributed and consistent material with density (ρ), Young's modulus (E), and Poisson's ratio (ν). The governing equations are derived by employing cylindrical coordinates (r, θ, z), where r denotes the radial coordinate, θ represents the azimuthal coordinate (θ direction), and z corresponds to the transverse coordinate. The displacement field of the drums can be mathematically represented as functions of time t by the utilisation of the following equations [27]

$$\begin{aligned}
u_r(r,\theta,z,t) &= u(r,\theta,t) - z\frac{\partial w}{\partial r},\\
u_\theta(r,\theta,z,t) &= v(r,\theta,t) - z\left(\frac{1}{r}\frac{\partial w}{\partial \theta}\right),\\
u_z(r,\theta,z,t) &= w(r,\theta,t),
\end{aligned}\tag{3.A1}$$

where (u, v, w) represent the radial, tangential, and transverse displacements, respectively. Taking von Kármán nonlinearities into account, the nonlinear normal and shear strains are determined as

$$\begin{aligned}
\varepsilon_{rr} &= \frac{\partial u}{\partial r} + \frac{1}{2}\left(\frac{\partial w}{\partial r}\right)^2 - z\frac{\partial^2 w}{\partial r^2},\\
\varepsilon_{\theta\theta} &= \frac{u}{r} + \frac{1}{r}\frac{\partial v}{\partial \theta} + \frac{1}{2}\left(\frac{1}{r}\frac{\partial w}{\partial \theta}\right)^2 - \frac{z}{r}\left(\frac{\partial w}{\partial r} + \frac{1}{r}\frac{\partial^2 w}{\partial \theta^2}\right),\\
\varepsilon_{r\theta} &= \frac{1}{2}\left(\frac{1}{r}\frac{\partial u}{\partial \theta} + \frac{\partial v}{\partial r} - \frac{v}{r} + \frac{1}{r}\frac{\partial w}{\partial r}\frac{\partial w}{\partial \theta}\right) - \frac{z}{r}\left(\frac{\partial^2 w}{\partial r\partial \theta} - \frac{1}{r}\frac{\partial w}{\partial \theta}\right).
\end{aligned}\tag{3.A2}$$

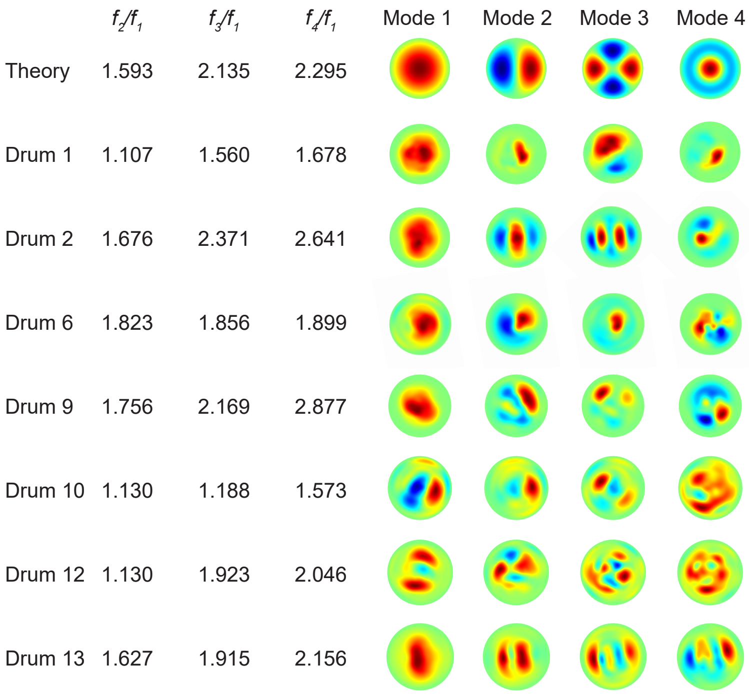

	f_2/f_1	f_3/f_1	f_4/f_1	Mode 1	Mode 2	Mode 3	Mode 4
Theory	1.593	2.135	2.295				
Drum 1	1.107	1.560	1.678				
Drum 2	1.676	2.371	2.641				
Drum 6	1.823	1.856	1.899				
Drum 9	1.756	2.169	2.877				
Drum 10	1.130	1.188	1.573				
Drum 12	1.130	1.923	2.046				
Drum 13	1.627	1.915	2.156				

Figure 3.A1: The first, second, third, and fourth mode shapes and the corresponding frequency ratio of seven of the measured devices and their comparison to theoretical estimates based on Eq. (1) of the main text. All mode shapes are normalized with respect to the maximum value of their displacement, and the colorbar ranges between -1 and 1.

Through constitutive equation and Lamé constants ($\mu = E/(2(1+\nu))$; $\lambda = E\nu/\left(1-\nu^2\right)$), the stresses are related to the strain fields as

$$\sigma_{ij} = 2\mu\varepsilon_{ij} + \lambda\delta_{ij}\varepsilon_{kk}, \tag{3.A3}$$

where σ_{ij} are the stresses, δ_{ij} denotes Kronecker delta, and $i, j = \{r, \theta\}$.

The strain energy of the circular plate can be obtained as

$$U = \int_0^{2\pi}\int_0^{R}\int_{-\frac{h}{2}}^{+\frac{h}{2}} \sigma_{ij}\varepsilon_{ij}\,\mathrm{d}z\,\mathrm{d}r\,\mathrm{d}\theta, \tag{3.A4}$$

and its kinetic energy neglecting radial (i.e. in-plane) inertia , is given by

$$T = \frac{1}{2}\int_{-\frac{h}{2}}^{+\frac{h}{2}}\int_0^{2\pi}\int_0^{R} \rho\dot{w}^2 r\,\mathrm{d}r\,\mathrm{d}\theta\,\mathrm{d}z, \tag{3.A5}$$

where the overdot indicates differentiation with respect to time t.

Next, by using the Hamilton's principle

$$\delta\int_0^{T}(T-U)\,\mathrm{d}t = 0, \tag{3.A6}$$

in which δ is the variational operator, the governing equations of motion can be found as follows [27]

$$\delta u : -\frac{1}{r}\left[\frac{\partial}{\partial r}(rN_{rr}) + \frac{\partial N_{r\theta}}{\partial \theta} - N_{\theta\theta}\right] + I_0\frac{\partial^2 u}{\partial t^2} = 0, \tag{3.A7a}$$

$$\delta v : -\frac{1}{r}\left[\frac{\partial}{\partial r}(rN_{r\theta}) + \frac{\partial N_{\theta\theta}}{\partial \theta} + N_{r\theta}\right] + I_0\frac{\partial^2 v}{\partial t^2} = 0, \tag{3.A7b}$$

$$\begin{aligned} \delta w : &-\frac{1}{r}\left[\frac{\partial^2}{\partial r^2}(rM_{rr}) - \frac{\partial M_{\theta\theta}}{\partial r} + \frac{1}{r}\frac{\partial^2 M_{\theta\theta}}{\partial \theta^2} + \frac{2}{r}\frac{\partial}{\partial r}\left(r\frac{\partial M_{r\theta}}{\partial \theta}\right)\right] \\ &+ \frac{\partial}{\partial r}\left(rN_{rr}\frac{\partial w}{\partial r} + N_{r\theta}\frac{\partial w}{\partial \theta}\right) + \frac{1}{r}\frac{\partial}{\partial \theta}\left(N_{\theta\theta}\frac{\partial w}{\partial \theta} + rN_{r\theta}\frac{\partial w}{\partial r}\right) + I_0\ddot{w} = 0, \end{aligned} \tag{3.A7c}$$

where δu, δv and δw are the virtual displacements. Furthermore, $I_0 = \rho h$, the resultant forces $N_{ij} = (N_{rr}, N_{\theta\theta}, N_{r\theta})$, and the resultant moments $M_{ij} = (M_{rr}, M_{\theta\theta}, M_{r\theta})$ are defined by

$$\begin{aligned} N_{ij} &= \int_{-\frac{h}{2}}^{+\frac{h}{2}} \sigma_{ij}\mathrm{d}z, \\ M_{ij} &= \int_{-\frac{h}{2}}^{+\frac{h}{2}} \sigma_{ij}z\mathrm{d}z. \end{aligned} \tag{3.A8}$$

Eq. (3.A7c), which describes the transverse governing equation, can be reformulated in terms of the displacement fields u, v, and w by utilizing Eq.s (3.A2), (3.A3), and (3.A8) as

$$\begin{aligned} &\frac{Eh^3}{12(1-\nu^2)}\left[\left(\frac{\partial^4 w}{\partial r^4}\right) + \left(\frac{2}{r}\frac{\partial^3 w}{\partial r^3}\right) - \left(\frac{1}{r^2}\frac{\partial^2 w}{\partial r^2}\right) + \left(\frac{1}{r^3}\frac{\partial w}{\partial r}\right)\right. \\ &\left. + \left(\frac{1}{r^4}\frac{\partial^4 w}{\partial \theta^4}\right) + \left(\frac{4}{r^4}\frac{\partial^2 w}{\partial \theta^2}\right) - \left(\frac{2}{r^3}\frac{\partial^3 w}{\partial r\partial \theta^2}\right) + \left(\frac{2}{r^2}\frac{\partial^4 w}{\partial r^2\partial \theta^2}\right)\right] \\ &- \frac{Eh}{1-\nu^2}\left[\left(\frac{1}{r^3}u\frac{\partial^2 w}{\partial \theta^2}\right) + \nu\left(\frac{1}{r^2}\frac{\partial u}{\partial r}\frac{\partial^2 w}{\partial \theta^2}\right) + \frac{1-\nu}{2}\left(\frac{1}{r^2}\frac{\partial^2 u}{\partial \theta^2}\frac{\partial w}{\partial r}\right)\right. \\ &+ (1+\nu)\left(\frac{1}{r}\frac{\partial u}{\partial r}\frac{\partial w}{\partial r}\right) + \frac{1+\nu}{2}\left(\frac{1}{r^2}\frac{\partial^2 u}{\partial r\partial \theta}\frac{\partial w}{\partial \theta}\right) + \frac{1+\nu}{2}\left(\frac{1}{r^3}\frac{\partial u}{\partial \theta}\frac{\partial w}{\partial \theta}\right) \\ &\left. + (1-\nu)\left(\frac{1}{r^2}\frac{\partial u}{\partial \theta}\frac{\partial^2 w}{\partial r\partial \theta}\right) + \left(\frac{\partial^2 u}{\partial r^2}\frac{\partial w}{\partial r}\right) + \nu\left(\frac{u}{r}\frac{\partial^2 w}{\partial r^2}\right) + \left(\frac{\partial u}{\partial r}\frac{\partial^2 w}{\partial r^2}\right)\right] \\ &- \frac{Eh}{1-\nu^2}\left[\left(\frac{1}{r^3}\frac{\partial^2 v}{\partial \theta^2}\frac{\partial w}{\partial \theta}\right) + \left(\frac{1}{r^3}\frac{\partial v}{\partial \theta}\frac{\partial^2 w}{\partial \theta^2}\right) - \frac{1-\nu}{2}\left(\frac{1}{r^2}\frac{\partial v}{\partial r}\frac{\partial w}{\partial \theta}\right)\right. \\ &- \frac{1-\nu}{2}\left(\frac{1}{r^2}\frac{\partial v}{\partial \theta}\frac{\partial w}{\partial r}\right) + \frac{1+\nu}{2}\left(\frac{1}{r}\frac{\partial^2 v}{\partial r\partial \theta}\frac{\partial w}{\partial r}\right) + (1-\nu)\left(\frac{1}{r}\frac{\partial v}{\partial r}\frac{\partial^2 w}{\partial r\partial \theta}\right) \\ &\left. + \frac{1-\nu}{2}\left(\frac{v}{r^3}\frac{\partial w}{\partial \theta}\right) - (1-\nu)\left(\frac{v}{r^2}\frac{\partial^2 w}{\partial r\partial \theta}\right) - \frac{1-\nu}{2}\left(\frac{1}{r}\frac{\partial^2 v}{\partial r^2}\frac{\partial w}{\partial \theta}\right) + \frac{\nu}{r}\left(\frac{\partial v}{\partial \theta}\frac{\partial^2 w}{\partial r^2}\right)\right] \\ &- \frac{Eh}{1-\nu^2}\left[\frac{3}{2}\left(\frac{1}{r^4}\frac{\partial^2 w}{\partial \theta^2}\left(\frac{\partial w}{\partial \theta}\right)^2\right) - \frac{1}{2}\left(\frac{1}{r^3}\frac{\partial w}{\partial r}\left(\frac{\partial w}{\partial \theta}\right)^2\right) + \frac{1}{2}\left(\frac{1}{r^2}\frac{\partial^2 w}{\partial \theta^2}\left(\frac{\partial w}{\partial r}\right)^2\right)\right. \\ &+ 2\left(\frac{1}{r^2}\frac{\partial w}{\partial \theta}\frac{\partial w}{\partial r}\frac{\partial^2 w}{\partial r\partial \theta}\right) + \frac{1}{2}\left(\frac{1}{r^2}\frac{\partial^2 w}{\partial r^2}\left(\frac{\partial w}{\partial \theta}\right)^2\right) \\ &\left. + \frac{3}{2}\left(\frac{\partial^2 w}{\partial r^2}\left(\frac{\partial w}{\partial r}\right)^2\right) + \frac{1}{2}\left(\frac{1}{r}\left(\frac{\partial w}{\partial r}\right)^3\right)\right] + I_0\ddot{w} = 0 \end{aligned} \tag{3.A9}$$

To characterize the mechanical response of a pre-deformed vibrating drum, we decompose the displacement field into a static and a dynamic part as follows [42, 43],

$$\begin{aligned} u(r,\theta,t) &= u_s(r,\theta) \\ v(r,\theta,t) &= v_s(r,\theta) \\ w(r,\theta,t) &= w_s(r,\theta) + w_d(r,\theta,t). \end{aligned} \tag{3.A10}$$

Here, the subscript s refers to static components, while d represents dynamic deformations. Inserting Eq. (3.A10) in Eq. (3.A9) we find the governing static and dynamic equations. The static equation is obtained as

$$\begin{aligned}
&\frac{Eh^3}{12(1-\nu^2)}\left[\left(\frac{\partial^4 w_s}{\partial r^4}\right)+\left(\frac{2}{r}\frac{\partial^3 w_s}{\partial r^3}\right)-\left(\frac{1}{r^2}\frac{\partial^2 w_s}{\partial r^2}\right)+\left(\frac{1}{r^3}\frac{\partial w_s}{\partial r}\right)\right.\\
&\left.+\left(\frac{1}{r^4}\frac{\partial^4 w_s}{\partial \theta^4}\right)+\left(\frac{4}{r^4}\frac{\partial^2 w_s}{\partial \theta^2}\right)-\left(\frac{2}{r^3}\frac{\partial^3 w_s}{\partial r\partial \theta^2}\right)+\left(\frac{2}{r^2}\frac{\partial^4 w_s}{\partial r^2\partial \theta^2}\right)\right]\\
&-\frac{Eh}{1-\nu^2}\left[\left(\frac{1}{r^3}u_s\frac{\partial^2 w_s}{\partial \theta^2}\right)+\nu\left(\frac{1}{r^2}\frac{\partial u_s}{\partial r}\frac{\partial^2 w_s}{\partial \theta^2}\right)+\frac{1-\nu}{2}\left(\frac{1}{r^2}\frac{\partial^2 u_s}{\partial \theta^2}\frac{\partial w_s}{\partial r}\right)\right.\\
&+(1+\nu)\left(\frac{1}{r}\frac{\partial u_s}{\partial r}\frac{\partial w_s}{\partial r}\right)+\frac{1+\nu}{2}\left(\frac{1}{r^2}\frac{\partial^2 u_s}{\partial r\partial \theta}\frac{\partial w_s}{\partial \theta}\right)+\frac{1+\nu}{2}\left(\frac{1}{r^3}\frac{\partial u_s}{\partial \theta}\frac{\partial w_s}{\partial \theta}\right)\\
&\left.+(1-\nu)\left(\frac{1}{r^2}\frac{\partial u_s}{\partial \theta}\frac{\partial^2 w_s}{\partial r\partial \theta}\right)+\left(\frac{\partial^2 u_s}{\partial r^2}\frac{\partial w_s}{\partial r}\right)+\nu\left(\frac{u_s}{r}\frac{\partial^2 w_s}{\partial r^2}\right)+\left(\frac{\partial u_s}{\partial r}\frac{\partial^2 w_s}{\partial r^2}\right)\right]\\
&-\frac{Eh}{1-\nu^2}\left[\left(\frac{1}{r^3}\frac{\partial^2 v_s}{\partial \theta^2}\frac{\partial w_s}{\partial \theta}\right)+\left(\frac{1}{r^3}\frac{\partial v_s}{\partial \theta}\frac{\partial^2 w_s}{\partial \theta^2}\right)-\frac{1-\nu}{2}\left(\frac{1}{r^2}\frac{\partial v_s}{\partial r}\frac{\partial w_s}{\partial \theta}\right)\right.\\
&-\frac{1-\nu}{2}\left(\frac{1}{r^2}\frac{\partial v_s}{\partial \theta}\frac{\partial w_s}{\partial r}\right)+\frac{1+\nu}{2}\left(\frac{1}{r}\frac{\partial^2 v_s}{\partial r\partial \theta}\frac{\partial w_s}{\partial r}\right)+(1-\nu)\left(\frac{1}{r}\frac{\partial v_s}{\partial r}\frac{\partial^2 w_s}{\partial r\partial \theta}\right)\\
&\left.+\frac{1-\nu}{2}\left(\frac{v_s}{r^3}\frac{\partial w_s}{\partial \theta}\right)-(1-\nu)\left(\frac{v_s}{r^2}\frac{\partial^2 w_s}{\partial r\partial \theta}\right)-\frac{1-\nu}{2}\left(\frac{1}{r}\frac{\partial^2 v_s}{\partial r^2}\frac{\partial w_s}{\partial \theta}\right)+\frac{\nu}{r}\left(\frac{\partial v_s}{\partial \theta}\frac{\partial^2 w_s}{\partial r^2}\right)\right]\\
&-\frac{Eh}{1-\nu^2}\left[\frac{3}{2}\left(\frac{1}{r^4}\frac{\partial^2 w_s}{\partial \theta^2}\left(\frac{\partial w_s}{\partial \theta}\right)^2\right)-\frac{1}{2}\left(\frac{1}{r^3}\frac{\partial w_s}{\partial r}\left(\frac{\partial w_s}{\partial \theta}\right)^2\right)+\frac{1}{2}\left(\frac{1}{r^2}\frac{\partial^2 w_s}{\partial \theta^2}\left(\frac{\partial w_s}{\partial r}\right)^2\right)\right.\\
&+2\left(\frac{1}{r^2}\frac{\partial w_s}{\partial \theta}\frac{\partial w_s}{\partial r}\frac{\partial^2 w_s}{\partial r\partial \theta}\right)+\frac{1}{2}\left(\frac{1}{r^2}\frac{\partial^2 w_s}{\partial r^2}\left(\frac{\partial w_s}{\partial \theta}\right)^2\right)\\
&\left.+\frac{3}{2}\left(\frac{\partial^2 w_s}{\partial r^2}\left(\frac{\partial w_s}{\partial r}\right)^2\right)+\frac{1}{2}\left(\frac{1}{r}\left(\frac{\partial w_s}{\partial r}\right)^3\right)\right]+I_0\ddot{w}_s=0
\end{aligned}\tag{3.A11}$$

Subtracting Eq. (3.A11) from the result obtained by inserting Eq. (3.A10) into Eq. (3.A9) yields the nonlinear dynamic governing equation. Linearizing about the static equilibrium, this latter equation about the pre-deformed configuration $(u_s,\ v_s, w_s)$ yields

$$\begin{aligned}
&\frac{Eh^3}{12(1-\nu^2)}\left[\left(\frac{\partial^4 w_d}{\partial r^4}\right)+\left(\frac{2}{r}\frac{\partial^3 w_d}{\partial r^3}\right)-\left(\frac{1}{r^2}\frac{\partial^2 w_d}{\partial r^2}\right)+\left(\frac{1}{r^3}\frac{\partial w_d}{\partial r}\right)\right.\\
&\left.+\left(\frac{1}{r^4}\frac{\partial^4 w_d}{\partial \theta^4}\right)+\left(\frac{4}{r^4}\frac{\partial^2 w_d}{\partial \theta^2}\right)-\left(\frac{2}{r^3}\frac{\partial^3 w_d}{\partial r\partial \theta^2}\right)+\left(\frac{2}{r^2}\frac{\partial^4 w_d}{\partial r^2\partial \theta^2}\right)\right]\\
&-\frac{Eh}{1-\nu^2}\left[\left(\frac{1}{r^3}u_s\frac{\partial^2 w_d}{\partial \theta^2}\right)+\nu\left(\frac{1}{r^2}\frac{\partial u_s}{\partial r}\frac{\partial^2 w_d}{\partial \theta^2}\right)+\frac{1-\nu}{2}\left(\frac{1}{r^2}\frac{\partial^2 u_s}{\partial \theta^2}\frac{\partial w_d}{\partial r}\right)\right.\\
&+(1+\nu)\left(\frac{1}{r}\frac{\partial u_s}{\partial r}\frac{\partial w_d}{\partial r}\right)+\frac{1+\nu}{2}\left(\frac{1}{r^2}\frac{\partial^2 u_s}{\partial r\partial \theta}\frac{\partial w_d}{\partial \theta}\right)+\frac{1+\nu}{2}\left(\frac{1}{r^3}\frac{\partial u_s}{\partial \theta}\frac{\partial w_d}{\partial \theta}\right)\\
&\left.+(1-\nu)\left(\frac{1}{r^2}\frac{\partial u_s}{\partial \theta}\frac{\partial^2 w_d}{\partial r\partial \theta}\right)+\left(\frac{\partial^2 u_s}{\partial r^2}\frac{\partial w_d}{\partial r}\right)+\nu\left(\frac{u_s}{r}\frac{\partial^2 w_d}{\partial r^2}\right)+\left(\frac{\partial u_s}{\partial r}\frac{\partial^2 w_d}{\partial r^2}\right)\right]\\
&-\frac{Eh}{1-\nu^2}\left[\left(\frac{1}{r^3}\frac{\partial^2 v_s}{\partial \theta^2}\frac{\partial w_d}{\partial \theta}\right)+\left(\frac{1}{r^3}\frac{\partial v_s}{\partial \theta}\frac{\partial^2 w_d}{\partial \theta^2}\right)-\frac{1-\nu}{2}\left(\frac{1}{r^2}\frac{\partial v_s}{\partial r}\frac{\partial w_d}{\partial \theta}\right)\right.\\
&-\frac{1-\nu}{2}\left(\frac{1}{r^2}\frac{\partial v_s}{\partial \theta}\frac{\partial w_d}{\partial r}\right)+\frac{1+\nu}{2}\left(\frac{1}{r}\frac{\partial^2 v_s}{\partial r\partial \theta}\frac{\partial w_d}{\partial r}\right)+(1-\nu)\left(\frac{1}{r}\frac{\partial v_s}{\partial r}\frac{\partial^2 w_d}{\partial r\partial \theta}\right)\\
&\left.+\frac{1-\nu}{2}\left(\frac{v_s}{r^3}\frac{\partial w_d}{\partial \theta}\right)-(1-\nu)\left(\frac{v_s}{r^2}\frac{\partial^2 w_d}{\partial r\partial \theta}\right)+\frac{1-\nu}{2}\left(\frac{1}{r}\frac{\partial^2 v_s}{\partial r^2}\frac{\partial w_d}{\partial \theta}\right)+\frac{\nu}{r}\left(\frac{\partial v_s}{\partial \theta}\frac{\partial^2 w_d}{\partial r^2}\right)\right]\\
&-\frac{Eh}{1-\nu^2}\left[\frac{3}{2}\frac{1}{r^4}\left(\left(\frac{\partial w_s}{\partial \theta}\right)^2\frac{\partial^2 w_d}{\partial \theta^2}+2\frac{\partial w_s}{\partial \theta}\frac{\partial^2 w_s}{\partial \theta^2}\frac{\partial w_d}{\partial \theta}\right)\right.\\
&-\frac{1}{2}\left(\frac{1}{r^3}\left(\left(\frac{\partial w_s}{\partial \theta}\right)^2\frac{\partial w_d}{\partial r}+2\frac{\partial w_s}{\partial \theta}\frac{\partial w_s}{\partial r}\frac{\partial w_d}{\partial \theta}\right)\right)\\
&+\frac{1}{2}\left(\frac{1}{r^2}\left(\left(\frac{\partial w_s}{\partial r}\right)^2\frac{\partial^2 w_d}{\partial \theta^2}+2\frac{\partial w_s}{\partial r}\frac{\partial^2 w_s}{\partial \theta^2}\frac{\partial w_d}{\partial r}\right)\right)\\
&+2\left(\frac{1}{r^2}\left(\frac{\partial w_s}{\partial \theta}\frac{\partial w_s}{\partial r}\frac{\partial^2 w_d}{\partial r\partial \theta}+\frac{\partial w_s}{\partial \theta}\frac{\partial^2 w_s}{\partial r\partial \theta}\frac{\partial w_d}{\partial r}+\frac{\partial w_s}{\partial r}\frac{\partial^2 w_s}{\partial r\partial \theta}\frac{\partial w_d}{\partial \theta}\right)\right)\\
&+\frac{1}{2}\left(\frac{1}{r^2}\left(\left(\frac{\partial w_s}{\partial \theta}\right)^2\frac{\partial^2 w_d}{\partial r^2}+2\frac{\partial w_s}{\partial \theta}\frac{\partial^2 w_s}{\partial r^2}\frac{\partial w_d}{\partial \theta}\right)\right)\\
&\left.+\frac{3}{2}\left(\left(\frac{\partial w_s}{\partial r}\right)^2\frac{\partial^2 w_d}{\partial r^2}+2\frac{\partial w_s}{\partial r}\frac{\partial^2 w_s}{\partial r^2}\frac{\partial w_d}{\partial r}\right)+\frac{1}{2}\left(\frac{1}{r}3\left(\frac{\partial w_s}{\partial r}\right)^2\frac{\partial w_d}{\partial r}\right)\right]+I_0\ddot{w}_d=0.
\end{aligned}\tag{3.A12}$$

Next, to write Eq. (3.A12) in dimensionless form, we use the following non-dimensional parameters

$$\begin{aligned}&\bar w=\tfrac{w}{h},\quad \bar u=\tfrac{R}{h^2}u,\quad \bar v=\tfrac{R}{h^2}v,\\ &\bar r=\tfrac{r}{R},\quad \bar t=\tfrac{1}{R}\sqrt{\tfrac{E}{\rho}}\,t,\quad \Gamma=\tfrac{h^2}{R^2(1-\nu^2)},\end{aligned}\tag{3.A13}$$

and obtain the following non-dimensional form of (3.A12)

$$\begin{aligned}
&\frac{\Gamma}{12}\Bigg[\Big(\frac{\partial^4\varphi}{\partial\bar r^4}\Big)+\Big(\frac{2}{\bar r}\frac{\partial^3\varphi}{\partial\bar r^3}\Big)-\Big(\frac{1}{\bar r^2}\frac{\partial^2\varphi}{\partial\bar r^2}\Big)+\Big(\frac{1}{\bar r^3}\frac{\partial\varphi}{\partial\bar r}\Big)\\
&+\Big(\frac{1}{\bar r^4}\frac{\partial^4\varphi}{\partial\theta^4}\Big)+\Big(\frac{4}{\bar r^4}\frac{\partial^2\varphi}{\partial\theta^2}\Big)-\Big(\frac{2}{\bar r^3}\frac{\partial^3\varphi}{\partial\bar r\partial\theta^2}\Big)+\Big(\frac{2}{\bar r^2}\frac{\partial^4\varphi}{\partial\bar r^2\partial\theta^2}\Big)\Bigg]\\
&-\Gamma\Bigg[\Big(\frac{1}{\bar r^3}\bar u_s\frac{\partial^2\varphi}{\partial\theta^2}\Big)+\bar u\Big(\frac{1}{\bar r^2}\frac{\partial\bar u_s}{\partial\bar r}\frac{\partial^2\varphi}{\partial\theta^2}\Big)+\frac{1-\nu}{2}\Big(\frac{1}{\bar r^2}\frac{\partial^2\bar u_s}{\partial\theta^2}\frac{\partial\varphi}{\partial\bar r}\Big)\\
&+(1+\nu)\Big(\frac{1}{\bar r}\frac{\partial\bar u_s}{\partial\bar r}\frac{\partial\varphi}{\partial\bar r}\Big)+\frac{1+\nu}{2}\Big(\frac{1}{\bar r^2}\frac{\partial^2\bar u_s}{\partial\bar r\partial\theta}\frac{\partial\varphi}{\partial\theta}\Big)+\frac{1+\nu}{2}\Big(\frac{1}{\bar r^3}\frac{\partial\bar u_s}{\partial\theta}\frac{\partial\varphi}{\partial\theta}\Big)\\
&+(1-\nu)\Big(\frac{1}{\bar r^2}\frac{\partial\bar u_s}{\partial\theta}\frac{\partial^2\varphi}{\partial\bar r\partial\theta}\Big)+\Big(\frac{\partial^2\bar u_s}{\partial\bar r^2}\frac{\partial\varphi}{\partial\bar r}\Big)+\nu\Big(\frac{\bar u_s}{\bar r}\frac{\partial^2\varphi}{\partial\bar r^2}\Big)+\Big(\frac{\partial\bar u_s}{\partial\bar r}\frac{\partial^2\varphi}{\partial\bar r^2}\Big)\Bigg]\\
&-\Gamma\Bigg[\Big(\frac{1}{\bar r^3}\frac{\partial^2\bar v_s}{\partial\theta^2}\frac{\partial\varphi}{\partial\theta}\Big)+\Big(\frac{1}{\bar r^3}\frac{\partial\bar v_s}{\partial\theta}\frac{\partial^2\varphi}{\partial\theta^2}\Big)-\frac{1-\nu}{2}\Big(\frac{1}{\bar r^2}\frac{\partial\bar v_s}{\partial\bar r}\frac{\partial\varphi}{\partial\theta}\Big)\\
&-\frac{1-\nu}{2}\Big(\frac{1}{\bar r^2}\frac{\partial\bar v_s}{\partial\theta}\frac{\partial\varphi}{\partial\bar r}\Big)+\frac{1+\nu}{2}\Big(\frac{1}{\bar r}\frac{\partial^2\bar v_s}{\partial\bar r\partial\theta}\frac{\partial\varphi}{\partial\bar r}\Big)+(1-\nu)\Big(\frac{1}{\bar r}\frac{\partial\bar v_s}{\partial\bar r}\frac{\partial^2\varphi}{\partial\bar r\partial\theta}\Big)\\
&+\frac{1-\nu}{2}\Big(\frac{\bar v_s}{\bar r^3}\frac{\partial\varphi}{\partial\theta}\Big)-(1-\nu)\Big(\frac{\bar v_s}{\bar r^2}\frac{\partial^2\varphi}{\partial\bar r\partial\theta}\Big)+\frac{1-\nu}{2}\Big(\frac{1}{\bar r}\frac{\partial^2\bar v_s}{\partial\bar r^2}\frac{\partial\varphi}{\partial\theta}\Big)+\frac{\nu}{\bar r}\Big(\frac{\partial\bar v_s}{\partial\theta}\frac{\partial^2\varphi}{\partial\bar r^2}\Big)\Bigg]\\
&-\Gamma\Bigg[\frac{3}{2}\frac{1}{\bar r^4}\Bigg(\Big(\frac{\partial\bar w_s}{\partial\theta}\Big)^2\frac{\partial^2\varphi}{\partial\theta^2}+2\frac{\partial\bar w_s}{\partial\theta}\frac{\partial^2\bar w_s}{\partial\theta^2}\frac{\partial\varphi}{\partial\theta}\Bigg)\\
&-\frac{1}{2}\Bigg(\frac{1}{\bar r^3}\Bigg(\Big(\frac{\partial\bar w_s}{\partial\theta}\Big)^2\frac{\partial\varphi}{\partial\bar r}+2\frac{\partial\bar w_s}{\partial\theta}\frac{\partial\bar w_s}{\partial\bar r}\frac{\partial\varphi}{\partial\theta}\Bigg)\Bigg)\\
&+\frac{1}{2}\Bigg(\frac{1}{\bar r^2}\Bigg(\Big(\frac{\partial\bar w_s}{\partial\bar r}\Big)^2\frac{\partial^2\varphi}{\partial\theta^2}+2\frac{\partial\bar w_s}{\partial\bar r}\frac{\partial^2\bar w_s}{\partial\theta^2}\frac{\partial\varphi}{\partial\bar r}\Bigg)\Bigg)\\
&+2\Bigg(\frac{1}{\bar r^2}\Bigg(\frac{\partial\bar w_s}{\partial\theta}\frac{\partial\bar w_s}{\partial\bar r}\frac{\partial^2\varphi}{\partial\bar r\partial\theta}+\frac{\partial\bar w_s}{\partial\theta}\frac{\partial^2\bar w_s}{\partial\bar r\partial\theta}\frac{\partial\varphi}{\partial\bar r}+\frac{\partial\bar w_s}{\partial\bar r}\frac{\partial^2\bar w_s}{\partial\bar r\partial\theta}\frac{\partial\varphi}{\partial\theta}\Bigg)\Bigg)\\
&+\frac{1}{2}\Bigg(\frac{1}{\bar r^2}\Bigg(\Big(\frac{\partial\bar w_s}{\partial\theta}\Big)^2\frac{\partial^2\varphi}{\partial\bar r^2}+2\frac{\partial\bar w_s}{\partial\theta}\frac{\partial^2\bar w_s}{\partial\bar r^2}\frac{\partial\varphi}{\partial\theta}\Bigg)\Bigg)\\
&+\frac{3}{2}\Bigg(\Big(\frac{\partial\bar w_s}{\partial\bar r}\Big)^2\frac{\partial^2\varphi}{\partial\bar r^2}+2\frac{\partial\bar w_s}{\partial\bar r}\frac{\partial^2\bar w_s}{\partial\bar r^2}\frac{\partial\varphi}{\partial\bar r}\Bigg)+\frac{1}{2}\Bigg(\frac{1}{\bar r}3\Big(\frac{\partial\bar w_s}{\partial\bar r}\Big)^2\frac{\partial\varphi}{\partial\bar r}\Bigg)\Bigg]=\bar\omega^2\varphi.
\end{aligned}\tag{3.A14}$$

3.A3. DISCRETIZATION OF THE GOVERNING EQUATIONS

In this Note we discuss how by using vibrational modes and frequencies of the drum, it is possible to find the unknown displacement field $\bar u_s$, $\bar v_s$, and $\bar w_s$ and thus the stress distribution.

Our analysis starts from Eq. (3.A14). This equation incorporates the known resonance frequencies $\bar\omega$ and mode shapes φ as parameters that can be measured from experiments. Naturally to determine the three unknowns $\bar u_s$, $\bar v_s$, and $\bar w_s$ from this equation, one would need to account for minimum three sets of mode shapes (φ_1, φ_2, φ_3) and their corresponding frequencies ($\bar\omega_1$, $\bar\omega_2$, $\bar\omega_3$), and solve the set of nonlinear partial differential equations using a numerical procedure e.g. Finite Element Method (FEM), Finite Difference Method (FDM) or method of Differential Quadratures (DQ).

Here, we make use of the DQ method [54] to solve the equations of motion for the unknown displacement field. The DQ method transforms Eq. (3.A14) into a set of nonlinear algebraic equations by approximating partial derivatives of functions at discrete points. We particularly apply polynomial-based Differential Quadrature (PDQ) in the radial direction, while we use Fourier Expansion-based Differential Quadrature (FDQ) in the azimuthal direction. This combination ensures accurate results in both r and θ directions and handles periodic domains effectively due to FDQ's inherent periodicity.

In order to apply DQ method, one would first need to discretize partial derivatives of given functions. Here, we denote the a-th derivative of a function $f(x)$ as $\partial^a f/\partial x^a$. We then express this derivative as a linear combination of the function values at discrete points along the corresponding coordinate direction, given by [54]

$$\left.\frac{\partial^a f(x)}{\partial x^a}\right|_{x=x_i} = \sum_{j=1}^{n} A_{i,j}^{(a)} f\left(x_j\right), \tag{3.A15}$$

where n is the number of total discrete grid points used in the approximation and $A_{i,j}^{(a)}$ are weighting coefficients. Based on the choice of basis functions for the approximation, different sets of weighting coefficients will be obtained. When PDQ is used, the weighting coefficients of the first derivative are determined as [54]

$$A_{i,j}^{(1)} = \frac{M\left(x_i\right)}{\left(x_i - x_j\right) M\left(x_j\right)} \quad \left(i, j = 1, 2, ..., n; i \neq j\right) \tag{3.A16}$$

where

$$M\left(x_i\right) = \prod_{i=1, i\neq j}^{n} \left(x_i - x_j\right). \tag{3.A17}$$

The weighting coefficients of higher-order derivatives can then be obtained through the following recurrence relation

$$A_{i,j}^{(a)} = \begin{cases} a\left[A_{i,j}^{(a-1)} A_{i,j}^{(1)} - \frac{A_{i,j}^{(a-1)}}{x_i - x_j}\right] & i \neq j \\ -\sum\limits_{j=1}^{n} A_{i,j}^{(a)} & i = j \end{cases}, \tag{3.A18}$$

where $\left(i, j = 1, 2, ..., n;\ 2 \leq a \leq n-1\right)$. However, if FDQ is used, the weighting coefficients of the first derivative are [54]

$$A_{i,j}^{(1)} = \frac{M\left(x_i\right)}{\left(x_i - x_j\right) M\left(x_j\right)} \quad \left(i, j = 1, 2, ..., n; i \neq j\right) \tag{3.A19}$$

where

$$M\left(x_i\right) = \prod_{i=1, i\neq j}^{n} \sin\left(\frac{\left(x_i - x_j\right)}{2}\right). \tag{3.A20}$$

The weighting coefficients of higher-order derivatives can be obtained through the following recurrence relation

$$A_{i,j}^{(a)} = \begin{cases} \frac{M(x_i)}{2\sin\left(\frac{x_i - x_j}{2}\right) M(x_j)} & i \neq j \\ -\sum\limits_{j=1}^{n} A_{i,j}^{(a)} & i = j \end{cases}, \tag{3.A21}$$

where $\left(i, j = 1, 2, ..., n;\ 2 \leq a \leq n-1\right)$. As pointed out earlier, since we have periodicity in the azimutal direction in circular drums, we opt for FDQ in θ direction and PDQ in the radial. Using these two procedures we then find the following set of discretized derivatives:

$$\begin{aligned}
\frac{\partial^a f}{\partial r^a} &= \sum_{k=1}^{N} C^{(a)}_{i,k} F_{k,j}, \\
\frac{\partial^a f}{\partial \theta^a} &= \sum_{k=1}^{M} \bar{C}^{(a)}_{i,k} F_{k,j}, \\
\frac{\partial^{a+b} f}{\partial r^a \partial \theta^b} &= \sum_{k_1=1}^{N} \sum_{k_2=1}^{M} C^{(a)}_{i,k_1} \bar{C}^{(b)}_{j,k_2} F_{k_1,k_2},
\end{aligned} \tag{3.A22}$$

where f is the parameter to be differentiated, $F_{i,j}$ is the value of f at node (i, j), $C^{(a)}_{i,j}$ are the PDQ weight coefficients for domain $\bar{r} \in [0,1]$, and $\bar{C}^{(b)}_{j,k_2}$ are the FDQ weight coefficients for the domain $\theta \in [0, 2\pi)$.

We note that in estimating stress distributions, the selection of an appropriate mesh distribution is an important factor that can very well affect the accuracy of the obtained displacement field and thus stress distribution. This is particularly important when calculating derivatives at the boundary conditions and ensuring the fulfillment of derivative constraints at the boundaries. Inadequate mesh distribution, characterized by a low number of nodes at the boundaries, may lead to inaccurate stress values near the edges. This likely accounts for the observed diminished accuracy near boundaries, as observed by Waitz et al. [30]. By applying appropriate mesh refinement strategies, we can effectively mitigate potential errors and enhance the overall accuracy of our numerical computations. One effective approach to address this issue is to increase the number of nodes near the edges compared to the main domain. In our DQ analysis, considering the periodicity in the azimuthal direction, we chose a uniform node distribution. However, for the radial direction, where boundary conditions are present, we utilized a Chebyshev-Gauss-Lobatto distribution [55]:

$$\bar{r}_i = \frac{1}{2}\left[1 - \cos\left(\frac{i-1}{N-1}\pi\right)\right].\ i = 1,\ 2,\ \ldots,\ N \tag{3.A23}$$

This distribution is defined as a non-uniform spacing of nodes which concentrates more nodes near the boundaries and fewer nodes in the central region. The Chebyshev-Gauss-Lobatto distribution ensures better resolution near the boundaries, where accurate approximation of derivatives is important, while maintaining an appropriate node spacing throughout the domain.

Applying boundary conditions is another important consideration when solving the equations using the DQ method. In the θ-direction, the periodicity is automatically satisfied due to the FDQ formulation. However, in the radial direction ($\bar{r}$-direction), since the DQ method discretizes the strong form of the 4th-order partial differential equation, we need to specify two boundary conditions for each of the edges corresponding to $\bar{r} = 0$ and $\bar{r} = 1$. This differs from FEM, which solves the weak form of the governing equations. The boundary condition for $\bar{r} = 1$ is a clamped condition which can be formulated as

$$\begin{aligned}
&\Phi_{N,j} = 0, \\
&\left.\frac{\partial \varphi}{\partial \bar{r}}\right|_{\bar{r}=1} = \sum_{k=1}^{N} C^{(1)}_{N,k} \Phi_{k,j} = 0.
\end{aligned} \tag{3.A24}$$

In contrast to rectangular geometry, which features well-defined boundaries, circular geometry lacks a tangible edge at the center. Analytical formulations address this challenge by omitting terms that approach infinity at the center of the circular membrane/-plate. However, determining the boundary condition (regularity condition) at the center in a numerical approach is not straightforward, and various methods exist to tackle this issue [56]. Among different approaches, the most promising regularity boundary condition is defined for two different types of mode shapes. In this approach mode shapes that exhibit nodal lines are subject to the regularity condition expressed as follows [56]

$$\begin{aligned}\left.\frac{\partial\varphi}{\partial\bar{r}}\right|_{\bar{r}=0} &= \sum_{k=1}^{N} C^{(1)}_{1,k}\Phi_{k,j} = 0,\\ \left.\frac{\partial^3\varphi}{\partial\bar{r}^3}\right|_{\bar{r}=0} &= \sum_{k=1}^{N} C^{(3)}_{1,k}\Phi_{k,j} = 0.\end{aligned} \tag{3.A25}$$

While for mode shapes without nodal lines, the regularity condition can be expressed as [56]

$$\begin{aligned}&\Phi_{1,j} = 0,\\ &\left.\frac{\partial^2\varphi}{\partial\bar{r}^2}\right|_{\bar{r}=0} = \sum_{k=1}^{N} C^{(2)}_{1,k}\Phi_{k,j} = 0.\end{aligned} \tag{3.A26}$$

As a result by solving Eq.s (3.A25) and Eq.s (3.A24) simultaneously, we find

$$\begin{aligned}\Phi_{1,j} &= \tfrac{1}{G}\sum_{k=3}^{N-2} G_{1,k}\Phi_{k,j},\\ \Phi_{2,j} &= \tfrac{1}{G}\sum_{k=3}^{N-2} G_{2,k}\Phi_{k,j},\\ \Phi_{N-1,j} &= \tfrac{1}{G}\sum_{k=3}^{N-2} G_{N-1,k}\Phi_{k,j},\end{aligned} \tag{3.A27}$$

where

$$\begin{aligned}G &= \left(C^{(1)}_{1,N-1}C^{(3)}_{1,2} - C^{(1)}_{1,2}C^{(3)}_{1,N-1}\right)C^{(1)}_{N,1} + \left(C^{(1)}_{1,1}C^{(3)}_{1,N-1} - C^{(1)}_{1,N-1}C^{(3)}_{1,1}\right)C^{(1)}_{N,2} + \left(C^{(1)}_{1,2}C^{(3)}_{1,1} - C^{(1)}_{1,1}C^{(3)}_{1,2}\right)C^{(1)}_{N,N-1},\\ G_{1,k} &= \left(C^{(3)}_{1,2}C^{(1)}_{N,N-1} - C^{(3)}_{1,N-1}C^{(1)}_{N,2}\right)C^{(1)}_{1,j} + \left(C^{(1)}_{1,N-1}C^{(1)}_{N,2} - C^{(1)}_{1,2}C^{(1)}_{N,N-1}\right)C^{(3)}_{1,j} + \left(C^{(1)}_{1,2}C^{(3)}_{1,N-1} - C^{(1)}_{1,N-1}C^{(3)}_{1,2}\right)C^{(1)}_{N,j},\\ G_{2,k} &= \left(C^{(3)}_{1,N-1}C^{(1)}_{N,1} - C^{(3)}_{1,1}C^{(1)}_{N,N-1}\right)C^{(1)}_{1,j} + \left(C^{(1)}_{1,1}C^{(1)}_{N,N-1} - C^{(1)}_{1,N-1}C^{(1)}_{N,1}\right)C^{(3)}_{1,j} + \left(C^{(1)}_{1,N-1}C^{(3)}_{1,1} - C^{(1)}_{1,1}C^{(3)}_{1,N-1}\right)C^{(1)}_{N,j},\\ G_{N-1,k} &= \left(C^{(3)}_{1,1}C^{(1)}_{N,2} - C^{(3)}_{1,2}C^{(1)}_{N,1}\right)C^{(1)}_{1,j} + \left(C^{(1)}_{1,2}C^{(1)}_{N,1} - C^{(1)}_{1,1}C^{(1)}_{N,2}\right)C^{(3)}_{1,j} + \left(C^{(1)}_{1,1}C^{(3)}_{1,2} - C^{(1)}_{1,2}C^{(3)}_{1,1}\right)C^{(1)}_{N,j}.\end{aligned} \tag{3.A28}$$

And by solving Eq.s (3.A26), and Eq.s (3.A24) we obtain

$$\begin{aligned}\Phi_{1,j} &= 0\\ \Phi_{2,j} &= \tfrac{1}{H}\sum_{k=3}^{N-2} H_{2,k}\Phi_{k,j},\\ \Phi_{N-1,j} &= \tfrac{1}{H}\sum_{k=3}^{N-2} H_{N-1,k}\Phi_{k,j},\end{aligned} \tag{3.A29}$$

where

$$\begin{aligned}H &= C^{(1)}_{N,2}C^{(2)}_{1,N-1} - C^{(2)}_{1,2}C^{(1)}_{N,N-1},\\ H_{2,k} &= C^{(1)}_{N,N-1}C^{(2)}_{1,k} - C^{(2)}_{1,N-1}C^{(1)}_{N,k},\\ H_{N-1,k} &= C^{(2)}_{1,2}C^{(1)}_{N,k} - C^{(1)}_{N,2}C^{(2)}_{1,k},\end{aligned} \tag{3.A30}$$

Thus, for the derivatives of $\bar{w}$, Eq. (3.A22) will be modified as

$$\begin{aligned}
\frac{\partial^a \varphi}{\partial r^a} &= C_{i,1}^{(a)} \Phi_{1,j} + C_{i,2}^{(a)} \Phi_{2,j} + C_{i,N-1}^{(a)} \Phi_{N-1,j} + \sum_{k=3}^{N-2} C_{i,k}^{(a)} \Phi_{k,j}, \\
\frac{\partial^a \varphi}{\partial \theta^a} &= \sum_{k=1}^{M} \bar{C}_{i,k}^{(a)} \Phi_{k,j}, \\
\frac{\partial^{a+b} \varphi}{\partial r^a \partial \theta^b} &= \sum_{k_2=1}^{M} C_{i,1}^{(a)} \bar{C}_{j,k_2}^{(b)} \Phi_{1,k_2} + \sum_{k_2=1}^{M} C_{i,2}^{(a)} \bar{C}_{j,k_2}^{(b)} \Phi_{2,k_2} + \sum_{k_2=1}^{M} C_{i,N-1}^{(a)} \bar{C}_{j,k_2}^{(b)} \Phi_{N-1,k_2} \\
&\quad + \sum_{k_1=3}^{N-2} \sum_{k_2=1}^{M} C_{i,k_1}^{(a)} \bar{C}_{j,k_2}^{(b)} \Phi_{k_1,k_2},
\end{aligned} \tag{3.A31}$$

where, based on the type of mode shape used, $\Phi_{1,j}$, $\Phi_{2,j}$, and $\Phi_{N-1,j}$ should be obtained from (3.A27) or Eq.s (3.A29). As can be seen, the modified derivatives are no longer applied to the whole domain, but only to the interior domain without the two adjacent rows of nodes to the edges.

Finally, the discretized version of Eq. (3.A14) can be written in a matrix-form as

$$\begin{aligned}
&\sum_{k_u} \left[\left(\mathbf{D}_{u\varphi}^{k_u} \Phi_{i,j} \right) \mathbf{D}_{U}^{k_u} \right] U_{i,j} + \sum_{k_v} \left[\left(\mathbf{D}_{v\varphi}^{k_v} \Phi_{i,j} \right) \mathbf{D}_{V}^{k_v} \right] V_{i,j} \\
&+ \sum_{k_w} \left[\mathbf{D}_{w\varphi}^{k_w} \Phi_{i,j} \right] \left[\left(\bar{\mathbf{D}}_{\mathbf{W}}^{k_w} W_{i,j} \right) \cdot \left(\bar{\bar{\mathbf{D}}}_{\mathbf{W}}^{k_w} W_{i,j} \right) \right] = \left(\bar{\omega}^2 I - \mathbf{D}_{\mathbf{W}} \right) \Phi_{i,j},
\end{aligned} \tag{3.A32}$$

where $U_{i,j}$, $V_{i,j}$, and $W_{i,j}$ denote the static deformation values at each nodes and are the vectors of unknowns. $\Phi_{i,j}$ and $\bar{\omega}$ denote normalized mode shape values at each node and the corresponding resonance frequency, respectively, and are known parameter. $\mathbf{D}_{u\varphi}^{k_u}$, $\mathbf{D}_{v\varphi}^{k_v}$, $\mathbf{D}_{w\varphi}^{k_w}$, $\mathbf{D}_{U}^{k_u}$, $\mathbf{D}_{V}^{k_v}$, $\mathbf{D}_{\mathbf{W}}$, $\bar{\mathbf{D}}_{\mathbf{W}}^{k_w}$, and $\bar{\bar{\mathbf{D}}}_{\mathbf{W}}^{k_w}$ are matrices which are function of DQ weighting coefficients.

3.A4. ROBUSTNESS OF THE DQ SOLUTION

We note that Eq. (3.A32) invovles nonlinear terms solely related to transverse static displacement field. If the drum is flat ($W_{i,j} = 0$), the equation will be considerably simplified (one would solely need to solve for $U_{i,j}$, and $V_{i,j}$). Consequently, instead of having $3 \times M \times N$ unknowns (where M represents the number of nodes in the θ direction and N signifies the number of nodes in the $\bar{r}$ direction), we will only have $2 \times M \times N$ unknowns. This suggests that two mode shapes and their corresponding resonance frequencies will be sufficient for extracting the unknown displacements. However, it is important to note that the nodes on the clamped edge have a value of zero, which results in $\Phi_{i,j} = 0$ on the edge, and consequently, we have the trivial $0 = 0$ equation on the edge nodes, indicating that we still require at least three mode shapes and frequencies to have more equations than unknowns and be able to extract displacement fields using a least squares procedure.

To assess the validity of our methodology and equations, we initiated a verification procedure by artificially generating a radial displacement field represented as

$$u(r,\theta) = 5 \times 10^{-6} \frac{r}{R} J_6 \left(9.93611 \frac{r}{R} \right) (1 + \sin(2\theta)). \tag{3.A33}$$

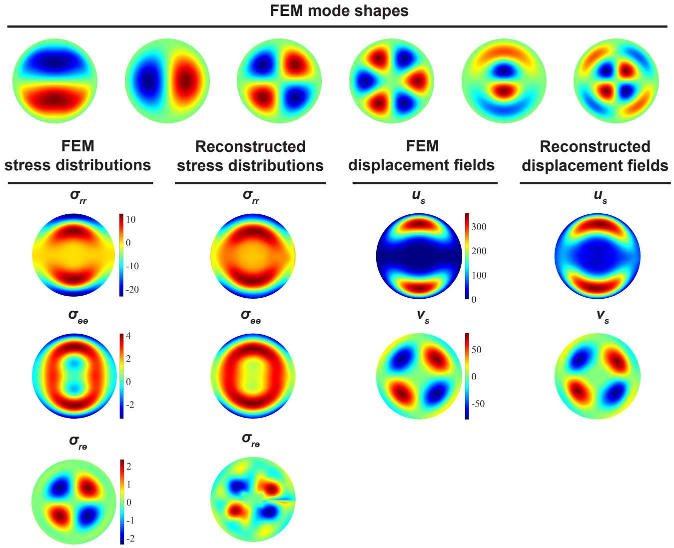

Figure 3.A2: Reconstruction of stress distribution and displacement field for an artificial FEM case. Within the FEM software, by assuming an artificial radial displacement denoted in Eq. (3.A34), first azimuthal displacement field is obtained using a static equilibrium analysis, and tehn the corresponding stress distributions and mode shapes are computed using postprocessing and a modal analysis, respectively. Eq. (3.A32) is then used to reconstruct displacement fields from FEM mode shapes. The displacement and stress values are shown in the non-dimensional form.

This artificial displacement was then introduced into a FEM software package with the constraint $w = 0$. The resulting equilibrium displacement field v was subsequently obtained. Employing the values of u, v, and w, we computed the corresponding stress distributions. Following this, a modal analysis was conducted to ascertain the resultant mode shapes. It is worth mentioning that here, graphene is considered as the constituent material with $E = 1$ TPa, $\rho = 2300$ kg.m^{-3}, and $\nu = 0.16$. Furthermore, all the parameters are made dimensionless, and the $h/R = 0.001$.

Next, we employed the FEM mode shapes and their corresponding resonance frequencies as inputs in our Eq. (3.A32) to reconstruct the displacement fields and stress distributions. The results of this reconstruction using six different mode shapes are shown in Fig. (3.A2). Notably, the reconstructed displacement fields exhibit high accuracy, closely resembling the FEM displacement field. Similarly, the calculation of normal stresses demonstrates decent precision. However, it is important to recognize that shear stress accuracy is relatively lower in comparison. This limitation stems from shear stress's substantially smaller amplitude as compared to normal stresses, as well as its comparable amplitude to numerical error created during the differentiation process.

We created a second test scenario (same material and geometric properties as previous case) to confirm that the prior one was not a coincidence. The radial displacement field is formulated as

$$u(r,\theta) = 3\times 10^{-6}\left(\frac{r}{R}\right)^2 (0.5+\sin(\theta))\,.$$

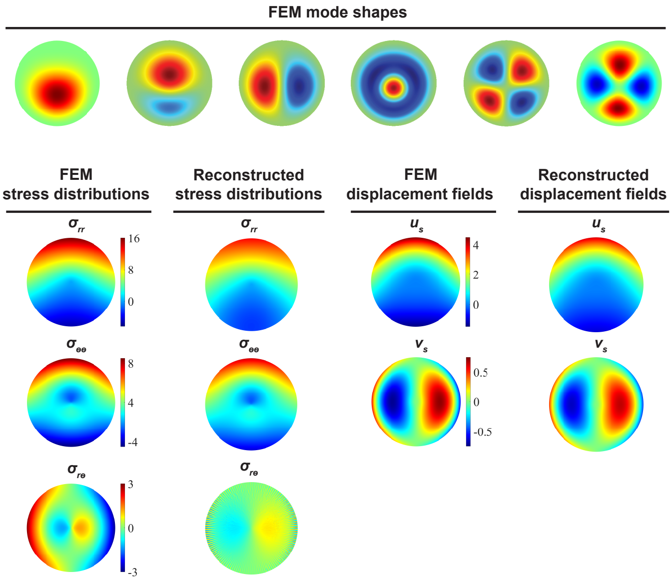

Figure 3.A3: Reconstruction of stress distribution and displacement field for an artificial FEM case. Within the FEM software, by assuming an artificial radial displacement denoted in Eq. (3.A33), first azimuthal displacement field is obtained using a static equilibrium analysis, and tehn the corresponding stress distributions and mode shapes are computed using postprocessing and a modal analysis, respectively. Eq. (3.A32) is then used to reconstruct displacement fields from FEM mode shapes. The displacement and stress values are shown in the non-dimensional form.

Fig. (3.A3) displays the results of this reconstruction with six distinct mode shapes. As can be observed, the reconstructed displacement fields are reasonably precise and closely resemble the FEM displacement field. Similarly, the estimation of normal stresses is relatively accurate. However, it is important to note that shear stress accuracy is rather poor.

Another crucial aspect to consider is the robustness of our method in the presence of noise and inaccuracies in the measured mode shapes. To evaluate this, we introduced random noise to the mode shapes obtained from the previous analysis. Specifically, we added random two-dimensional Gaussian noise with a maximum amplitude of less than 0.05 times the local deflection to the original mode shapes shown in Fig. (3.A2).

Subsequently, we employed a fitting procedure for the noisy mode shapes, which is detailed in the main text and the following Note. This fitting procedure employs a finite set of circular plate mode shapes as

$$\begin{aligned}\varphi(r,\theta) = &\sum_{m=0}^{M_f}\sum_{n=0}^{N_f}\left[\mathrm{A}_n J_n(\lambda_{m,n}\tfrac{r}{R}) + \mathrm{B}_n I_n(\lambda_{m,n}\tfrac{r}{R})\right]\cos(n\theta)\\ &+ \sum_{m=0}^{M_f}\sum_{n=1}^{N_f}\left[\mathrm{A}_n^{*} J_n(\lambda_{m,n}\tfrac{r}{R}) + \mathrm{B}_n^{*} I_n(\lambda_{m,n}\tfrac{r}{R})\right]\sin(n\theta),\end{aligned} \tag{3.A34}$$

to approximate and enhance the quality of the noisy mode shapes. Here, M_f, and N_f are the number of radial and azimuthal coordinates chosen for fitting. A_n, A_n^{*}, B_n, and

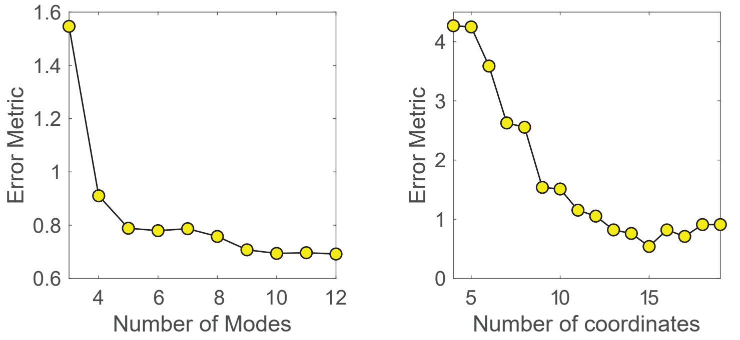

Figure 3.A4: DQ solution's robustness in the presence of noise on measured mode shapes. a) The error metric (3.A36) of the proposed solution as a function of the number of experimental mode shapes employed in the solution procedure. As demonstrated, adding more mode shapes reduces the error of the solution by averaging the noise in the measured mode shapes; however, after five modes, adding more mode shapes does not significantly improve accuracy. (b) The error metric (3.A36) of the proposed solution as a function of the number of fitting coordinates employed to fit the mode shapes (see Eq. (3.A34)). Fewer coordinates result in greater smoothing, whereas a larger number of coordinates follows all local curvatures, which may be artefacts of noise or measurement errors.

B_n^* are the fitting parameters which can be found through the fitting procedure. Here, J_n, and I_n denote Bessel function of the first kind of n-th order, and modified Bessel function of first kind of the n-th order, respectively. $\lambda_{m,n}$ represents the corresponding eigenfrequency of the plate which can be found from the following equation [27]

$$\frac{J_{n+1}\left(\lambda_{m,n}\right)}{J_n\left(\lambda_{m,n}\right)}+\frac{I_{n+1}\left(\lambda_{m,n}\right)}{I_n\left(\lambda_{m,n}\right)}=0. \tag{3.A35}$$

We evaluated the method's accuracy based on the implications of varying the number of experimental mode shapes employed in the fitting procedure (See Fig. 4a) and the number of plate modes (coordinates) utilized in the fitting process (See Fig. 4b). This allowed us to conduct a parametric study to ascertain whether a good fit, encompassing both the true mode shape and the spurious displacements arising from noise, or a smoother fit with a lower number of coordinates (and accordingly lower R^2 value), proves to be more suitable. In order to evaluate the accuracy of our method, we introduce an error metric as

$$EM=\left[\frac{\int\limits_0^{2\pi}\int\limits_0^{R}\left(\sigma_{rr}^{predict}-\sigma_{rr}^{real}\right)^2 r\,dr\,d\theta}{\int\limits_0^{2\pi}\int\limits_0^{R}\left(\sigma_{rr}^{real}\right)^2 r\,dr\,d\theta}\right]^{1/2} \tag{3.A36}$$

where $\sigma_{rr}^{predict}$ denotes the predicted normal stress obtained using Eq. (3.A29), and σ_{rr}^{real} is the normal stress that is artificially created at the beginning of the procedure. The results of our analysis indicated that we require a fitting procedure with a high degree of accuracy, but also a certain level of smoothing to mitigate the impact of noise (Fig. (3.A4)).

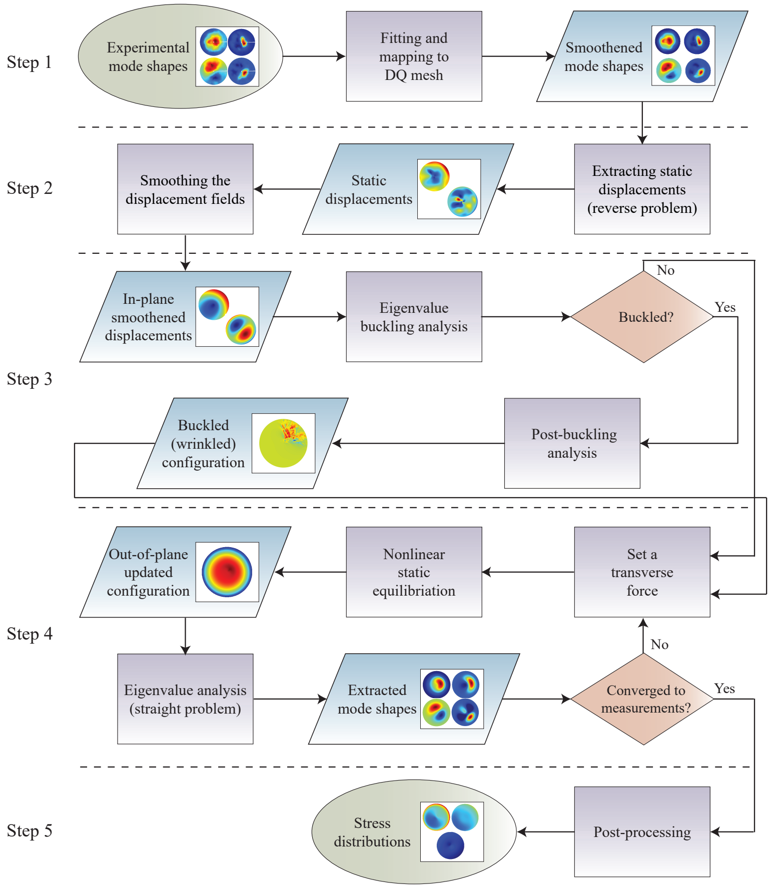

Figure 3.A5: The flowchart for deriving stress distributions from experimental mode shapes and resonance frequencies.

3.A5. EXTRACTING THE STRESS DISTRIBUTIONS

To determine the static displacement fields ($U_{i,j}$, $V_{i,j}$, and $W_{i,j}$) in suspended drums, we expand the methodology explained earlier on numerical simulations to experimental measurements so as to extract the nonuniform stress distributions. The procedure, illustrated in Fig. 3.A5, involves several steps to ensure accurate and reliable results. A minimum of three sets of mode shapes and their corresponding resonance frequencies are required as inputs. These mode shapes capture the vibrational behavior of the drums and serve as the basis for reconstructing the displacement fields and stress distributions. It is important to note that our method is applicable only to drums with small deviations from a parabolically-bulged configuration.

To prepare the experimental data for numerical analysis, we address several challenges associated with the mode shapes. These include noise, discreteness, non-zero values on boundaries, and the need for a smooth and continuous representation of the mode shapes. To tackle these challenges, the mode shapes are transformed to polar coordinates and fitted with a plane to remove edge effects and establish zero value at the boundaries. The resulting mode shapes are then smoothed and transferred to the DQ mesh, ensuring that the fitted shapes satisfy the boundary conditions necessary for accurate numerical analysis. Thus, we chose to use plate mode shapes as the basis for fitting the processed experimental mode shapes. The fitting equation used is Eq. (3.A34) defined in the last Note.

Having obtained the fitted mode shapes, we proceed to solve the reverse problem i.e. finding displacement field from resonance frequencies and mode shapes, by assuming a parabolic transverse deflection profile for the out-of-plane displacement field using Eq. (3.A32). The static displacement fields are determined by solving the nonlinear algebraic Eq.s (3.A32). A least squares procedure is employed, to ensure accurate reconstruction of the in-plane displacements and a first approximation of the out-of-plane deflection. For the sake of numerical robustness, we applied a smoothing operation to the obtained radial displacement field u using a Savitzky-Golay Finite Impulse Response (FIR) filter. Specifically, when the magnitudes of the in-plane displacement field v were comparable to those of u, a Savitzky-Golay FIR filter was also employed for smoothing v. Conversely, in cases where the values of v were significantly smaller than those of u, we exclusively utilized a FEM solver to determine the equilibrium state of v. This decision arises from the acknowledgment that when v is significantly smaller than u, it becomes more vulnerable to numerical errors, as its values may either approach or be in the vicinity of the numerical error order.

An important consideration is the validation of the initial approximation. To assess its adequacy, an eigenvalue buckling analysis is performed. If the in-plane displacement field leads to a stable drum without buckling, the initial approximation is deemed satisfactory. However, when non-uniform in-plane displacements result in instability and buckling, a post-buckling analysis is conducted to obtain a more realistic deformation pattern.

In the fourth step of our analysis, we evaluate the adequacy of the in-plane displacement fields and the deformed configuration obtained thus far. However, it is often the case that these results do not meet the criterion expressed in Eq. (5) of the main text as

$$e = \frac{1}{\bar{N}} \sum_{n=1}^{\bar{N}} \left[\frac{\int_0^{2\pi} \int_0^1 \left(\bar{\varphi}_n - \varphi_n\right)^2 r \mathrm{d}r \mathrm{d}\theta}{\int_0^{2\pi} \int_0^1 \left(\varphi_n\right)^2 r \mathrm{d}r \mathrm{d}\theta} \right]^{1/2} \leq e_0, \tag{3.A37}$$

To address this, we introduce a perturbation to further refine our solution. We begin by applying a zero-pressure perturbation and perform a nonlinear static equilibrium analysis using an FEM software package (In our case Ansys was used). This analysis yields an updated out-of-plane configuration in conjunction with the smoothened in-plane displacement fields.

To validate the convergence of our solution, the updated configuration and in-plane displacement fields are employed in an eigenvalue modal analysis. By comparing the resulting mode shapes to the experimental mode shapes using the criteria outlined in Eq. (3.A37), we then assess the convergence of our solution. However, if the solution fails to converge, we iterate the process by adjusting the perturbation (perturbing out-of-plane force) until convergence is achieved.

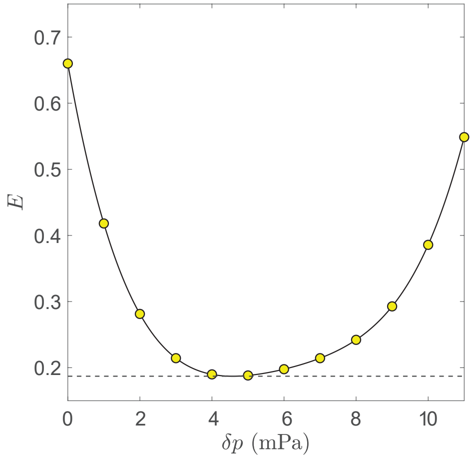

Figure 3.A6: Error criterion e as a function of perturbation uniform transverse load δp.

This iterative procedure ensures that our analysis reaches a stable and accurate solution, capturing the intricate interplay between in-plane and out-of-plane displacements and providing reliable stress distributions in suspended drums.

In the final step of our analysis, after obtaining convergence, we utilize the static displacement fields (in-plane and transverse) to calculate the strain and stress fields within the drum. This calculation is performed using Eqs. (3.A2) and (3.A3) for the mid-plane of the plate. The resulting stress fields serve as a reasonable approximation for the actual experimental stress distributions, as they successfully reproduce the observed mode shapes.

3.A6. FINDING THE MINIMUM ERROR THRESHOLD

The error criterion, as presented in Eq. (3.A37), is formulated based on the spatial disparity between the experimental mode shapes and the reconstructed mode shapes. It is clear that the mode shapes undergo adjustments through the tuning of a transverse perturbation pressure during the post-buckling analysis 3.A5.

To ascertain an appropriate value for e_0, we initiate an iterative procedure without applying any perturbation pressure and gradually increase it. Initially, the observed trend reveals a decreasing error metric e until reaching its minimum value e_0 at a perturbation pressure of δp_m. Beyond this point, further increments in the perturbation pressure result in an increase in error. Consequently, the minimal achievable error for each set of experiments corresponds to e_0, which may vary among different drums. Fig. 3.A6 demonstrates this analysis conducted for device D1. To establish the minimum achievable error threshold using our method, this analysis must be performed for each drum under investigation. The plot clearly indicates the error threshold attained in this case as $e_0 \simeq 0.19$ at $\delta p_m \simeq 4.6\,\text{mPa}$.

The determination of e_0 holds importance in ensuring the accuracy and reliability of

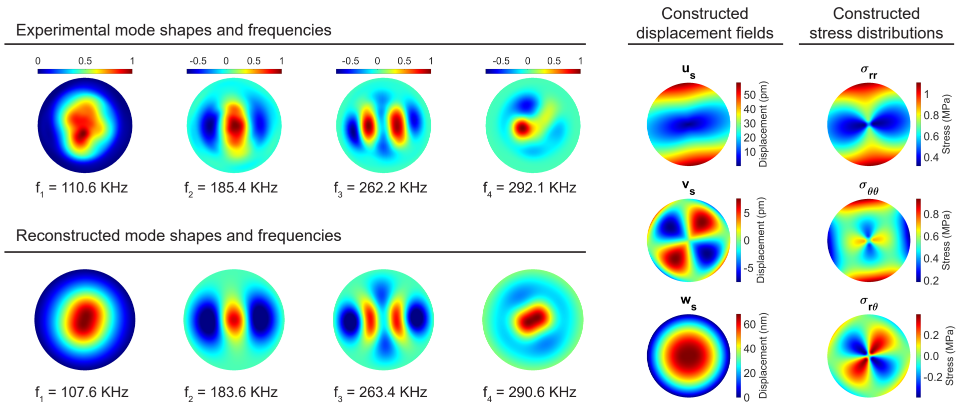

Figure 3.A7: Estimation of stress distributions from experimental mode shapes for device D2.

our method for analyzing the vibrational behavior of circular drums. The specific value of e_0 for each drum is significant as it serves as a reference point for assessing the quality of the reconstructed mode shapes and stress distributions. A lower e_0 signifies a higher level of fidelity in our predictions, thereby greater confidence in the obtained results.

3.A7. STRESS DISTRIBUTION IN THE FABRICATED DEVICES

As shown in the main text, 4 drums' stress distribution were successfully found using the proposed procedure. Here, you can see the experimental mode shapes, reconstructed mode shapes, and also the resulting stress distributions in Fig.s(3.A7-3.A9).

3.A8. RAMAN SPECTROSCOPY MEASUREMENTS AND THEIR LIMITATIONS

The Raman spectra of graphene is related to the strain loaded on the membrane [39], for example, the slope $\partial\omega/\partial\epsilon$ of 2D peak is about -64 $\text{cm}^{-1}/\%$ [39]. Here, we measure the Raman spectrum of the device D1 using 514 nm green laser at room temperature, as shown in Fig. 3.A10 (left). Accordingly, we extract the stress distribution of device D1 as plotted in Fig. 3.A10 (right), which shows an extremely large error bar. This is because of the limited resolution of strain-dependent Raman peak shift. The predicted stress range (difference between the maximum and minimum stress) obtained through Raman measurements is 16 times larger than the range predicted by our method. Additionally, the limited spatial resolution of Raman measurements is evident, with no clear stress distribution observable in the membrane, unlike the distinct distribution obtained through our method, as illustrated in Fig. 3 of the main text. Consequently, our proposed method offers a significantly more accurate approach for quantifying the stress distribution in suspended graphene membranes.

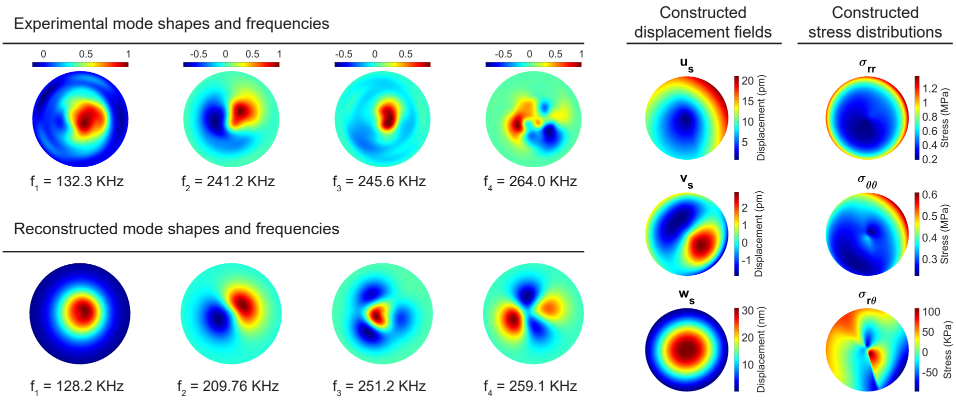

Figure 3.A8: Estimation of stress distributions from experimental mode shapes for device D6.

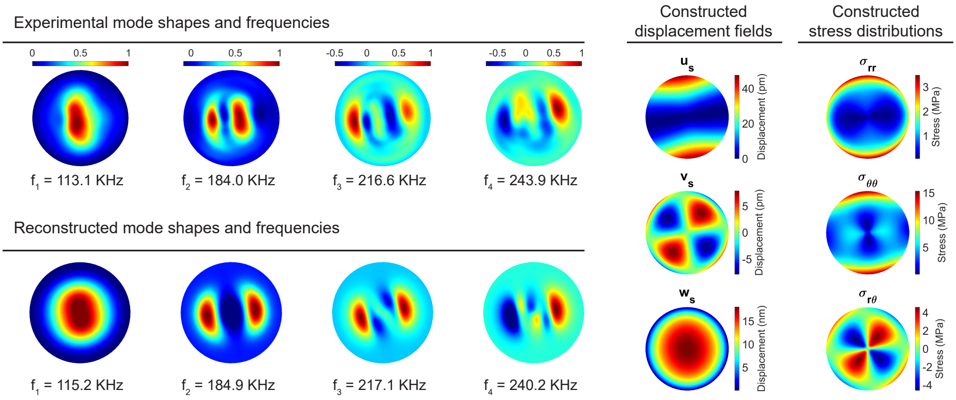

Figure 3.A9: Estimation of stress distributions from experimental mode shapes for device D13.

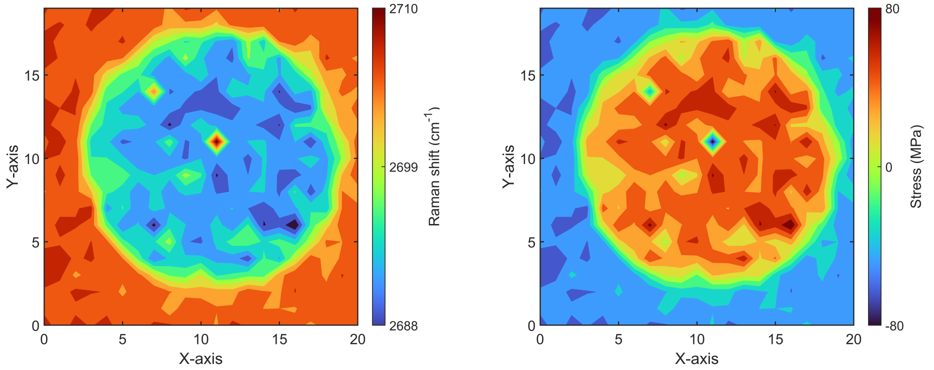

Figure 3.A10: Measured Raman spectra of device D1 and the stress distribution extracted from the reported strain-dependent 2D peak.

3.A9. STRESS DISTRIBUTION IN SMALLER DEVICES

In order to affirm the applicability of our data to smaller devices, we utilized experimental data of a graphene drum with a radius R of 2.5 μm, and thickness h of 5 nm, previously published in [34]. It is noteworthy that due to small out-of-plane static deformations, the method worked without conducting step 3 detailed in Fig. (3.A5). As can be seen in Fig. (3.A11), the stress distribution is found successfully. The stress distribution suggests that this specific device is almost uniformly-tensioned with a part of the edge almost with zero tension suggesting a possible detachment from the substrate. Our observation is consistent with the microscopic image of this graphene drum, provided in [34], that confirms the presence of a detachment at the boundary due to a wrinkle.

3.A10. FABRICATION PROCEDURE

The procedure employed for fabricating the devices of the main text is detailed out here . As shown in Fig. 3.A12(a), the process begins with the preparation of a Si (100) target substrate containing through holes with diameters ranging from 60 μm to 1000 μm. The procedure starts with the deposition of a 6 μm SiO_2 layer on both sides of a 100 mm Si (100) target substrate using plasma-enhanced chemical vapor deposition (CVD). Next, a layer of positive photo-resist is spin-coated onto the substrate, and optical lithography combined with reactive ion etching is employed to define and pattern holes on top of the SiO_2 layer. Deep reactive ion etching (DRIE) is then carried out until reaching the underlying SiO_2 layer. Subsequently, the SiO_2 is thoroughly removed through wet etching in a buffered hydrofluoric acid (BHF) solution (1:7 ratio). The fabrication process is completed with the growth of a 300 nm thermal oxide layer on the wafer using a wet oxidation technique.

In the next step, as shown in Fig. 3.A12(b), multi-layer graphene is deposited using chemical vapor deposition (CVD) on a thin-film Mo catalyst. This process begins with the sputtering of a 50 nm Mo layer onto a 100 mm Si (100) substrate, which is covered by a 600 nm thermal oxide layer [53]. Subsequent CVD is carried out at a substrate temper-

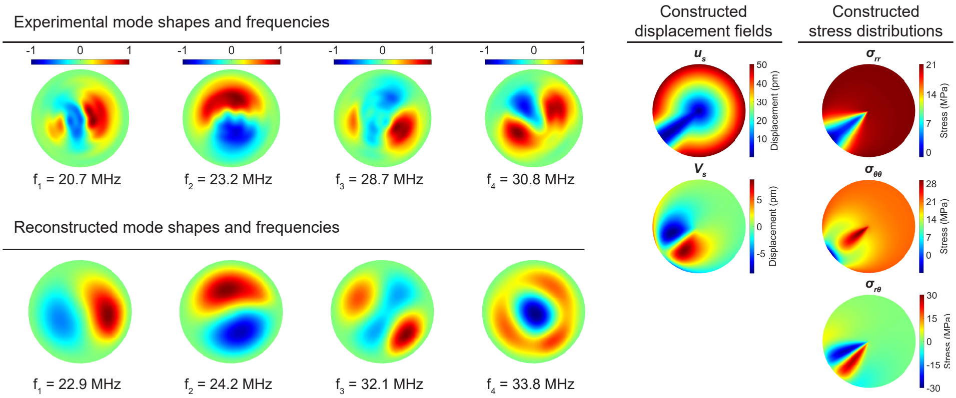

Figure 3.A11: Estimation of stress distributions from experimental mode shapes for graphene membrane presented in [34].

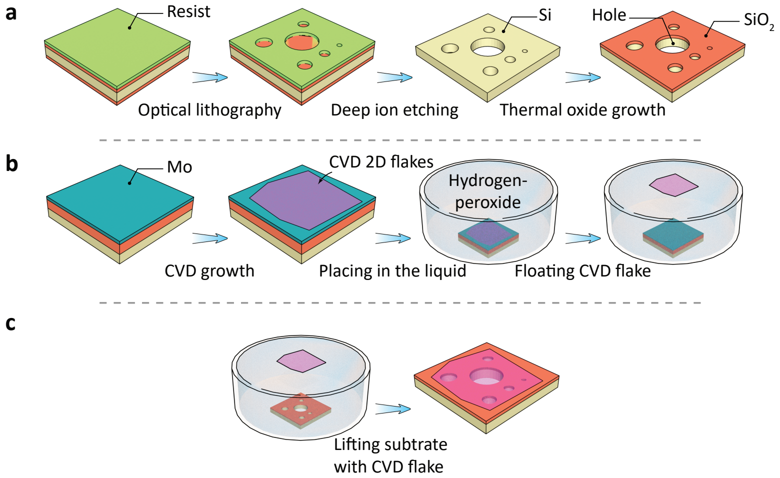

Figure 3.A12: Fabrication and vibration measurement of graphene drums. (a) Fabrication process of SiO$_2$/Si substrate with etched holes. (b) Growth and exfoliation of large-scale CVD graphene flake. (c) Wet transfer method to suspend CVD graphene on substrate.

ature of 915 °C, utilizingH_2/CH_4 gases at flow rates of 1000/25 sccm, respectively, under a pressure of 25 mbar. The growth process is conducted for 30, 45, 60, and 90 minutes for different samples, after which the wafer is cooled down within an argon ambient environment.

The final stage of the fabrication procedure, as depicted in Fig. 3.A12(c), involves transferring the CVD-grown graphene from the growth substrate to the target substrate through a wet transfer process. This step begins by immersing the graphene-coated growth substrate in a 30% hydrogen peroxide solution for 25 minutes, facilitating the detachment of the graphene layer, which then floats atop the hydrogen peroxide solution. Subsequent rinsing with deionized (DI) water is performed twice to ensure complete removal of residual hydrogen peroxide. To optimize the transfer, a detergent solution (1 drop of Triton X100 in 150 ml of DI water) is introduced to reduce surface tension. The graphene layer is then picked up using the target substrate, resulting in the formation of suspended drum structures over the fabricated holes. The samples are subsequently dried at room temperature for 25 minutes and left under a glass enclosure for 24 hours.

3.A11. SAMPLE CHARACTERIZATION AND AFM MEASUREMENTS

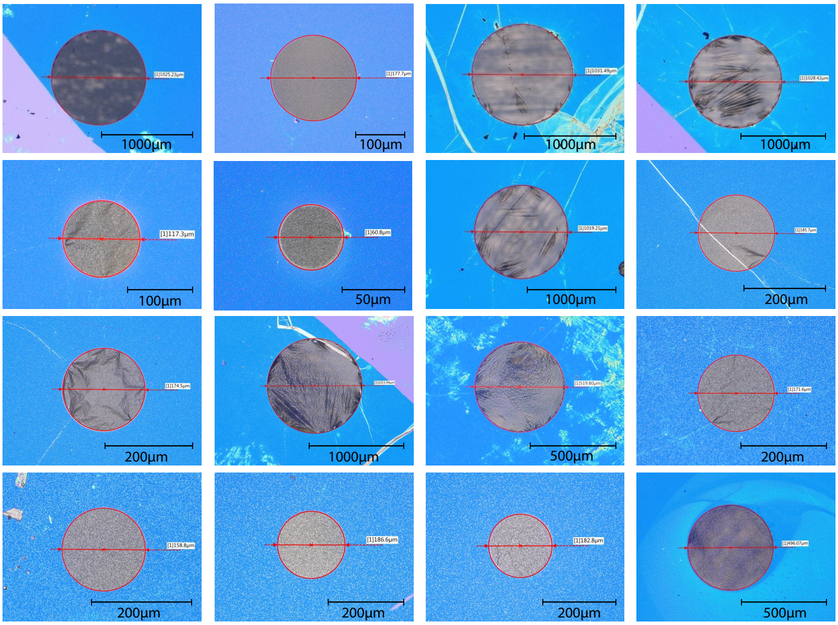

Figure 3.A13: Optical images of the fabricated graphene membranes (devices D1 to D16) on silicon substrate.

Fig. 3.A13 shows all graphene drums we fabricated in this work. Using optical microscopy the image of each drum is obtained and then numbered as devices D1 to D16. The diameters of the fabricated drums vary from 60.8 to 1031.5 μm, as summarized in Table 3.A1. Structural defects such as wrinkles that result from the transfer process can

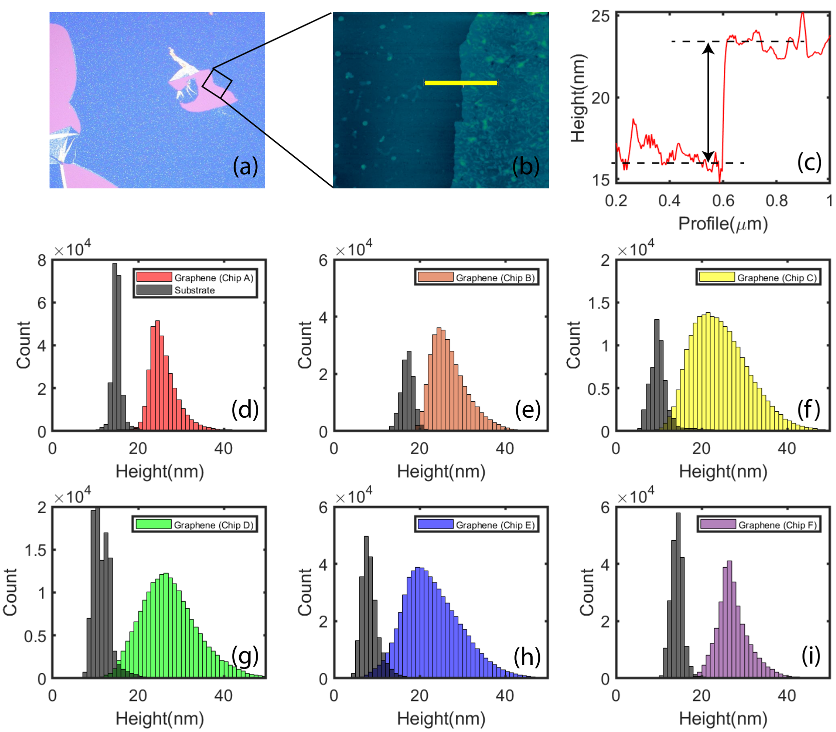

Figure 3.A14: (a) Optical image of the edge of graphene membrane on chip A. (b) AFM image corresponding to the black frame in (a). (c) Height profile along the yellow line shown in (b). (d) Height histogram for both substrate and graphene membrane measured by AFM, allowing us to extract a thickness of around 10 nm. (e)-(i) Height histograms for chip B to F, respectively.

extend over the membranes, causing an irregular distribution of graphene sheet tension around its perimeter. Due to the small thickness and high flexibility of graphene, structural defects can be clearly visible on the defected drums.

Here all devices in Fig.s 3.A13 are fabricated onto 6 Si chips, as numbered from chip A to F (see Table 3.A1). Assuming that the CVD graphene on each chip is uniform, we use AFM to measure the membrane thickness for all devices. We scan the selected edge area of graphene membranes, as shown in the black frame in Fig.s 3.A14(a). The surface height rises from 16.3 to 23.8 nm, corresponding to a membrane thickness of 7.5 nm (Fig.s 3.A14(b) and 3.A14(c)). As shown in Fig. 3.A14(d), for chip A, we use the statistics to plot the height histogram for both substrate (black bars) and membrane (red bars). Accordingly, we extract a thickness of 10 nm, corresponding to a surface mass density about 2.267×10^{-5} kg/m^2. Using this method, we further extract the density of all the other chips as listed in Table 3.A1.

Table 3.A1: Geometrical parameters of suspended graphene samples.

Chip	Thickness(nm)	Drum No.	Diameter(μm)
A	10.0	1	1025.2
		2	177.7
		3	158.0
B	7.0	4	1028.4
		5	1031.5
		6	117.3
		7	60.8
C	11.9	8	1019.2
		9	185.7
D	13.8	10	1011.9
		11	519.8
		12	171.6
		13	158.8
E	11.9	14	186.6
		15	182.8
F	11.9	16	496.1

BIBLIOGRAPHY

[1] Lemme, M.C. et al. Nanoelectromechanical sensors based on suspended 2D materials. Research 2020, 8748602 (2020).

[2] Yildirim, T. et al. Towards future physics and applications via two-dimensional material NEMS resonators. Nanoscale 12, 22366-22385 (2020).

[3] Hu, K.M. et al. Resonant nano-electromechanical systems from 2D materials. EPL 131, 58001 (2020).

[4] Todorovic, D. et al. Multilayer graphene condenser microphone. 2D Mater. 2, 045013 (2015).

[5] Šiškins, M. et al. Magnetic and electronic phase transitions probed by nanomechanical resonators. Nat. Commun. 11, 2698 (2020).

[6] Dolleman, R.J. et al. Optomechanics for thermal characterization of suspended graphene. Phys. Rev. B 96, 165421 (2017).

[7] Liu, H. et al. Tension tuning of sound and heat transport in graphene. Preprint at arXiv:2204.06877 (2022).

[8] Roslon, I.E. et al. Probing nanomotion of single bacteria with graphene drums. Nat. Nanotechnol. 17, 637-642 (2022).

[9] Ferrari, P.F., Kim, S. & van der Zande, A.M., 2023. Nanoelectromechanical systems from two-dimensional materials. Appl. Phys. Rev. 10, 030802 (2023).

[10] Akinwande, D. et al. A review on mechanics and mechanical properties of 2D materials—Graphene and beyond. Extrem. Mech. Lett. 13, 42-77 (2017).

[11] Vozmediano, M.A., Katsnelson, M.I. & Guinea, F., 2010. Gauge fields in graphene. Phys. Rep. 496, 109-148 (2010).

[12] Chen, W. et al. Wrinkling of two-dimensional materials: Methods, properties and applications. Nanoscale Horiz. 4, 291-320 (2019).

[13] Deng, S. & Berry, V., 2016. Wrinkled, rippled and crumpled graphene: an overview of formation mechanism, electronic properties, and applications. Mater. Today 19, 197-212 (2016).

[14] Steeneken, P.G., Dolleman, R.J., Davidovikj, D., Alijani, F. & Van der Zant, H.S., 2021. Dynamics of 2D material membranes. 2D Mater. 8, 042001 (2021).

[15] Gornyi, I.V., Kachorovskii, V.Y. & Mirlin, A.D., 2016. Anomalous Hooke's law in disordered graphene. 2D Mater. 4, 011003 (2016).

[16] Sarafraz, A. et al., 2021. Nonlinear elasticity of wrinkled atomically thin membranes. J. Appl. Phys. 130, 184302 (2021).

[17] Paillet, M., Parret, R., Sauvajol, J.L. & Colomban, P., 2018. Graphene and related 2D materials: An overview of the Raman studies. J. Raman Spectrosc. 49, 8-12 (2018).

[18] Dai, Z., Liu, L. & Zhang, Z.. Strain engineering of 2D materials: issues and opportunities at the interface. Adv. Mater. 31, 1805417 (2019).

[19] Colangelo, F. et al., Mapping the mechanical properties of a graphene drum at the nanoscale. 2D Mater. 6, 025005 (2019).

[20] Ferralis, N., Probing mechanical properties of graphene with Raman spectroscopy. J. Mater. Sci. 45, 5135-5149 (2010).

[21] Eichler, A. et al. Nonlinear damping in mechanical resonators made from carbon nanotubes and graphene. Nat. Nanotechnol. 6, 339-342 (2011).

[22] Bunch, J.S. et al., Impermeable atomic membranes from graphene sheets. Nano Lett. 8, 2458-2462 (2008).

[23] Morell, N. et al., High quality factor mechanical resonators based on WSe2 monolayers. Nano Lett. 16, 5102-5108 (2016).

[24] Houri, S. et al., Direct and parametric synchronization of a graphene self-oscillator. Appl. Phys. Lett. 110, 073103 (2017).

[25] Van Leeuwen, R. et al., Time-domain response of atomically thin MoS2 nanomechanical resonators. Appl. Phys. Lett. 105, 043102 (2014).

[26] Steeneken, P.G. et al., Dynamics of 2D material membranes. 2D Mater. 8, 042001.

[27] Reddy, J.N., Theory and analysis of elastic plates and shells. CRC Press (2006).

[28] Amabili, M., Nonlinear vibrations and stability of shells and plates. Cambridge University Press (2008).

[29] Keşkekler, A. et al. Tuning nonlinear damping in graphene nanoresonators by parametric–direct internal resonance. Nat. Commun. 12, 1099 (2021).

[30] Waitz, R. et al., Spatially resolved measurement of the stress tensor in thin membranes using bending waves. Phys. Rev. Appl. 3, 044002 (2015).

[31] Davidovikj, D. et al., Nonlinear dynamic characterization of two-dimensional materials. Nat. Commun. 8, 1253 (2017).

[32] Sajadi, B. et al., Size-and temperature-dependent bending rigidity of graphene using modal analysis. Carbon 139, 334-341 (2018).

[33] Sajadi, B. et al., Nonlinear dynamic identification of graphene's elastic modulus via reduced order modeling of atomistic simulations. J. Mech. Phys. Solids 122, 161-176 (2019).

[34] Davidovikj, D. et al. Visualizing the motion of graphene nanodrums. Nano Lett. 16, 2768-2773 (2016).

[35] Castellini, P., Martarelli, M. & Tomasini, E.P. Laser Doppler Vibrometry: Development of advanced solutions answering to technology's needs. Mech. Syst. Signal Process. 20, 1265-1285 (2006).

[36] Castellanos-Gomez, A. et al. Single-layer MoS2 mechanical resonators. Preprint at http://arxiv.org/abs/1310.2134 (2013).

[37] Chen, C. et al. Performance of monolayer graphene nanomechanical resonators with electrical readout. Nat. Nanotechnol. 4, 861-867 (2009).

[38] Van der Zande, A.M. et al. Large-scale arrays of single-layer graphene resonators. Nano Lett. 10, 4869-4873 (2010).

[39] Mohiuddin, T.M.G. et al. Uniaxial strain in graphene by Raman spectroscopy: G peak splitting, Grüneisen parameters, and sample orientation. Phys. Rev. B 79, 205433 (2009).

[40] Katsnelson, M.I. & Fasolino, A. Graphene as a prototype crystalline membrane. Acc. Chem. Res. 46, 97-105 (2013).

[41] Amabili, M. Nonlinear vibrations and stability of shells and plates, Cambridge University Press (2008).

[42] Sarafraz, A. et al. Pressure-induced nonlinear resonance frequency changes for extracting Young's modulus of drums. Nonlinear Dyn. 1-11 (2023).

[43] Sajadi, B. et al. Experimental characterization of graphene by electrostatic resonance frequency tuning. J. Appl. Phys. 122, 234302 (2017).

[44] Li, S.R., Yu, W.S. & Batra, R.C. Free vibration of thermally pre/post-buckled circular thin plates embedded with shape memory alloy fibers. J. Therm. Stresses 33, 79-96 (2010).

[45] Changguo, W., Yunliang, L., Xingwen, D., Xiaodong, H. & Guozhi, S. Simulation analysis of vibration characteristics of wrinkled membrane space structure. Int. J. Space Struct. 22, 239-246 (2007).

[46] Neumann, C. et al. Raman spectroscopy as probe of nanometre-scale strain variations in graphene. Nat. Commun. 6, 8429 (2015).

[47] Hiltunen, V.M. et al., Ultrastiff graphene. npj 2D Mater. Appl. 5, 49 (2021).

[48] Liu, H. et al. Enhanced sensitivity and tunability of thermomechanical resonance near the buckling bifurcation. 2D Mater. 11, 025028 (2024).

[49] Kukathasan, S. & Pellegrino, S., 2003. Nonlinear vibration of wrinkled membranes. 44th AIAA/ASME/ASCE/AHS/ASC Structures, Structural Dynamics, and Materials Conference, p. 1747.

[50] Šiškins, M. et al., 2019. Highly anisotropic mechanical and optical properties of 2D layered As2S3 membranes. ACS Nano, 13(9), 10845-10851.

[51] Liu, H., Lee, M., Šiškins, M., Van Der Zant, H. S., Steeneken, P. G., & Verbiest, G. J. Tuning heat transport in graphene by tension. Phys. Rev. B 108, L081401 (2023).

[52] Liu, H. et al. Optomechanical methodology for characterizing the thermal properties of 2D materials. APL Mater. 12, 020901 (2024).

[53] Vasić, B. et al. Low-friction, wear-resistant, and electrically homogeneous multilayer graphene grown by chemical vapor deposition on molybdenum. Appl. Surf. Sci. 509, 144792 (2020).

[54] Shu, C. Differential quadrature and its application in engineering. Springer Science & Business Media (2000).

[55] Shu, C. & Chew, Y.T. Fourier expansion-based differential quadrature and its application to Helmholtz eigenvalue problems. Commun. Numer. Methods Eng. 13, 643-653 (1997).

[56] Wu, T.Y., Wang, Y.Y. & Liu, G.R. Free vibration analysis of circular plates using generalized differential quadrature rule. Comput. Methods Appl. Mech. Eng. 191, 5365-5380 (2002).

[57] Mohiuddin, T. M. G. et al. Uniaxial strain in graphene by Raman spectroscopy: G peak splitting, Grüneisen parameters, and sample orientation. Phys. Rev. B 79, 205433 (2009).

4

4

DYNAMICS OF PRESSURIZED MEMBRANES

The resonance frequency of ultra-thin layered nanomaterials changes nonlinearly with the tension induced by the pressure from the surrounding gas. Although the dynamics of pressurized nanomaterial membranes have been extensively explored, recent experimental observations show significant deviations from analytical predictions. Here, we present a multi-mode continuum model that captures the nonlinear pressure-frequency response of pre-tensioned membranes undergoing large deflections. We validate the model using experiments conducted on polysilicon nanodrums excited opto-thermally and subjected to pressure changes in the surrounding medium. We demonstrate that considering the effect of pressure on the nanodrum tension is not sufficient for determining the resonance frequencies. In fact, it is essential to also account for the change in the membrane's shape in the pressurized configuration, the mid-plane stretching, and the contributions of higher modes to the mode shapes. Finally, we show how the presented high-frequency mechanical characterization method can serve as a fast and contactless method for determining Young's modulus of ultra-thin membranes.

This chapter was published as:
Sarafraz, A., Givois, A., Rosłoń, I., Liu, H., Brahmi, H., Verbiest, G., Steeneken, P.G. and Alijani, F., 2023. Pressure-induced nonlinear resonance frequency changes for extracting Young's modulus of nanodrums. *Nonlinear Dynamics,* pp.1-11.

4.1. INTRODUCTION

Owing to their low bulk modulus and outstanding in-plane stiffness, sensors made of ultra-thin membranes and two-dimensional (2D) materials have recently gained interest for gas [1, 2], pressure [3–5], and biosensing [6] applications. Despite numerous experimental and theoretical studies [7, 8], probing the elasticity of these membranes has remained challenging [9, 10], making the development of new methods for their mechanical characterization of great importance [11–13].

Atomic force microscopy (AFM) is the most widely used technique for extracting Young's modulus of 2D membranes, which is achieved by fitting their nonlinear force-deflection response [14, 15]. Pressurized blister test [16, 17], electrostatic deflection method [18–20], and Duffing-type nonlinear response at large amplitude vibrations [11, 13] are other methods used to characterize thin membranes.

Recently, it was also shown that the tension-induced shift in the resonance frequency of 2D membranes as a function of applied pressure could be used to characterize elastic properties. [21]. In contrast to AFM which requires large indentations to enter the nonlinear regime for estimating Young's modulus [22], it was demonstrated that the geometrically nonlinear regime may be easily reached using this approach by sweeping the pressure across the membrane. However, it was found that the fit of the pressure-frequency response, results in estimations of Young's modulus that are an order of magnitude lower than the well-accepted values in the literature [21, 23]. Therefore, in order to use this method to characterize suspended ultra-thin materials that undergo large deflections, a more comprehensive model is required to describe the underlying physics.

Unlike models commonly used for characterizing pressurized nanodrums [24, 25], the proposed model accounts for a change in the static equilibrium shape of the vibrating membrane, mid-plane stretching, and in-plane and out-of-plane mode coupling. By comparing the model to the Finite Element Method (FEM) simulations of nanodrums subjected to large deflections, we validate the analytic formulation. Finally, we acquire the nonlinear pressure-frequency response of polysilicon nanodrums experimentally and demonstrate that the suggested multi-mode model can be utilized to characterize (extract Young's modulus) from the high-frequency dynamic response of pressurized ultra-thin membranes.

4.2. THEORY

4.2.1. GOVERNING EQUATIONS

We consider a thin circular drum with a diameter of $2R$ and thickness $h \ll R$ clamped at the outer edge, as shown in figure 4.1(a). The drum is assumed to be made of a homogeneous and isotropic material of density ρ, Young's modulus E, and Poisson's ratio ν. The drum is also assumed to be subjected to an axisymmetric tension n_0, and the pressure difference alongside it is Δp (see figure 4.1(b, c)). We only account for axisymmetric vibrations and suppose that the aspect ratio is very small (i.e., $h/R < 0.001$ [26]) such that the effect of bending rigidity can be discarded, and the motion can be modeled using membrane theory [27]. The equations of motion for a membrane subjected to large transverse displacement w, moderate rotations, are the dynamic equivalents of the von Kármán equations. In this context, the governing equations of a pre-stressed membrane with negligible bending rigidity are [27]:

$$\rho h \ddot{w} - n_0 \nabla^2 w - \operatorname{div}(\boldsymbol{N} \nabla w) = \Delta p, \tag{4.1a}$$

$$\rho h \ddot{\boldsymbol{u}} - \mathbf{div}\, \boldsymbol{N} = 0. \tag{4.1b}$$

where:

$$\begin{aligned} \boldsymbol{N} &= [Eh/(1-\nu^2)]\,[(1-\nu)\boldsymbol{\epsilon} + \nu\, \mathrm{tr}\, \boldsymbol{\epsilon} \mathbf{1}], \\ \boldsymbol{\epsilon} &= \tfrac{1}{2}\left(\nabla \boldsymbol{u} + \nabla^{\mathrm{T}} \boldsymbol{u} + \nabla w \otimes \nabla w\right). \end{aligned} \tag{4.2}$$

Here, $\boldsymbol{u} = [u; v]$ is the axial displacements; moreover, $\nabla^2 w$, ∇w and $\nabla \boldsymbol{u}$ denote the Laplacian of scalar field w, the vector gradient of scalar field w and the tensor gradient of the vector field $\boldsymbol{u}$, respectively. $\operatorname{div}\boldsymbol{u}$ and $\mathbf{div}\, \boldsymbol{N}$ are the scalar and vector divergences of vector field $\boldsymbol{u}$ and tensor field $\boldsymbol{N}$. Finally, $\nabla w \otimes \nabla w$ corresponds to the tensor product between vectors ∇w and ∇w. Overdot indicates derivation with respect to time. Considering only axisymmetric vibrations the following set of equations can be obtained in cylindrical coordinates and in terms of radial (u) and transverse (w) displacements:

$$\begin{aligned} \rho h \ddot{w} - n_0 \Delta w - \left(Eh/\left(1-\nu^2\right)\right) [u_{,rr} w_{,r} + u_{,r} w_{,rr} \\ +(1+\nu) \tfrac{u_{,r}}{r} w_{,r} + \nu \tfrac{u}{r} w_{,rr} + \tfrac{(w_{,r})^3}{2r} + \tfrac{3}{2} (w_{,r})^2 w_{,rr}] = \Delta p, \end{aligned} \tag{4.3a}$$

$$\left(Eh/\left(1-\nu^2\right)\right) [u_{,rr} + \frac{u_{,r}}{r} - \frac{u}{r^2} + \frac{1-\nu}{2} \frac{(w_{,r})^2}{r} + w_{,r} w_{,rr}] = 0, \tag{4.3b}$$

where $_{,r}$ and $_{,rr}$ denote the first and second derivatives with respect to r.

To write Eqs. (4.3a, b) in dimensionless form, we introduce the following set of dimensionless variables:

$$\begin{aligned} &\bar{w} = \tfrac{w}{h}, \quad \bar{u} = \tfrac{R}{h^2} u, \quad \bar{r} = \tfrac{r}{R}, \\ &\bar{t} = \tfrac{1}{R} \sqrt{\tfrac{n_0}{\rho h}}\, t, \quad \overline{\Delta p} = \tfrac{R^2}{n_0 h} \Delta p, \quad \varepsilon = \tfrac{1}{1-\nu^2} \tfrac{E h^3}{n_0 R^2}, \end{aligned} \tag{4.4}$$

This would yield the following non-dimensional form of equation (4.3):

$$\begin{aligned} \ddot{\bar{w}} - \Delta \bar{w} - \varepsilon \Bigg[\bar{u}_{,rr} \bar{w}_{,r} + (1+\nu) \tfrac{\bar{u}_{,r}}{r} \bar{w}_{,r} + \nu \tfrac{\bar{u}}{r} \bar{w}_{,rr} \\ + \tfrac{(\bar{w}_{,r})^3}{2r} + \tfrac{3}{2} \left(\bar{w}_{,r}\right)^2 \bar{w}_{,rr} \Bigg] = \overline{\Delta p} \end{aligned} \tag{4.5a}$$

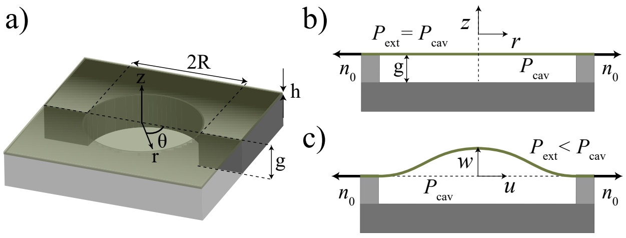

Figure 4.1: a) Schematic of the membrane and its cross-sections. b) Side-view of the undeformed membrane, and c) deformed configuration under transverse loading due to pressure difference alongside the membrane.

$$\bar{u}_{,rr} + \frac{\bar{u}_{,r}}{r} - \frac{\bar{u}}{r^2} + \frac{1-\nu}{2}\frac{\left(\bar{w}_{,r}\right)^2}{r} + \bar{w}_{,r}\bar{w}_{,rr} = 0. \tag{4.5b}$$

In order to solve Eqs. (4.5a, b), we first expand the transverse displacement w and radial displacement u as follows:

$$\bar{w}(r,t) = \sum_{k=1}^{N_w} \Phi_k(r)\, q_k(t), \tag{4.6a}$$

$$\bar{u}(r,t) = \sum_{p=1}^{N_u} \Psi_p(r)\, \eta_p(t), \tag{4.6b}$$

where q_k and η_p denote the unknown modal coordinates, and N_w and N_u are the number of generalized coordinates that will be retained in the analysis. Moreover, Φ_k and Ψ_p are mode shapes associated with the transverse and radial displacements, respectively. These modes are chosen such that they satisfy the following eigenvalue problems that originate from the linear counterpart of Eqs. (4.5):

$$\Delta\Phi_k + \omega_k^2\Phi_k = 0, \qquad \Psi_{,rr} + \frac{\Psi_{,r}}{r} - \frac{\Psi}{r^2} + \gamma_p^2\Psi_p = 0 \tag{4.7}$$

with ω_k and γ_p being the transverse and in-plane dimensionless eigenfrequencies, respectively. We note that Eqs. (4.7) are Bessel equations, and their solution can be expressed as:

$$\Phi_k(r) = \kappa_k J_0(\omega_k r), \qquad \Psi_p(r) = \lambda_p J_1(\gamma_p r). \tag{4.8}$$

These modes have orthogonality properties and are normalized with respect to the modal mass, by fixing the values of κ_k, λ_p introduced in Eqs. (4.8) and (4.7). They are chosen such that:

$$\iint_S \Phi_i\Phi_j \mathrm{d}S = \delta_{ij} \qquad \text{and} \qquad \iint_S \Psi_p\Psi_l \mathrm{d}S = \delta_{pl}. \tag{4.9}$$

where S is the domain of integration. By applying Galerkin technique, namely inserting Eqs. (4.8), and Eqs. (4.6) in Eqs. (4.5), multiplying equation (4.5a) by Φ_k and equation (4.5b) by Ψ_p, and then integrating over the entire domain, the nonlinear partial differential Eqs. (4.5a) and (4.5b) reduce to:

$$\ddot{q}_k + \omega_k^2 q_k + \varepsilon\sum_{p=1}^{N_u}\sum_{i=1}^{N_w} a_{pi}^k \eta_p q_i + \varepsilon\sum_{i=1}^{N_w}\sum_{j=1}^{N_w}\sum_{l=1}^{N_w} c_{ijl}^k q_i q_j q_l = Q_k \tag{4.10a}$$

$$\gamma_p^2\eta_p - \sum_{i=1}^{N_w}\sum_{j=1}^{N_w} b_{ij}^p q_i q_j = 0 \tag{4.10b}$$

where $Q_k = \overline{\Delta p}\left[\int_0^1 \Phi_k^2 r \mathrm{d}r\right]^{-1}\left[\int_0^1 \Phi_k r \mathrm{d}r\right]$ is the projection of $\overline{\Delta p}$ on the k-th mode of vibration, and the nonlinear modal coefficients a_{pi}^k, b_{ij}^p, and c_{ijl}^k are:

$$\begin{aligned} a_{pi}^k = &-[\textstyle\int_0^1 \Phi_k^2 r \mathrm{d}r]^{-1} \int_0^1 \Phi_k(\Psi_{p,rr}\Phi_{i,r} + \Psi_{p,r}\Phi_{i,rr} + (1+\nu)\frac{\Psi_{p,r}\Phi_{i,r}}{r} \\ &+\nu\frac{\Psi_p\Phi_{i,rr}}{r}) r \mathrm{d}r, \end{aligned} \tag{4.11a}$$

$$b^p_{ij} = +\frac{1}{2}[\int_0^1 \Psi_p^2 r\mathrm{d}r]^{-1} \int_0^1 \Psi_p(\frac{1-\nu}{r}\Phi_{i,r}\Phi_{j,r} + (\Phi_{i,r}\Phi_{j,r})_{,r}) r\mathrm{d}r, \tag{4.11b}$$

$$c^k_{ijl} = -\frac{1}{2}[\int_0^1 \Phi_k^2 r\mathrm{d}r]^{-1} \int_0^1 \Phi_k(\Phi_{i,r}\Phi_{j,r}\Phi_{l,r} + \frac{(\Phi_{i,r}\Phi_{j,r}\Phi_{l,r})_{,r}}{r}) r\mathrm{d}r. \tag{4.11c}$$

In order to find η_p in terms of q_k, we rewrite equation (4.10b) as:

$$\eta_p = \frac{1}{\gamma_p^2}\sum_{i=1}^{N_w}\sum_{j=1}^{N_w} b^p_{ij} q_i q_j. \tag{4.12}$$

Inserting equation (4.12) in equation (4.10a) [28] leads to:

$$\ddot{q}_k + \omega_k^2 q_k + \varepsilon\sum_{i=1}^{N_w}\sum_{j=1}^{N_w}\sum_{l=1}^{N_w}\Gamma^k_{ijl} q_i q_j q_l = Q_k, \tag{4.13}$$

with

$$\Gamma^k_{ijl} = c^k_{ijl} + \sum_{p=1}^{N_u}\frac{b^p_{jl} a^k_{pi}}{\gamma_p^2}. \tag{4.14}$$

equation (4.13) is a reduced-order model, which accounts for mid-plane stretching and higher-mode interactions and can be used for investigating nonlinear pressure-frequency response of nanodrums.

4.2.2. SOLUTION PROCEDURE

Generally, the force vector applied on a membrane can be split into a constant, and a time-varying part. The constant force leads to a static deflection, and the time-varying force vibrates the structure around the new configuration. Considering small-amplitude oscillations around large pressure-induced deflections, it is a decent approximation to separate the contribution into static (q_k^s) and dynamic (q_k^d) components as follows [12]:

$$q_k = q_k^s + q_k^d. \tag{4.15}$$

This separation (equation (4.15)) allows us to separate equation (4.13) to a static and dynamic part as well. We can obtain the static deflection due to Q_k, and obtain the dynamic equations around the statically deflected configuration which we will then use for obtaining the natural frequencies of the nanodrum in the deformed state and as a function of the applied pressure, as follows:

$$\omega_k^2 q_k^s + \varepsilon\sum_{i=1}^{N_w}\sum_{j=1}^{N_w}\sum_{l=1}^{N_w}\Gamma^k_{ijl} q_i^s q_j^s q_l^s = Q_k, \tag{4.16a}$$

$$\ddot{q}_k^d + \omega_k^2 q_k^d + \varepsilon\sum_{i=1}^{N_w}\alpha_i^k q_i^d = 0, \tag{4.16b}$$

where

$$\alpha_i^k = \sum_{j=1}^{N_w}\sum_{l=1}^{N_w}(2\Gamma^k_{jil} + \Gamma^k_{ijl}) q_j^s q_l^s. \tag{4.17}$$

In order to solve equation (4.16a) for q_k^s, we use the software package MANLAB. The software uses the Asymptotic Numerical Method (ANM) [29], a continuation algorithm based on high-order Taylor series expansions, to solve nonlinear systems of equations. The ANM continuation method allows for solving nonlinear algebraic equations written in the form:

$$\boldsymbol{F}(\boldsymbol{U},\lambda)=\boldsymbol{0}, \tag{4.18}$$

where $\boldsymbol{F}$ denotes a set of nonlinear algebraic equations, $\boldsymbol{U}=[q_1^s, q_2^s, \dots, q_{N_w}^s]$ is a vector of unknown coefficients, and λ is the continuation parameter. The method also requires the system of equations to be written with quadratic nonlinearities [29]. To perform continuation, we thus recast the static part of equation (4.16a) to:

$$\omega_k^2 q_k^s + \varepsilon \sum_{i=1}^{N_w}\sum_{j=1}^{N_w}\sum_{l=1}^{N_w}\Gamma_{ijl}^k S_{jl} q_i^s - \lambda Q_k = 0, \tag{4.19a}$$

$$S_{jl} - q_j^s q_l^s = 0. \tag{4.19b}$$

By solving equation (4.19) for q_k^s, one can find the shift in resonance frequencies due to pressure. We note that the fundamental frequency of the pressurized nanodrum Ω_u can be obtained by considering the pre-factors of q_k^d in equation (4.16b) which is denoted with the matrix $\boldsymbol{A}$, defined as:

$$A_{uv} = \omega_u^2 \delta_{uv} + \varepsilon \alpha_u^v. \tag{4.20}$$

where δ_{uv} is the kronecker delta. Diagonalizing the matrix $\boldsymbol{A}$ leads to the modified frequencies and mode shapes of the bulged nanodrum with an initial bulged shape:

$$[\Omega_u^2 \delta_{uv}]_{u,v\in[1,N_w]} = \boldsymbol{P}^{-1}\boldsymbol{A}\boldsymbol{P}, \tag{4.21}$$

where $\boldsymbol{P}$ are the eigenvectors associated with the frequencies Ω_u for the pressurized membrane.

4.3. RESULTS

4.3.1. NUMERICAL SIMULATIONS

CONVERGENCE STUDY

As mentioned in the Section 4.2, in order to better capture small-amplitude oscillations of a pressurized membrane, one must i) linearize the dynamic response around the new static configuration, ii) account for mid-plane stretching effect, and iii) includes contributions from out-of-plane modes. Thus, to emphasize the significance of these assumptions and to facilitate a more accurate comparison of these parameters in a pressurized configuration versus a flat configuration, in Figs. 4.2, we simulate the effect of pressure on the static and dynamic in-plane and out-of-plane displacements of a nanodrum with $R = 5\ \mu$m, $h = 20$ nm, $\rho = 2300$ kg. m^{-3}, $E = 160$ GPa, $\nu = 0.22$, $n_0 = 0.3$ N/m.

figure 4.2(a) shows that the original flat configuration changes significantly with increasing pressure. This result suggests that when estimating frequency shifts due to pressure, the dynamic governing equation must be obtained around the new bulged shape ($q_k^s \neq 0$) rather than the flat configuration ($q_k^s = 0$). The application of pressure causes

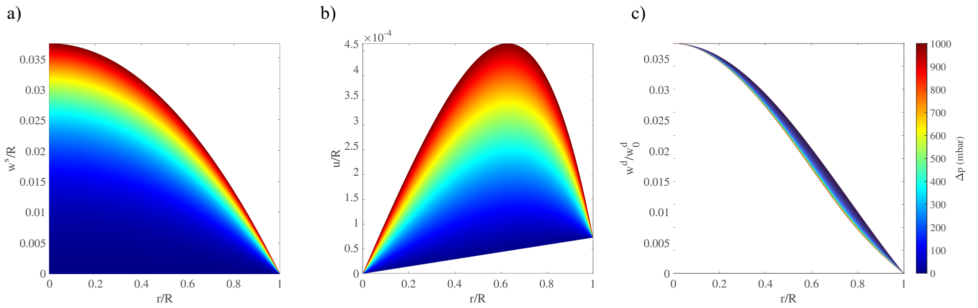

Figure 4.2: Variation of the static and dynamic displacement fields with pressure. a) Normalized static transverse displacement varying from a flat to a nearly parabolic configuration; b) normalized in-plane displacement showing deviation from linear variation in the radial direction with increasing pressure; c) normalized mode shape as a function of external pressure obtained from the multi-mode model (w_0^d denotes the dynamic transverse deflection at the center of the membrane). One must bear in mind that the membrane is flat at $\Delta p = 0$ mbar.

a nonlinear in-plane displacement field at high pressures, as depicted in figure 4.2(b). In addition, figure 4.2(c) illustrates the slight differences in the first mode shape that emerge due to statically deformed configurations. As we will discuss next, neglecting these effects could yield wrong estimation of the resonance frequencies of pressurized ultra-thin membranes.

We also note that the model is obtained in modal coordinates. Nonetheless, the governing partial differential equations (equation (4.3)) were formulated with in-plane (u) and out-of-plane (w) displacement fields. Moreover, figure 4.2 depicts the results for u, w^s, and w^d, rather than q^s, and q^d. Thus, to retrieve u from the modal equations, one must use Eqs. (4.4), (4.6b), and (4.12) simultaneously as follows:

$$u(r,t) = \frac{h^2}{R}\sum_{p=1}^{N_u}\sum_{i=1}^{N_w}\sum_{j=1}^{N_w}\Psi_p(r)\,\frac{b_{ij}^p}{\gamma_p^2}\,q_i^s q_j^s. \tag{4.22}$$

However, for the out-of-plane deflection, one should note that separation of static and dynamic modal coordinates results in the separation of static and dynamic transverse displacements. Using Eqs. (4.15), (4.6a) and (4.4), the transverse displacement can be then obtained as follows:

$$w = w^s + w^d, \tag{4.23}$$

where:

$$w^s = h\sum_{k=1}^{N_w}\Phi_k(r)\,q_k^s, \tag{4.24a}$$

$$w^d = h\sum_{k=1}^{N_w}\Phi_k(r)\,q_k^d. \tag{4.24b}$$

In order to highlight the influence of the effects depicted in figure 4.2 on the estimation of the resonance frequencies, we benchmark in figure 4.3(a-c) the fundamen-

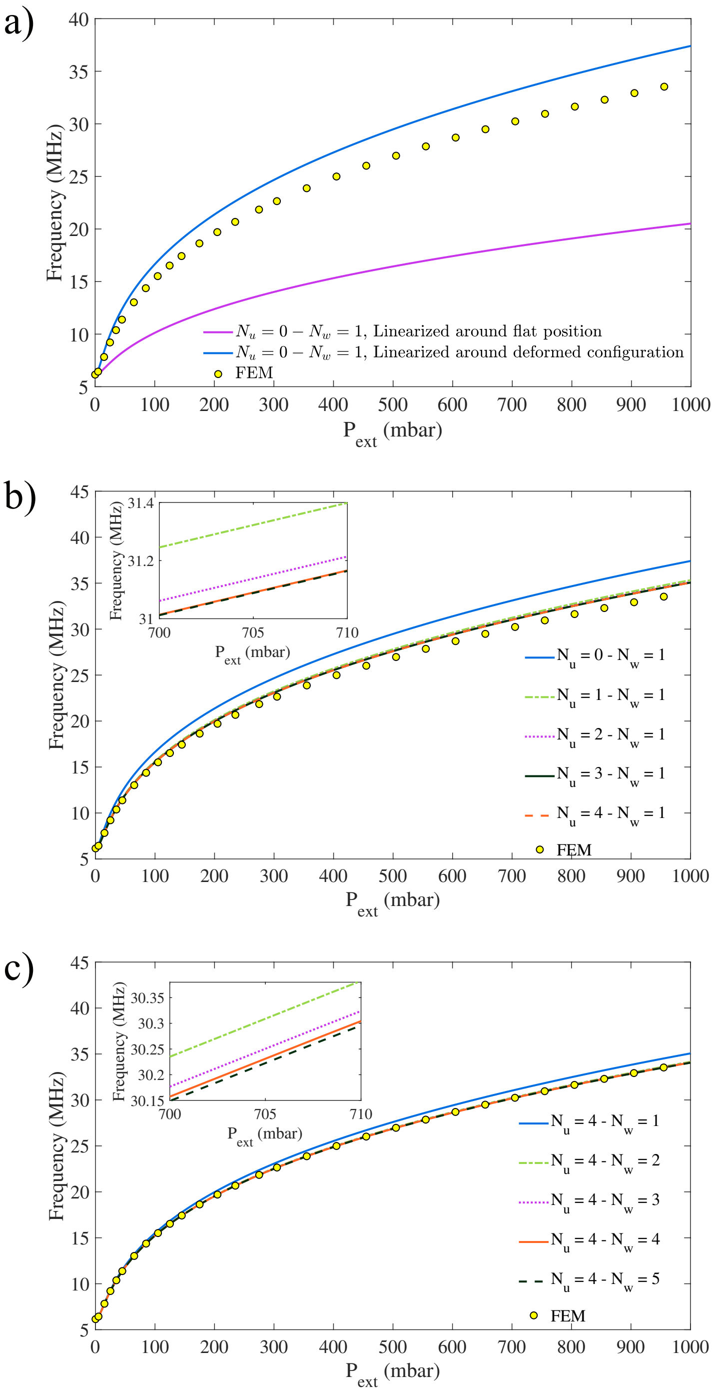

Figure 4.3: Comparison of the proposed model to the FEM result by a) linearizing the dynamic governing equation about the deformed static configuration rather than flat position; b) increasing the number of in-plane modes; c) addition of out-of-plane modes.

tal frequency derived from our model against FEM results. The simulations are performed for the same drum specifications as figure 4.2. In figure 4.3(a), we simulate the frequency shift where only one single out-of-plane mode is retained in the analysis ($N_u = 0, N_w = 1$). Frequency shifts are found, by linearizing equation (4.16b) around the undeformed (flat) as well as deformed configuration. The figure confirms our earlier prediction in figure 4.2(a) that using the equations around the deformed configuration substantially increases accuracy. When compared to FEM results, the model still has a maximum error of 9% at 1 bar.

To illustrate the effect of in-plane displacements on the predicted frequencies, we increase N_u from 0 to 4 in figure 4.3(b) while retaining only one out-of-plane generalized coordinate ($N_w = 1$) in the analysis. It can be seen that including more in-plane modes in the model results in a more accurate model (the error relative to FEM simulations decreases to 4% at 1 bar). This confirms the important role of mid-plane stretching when tracing the fundamental resonance frequency of nanodrums as a function of pressure.

Although the response from this model is already close to the FEM simulations, figure 4.3(c) shows that the accuracy can be even further improved by including more transverse degrees-of-freedom in the basis functions by increasing N_w in Eqs. (4.16). This finally leads to a negligible difference between simulations based on the present multi-mode model and FEM results, which highlights a slight contribution of higher order out-of-plane modes to the estimated resonance frequency [30]. Notably, each of these three criteria contributes to model convergence, and neglecting them would reduce the accuracy the model. For instance, considering more out-of-plane displacements while ignoring in-plane displacements would not produce accurate results, as in-plane displacements are always required to account for the mid-plane stretching effect.

SINGLE-TRANSVERSE-MODE APPROXIMATION

Although increasing the number of transverse modes improves model accuracy, it also increases the complexity of the governing equations, necessitating the employment of numerical techniques to solve them. However, the model can be analytically solved using just one transverse mode. Figure 4.3 demonstrates that the single-transverse-mode approximation is precise enough for tracing the pressure induced resonance frequency shifts up to 1 bar. Considering only $N_w = 1$ and $N_u = 4$, and converting equations back to dimensional form using equation (4.4) yields the following equations as a simplified version of Eqs.(4.16):

$$\frac{5.7831 n_0}{\rho h R^2}\tilde{q}_1^s + 1.181\frac{E\varpi(\nu)}{\rho R^4}\left(\tilde{q}_1^s\right)^3 = \frac{1.6019}{\rho h}\Delta p, \tag{4.25a}$$

$$\ddot{\tilde{q}}_1^d + \frac{5.7831 n_0}{\rho h R^2}\tilde{q}_1^d + 3.543\frac{E\varpi(\nu)}{\rho R^4}\left(\tilde{q}_1^s\right)^2\tilde{q}_1^d = 0, \tag{4.25b}$$

where $\varpi(\nu)$ is plotted in figure (4.4). Moreover, $\tilde{q}_1^s = hq_1^s$ denotes dimensional static deflection at the center of the nanodrum and $\tilde{q}_1^d = hq_1^d$ is the dimensional dynamic deflection at the center of the membrane. For this simplified scenario, the nonlinear pressure-deflection and pressure-frequency relationships are derived analytically by linearizing equation(4.25) around the deflected configuration as follows:

$$\Delta p = A\frac{n_0}{R^2}\tilde{q}_1^s + B\frac{Eh}{R^4}\left(\tilde{q}_1^s\right)^3, \tag{4.26a}$$

$$f = \frac{2.4048}{2\pi R}\sqrt{\frac{n_0}{\rho h} + C\frac{E}{\rho R^2}\left(\tilde{q}_1^s\right)^2}, \tag{4.26b}$$

where A, B, and C are defined for the current study in table (4.1). It is worth noting that equation (4.26a) only retains the cubic term in the high pressure regime, hence $\Delta p \propto \left(\tilde{q}_1^s\right)^3$. By applying the same reasoning, it is possible to demonstrate that equation (4.26b) results in $f \propto \left(\tilde{q}_1^s\right)$ and thus $f \propto \Delta p^{1/3}$.

We finally compare the result of our reduced-order model (equation (4.26)) with analytic models available in the literature, which are often used for the dynamic characterization of pressurized nanodrums [24, 25] (see figure 4.5).

In table (4.1) we benchmark this new formulation against the analytic solutions available in the literature for pressurized nanodrums [24, 25]. Significant discrepancies between our model and those of Refs. [24, 25] can be attributed to the simplifying assumptions lifted in our study, including linearization about flat configuration, absence of mid-plane stretching, and out-of-plane modal interactions. As demonstrated in figure 4.3, the first two assumptions have a greater impact on the model's accuracy than the third one.

4.3.2. EXPERIMENTAL VALIDATION

To verify the applicability of the proposed formulation for the dynamic characterization of ultra-thin drums, we measure 33 nm thick polysilicon membranes measured by Atomic Force Microscopy (AFM), which we transfer over SiO2 substrate cavities, that are created using reactive ion etching with a depth of 350 nm. The 10 μm-diameter drums are placed in a vacuum chamber with variable pressure ranging from 50 to 1000 mbar. We employ a modulated blue laser diode (λ = 405 nm) to push the polysilicon nanodrums into resonance (figure 4.6a). The suspended nanodrum modulates the intensity of the reflected red laser (λ = 633 nm), which is collected at a photodiode and analyzed by a Vector Network Analyser (VNA). Our setup includes a PID controller that monitors chamber pressure using a vacuum pump and gas supply (nitrogen). figure 4.6(b) depicts the frequency spectra of a polysilicon drum at different pressures $\Delta P = P_{\text{ext}} - P_{\text{cav}}$, where P_{cav} and P_{ext} are the pressure outside and inside the cavity, respectively (see figure 4.1).

Table 4.1: Benchmarking the present model's parameters against the analytic formulations available in the literature (See equation 4.26).

Model	A	B	C
Ref. [24]	4	$\frac{8}{3(1-\nu)}$	$\frac{2}{3\,(1-\nu)}$
Ref. [25]	4	$\frac{8}{3(1.026-0.793\nu-0.233\nu^2)}$	$\frac{2}{3\left(1-\nu^2\right)}$
Current Study	3.61	$0.737\varpi(\nu)$	$0.612\varpi(\nu)$

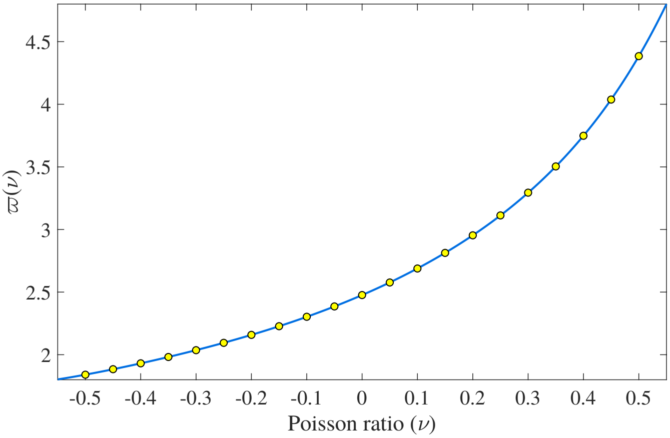

Figure 4.4: Function $\varpi(\nu)$ used in single-transverse-mode analysis (see Eqs. (4.26)). The function is evaluated for finite numbers of Poisson ratios and interpolated with the cubic spline method.

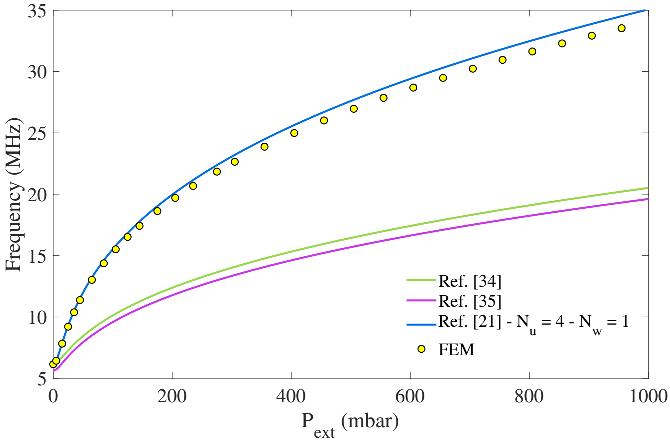

Figure 4.5: Comparison of models available in the literaure and single-mode approximation proposed in Eqs. (4.26).

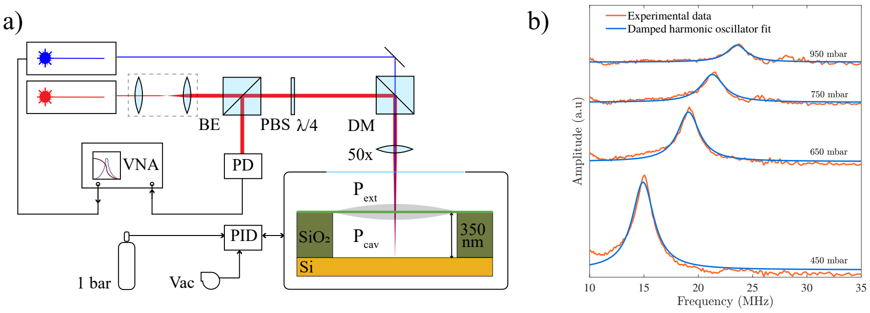

Figure 4.6: The laser interferometry setup and obtained frequency spectra of polysilicon drums. a) After passing through the polarized beam splitter (PBS) and the quarter-wave plate ($\lambda/4$), the red laser is combined with the blue laser and focused on the drum using a dichroic mirror (DM). The readout is performed by a high-frequency photodiode (PD), and the output is fed into the Vector Network Analyzer (VNA). The VNA modulates the blue laser that actuates the drum. A PID controller is used to regulate gas pressure inside the vacuum chamber. b) Frequency spectra (light green) are obtained from the VNA at different pressures. To determine the fundamental mode's resonance frequency, a damped harmonic oscillator model is fitted (dark green).

As a result of increased pressure, we observe an apparent tension-induced increase in the nanodrum's resonance frequency. To obtain the pressure-frequency response, we sweep the pressure from 50 to 1000 mbar and fit the resonance peaks with the damped linear harmonic oscillator model to obtain resonance frequencies at each pressure values (See figure 4.6(b)). In figure 4.7(a) we show typical pressure-frequency measurement data which we fit using our model (E = 155 GPa, $n_0 = 1.6$ N/m). In contrast to figure 4.3, we see a minimum in the pressure-frequency response at $P_{\text{cav}} = 248$ mbar, which corresponds to a flat configuration. In this configuration, the drum's fundamental frequency is determined solely by pre-tension. By increasing pressure, the nanodrum deforms statically, and the resonance frequency varies nonlinearly as $f \propto \sqrt[6]{E}\Delta p^{1/3}$. Knowing this relation, such pressure-frequency measurements can also be used to determine the nanodrum's Young's modulus.

To demonstrate the versatility of the method for characterizing Young's modulus of ultra-thin membranes, we repeated the same measurements on 13 nanodrums that were adequately sealed (or the leak rate was low enough relative to the experiment's data collection speed) and did not exhibit hysteresis in the pressure-frequency response when the pressure was swept up and down. From these measurements, we determined $n_0 = 1.1 \pm 0.5\,\text{N/m}$ for the nanodrums. Figure 4.7(b) depicts the retrieved Young's moduli histogram. We see that the obtained average value $E = 148 \pm 7\,\text{GPa}$ from our technique is comparable to the literature-reported uni-axial stretching test findings for thin polysilicon beams [31, 32], further validating the accuracy of our model. We note that in our experiments, owing to the low aspect ratio of the fabricated devices, the bending rigidity is very small. The linear stiffness mediated by bending rigidity is proportional to $k_{bending} = Eh^3/(12(1-\nu^2)R^2) = 0.02$ N/m which compared to the linear stiffness due to the pre-tension of the nanodrum ($k_{stretching} = n_0 = 1.1$ N/m) in the flat configuration is negligible. Therefore, consistent with our modelling approach, the motion of the nanodrum is dominated by its tension. One can find more information for how to compute and compare such results in [33, 34].

At high pressures, the damping also rises, which may make it difficult to observe resonance peaks. Yet, our experiments demonstrate that even at ambient pressure the oscillation is under-damped and the resonance peak is apparent. In addition, as depicted in figure 4.7a, the membranes reach the nonlinear regime at $\Delta p \approx 400$ mbar, which is sufficient for characterization purposes.

4.4. DISCUSSION

Employing the pressure-frequency response as a material characterization method has several advantages over commonly used techniques. Compared to AFM that requires considerable deflections to estimate Young's modulus, i.e., the force-deflection curve should reach a cubic regime [22]($F \propto \delta^3$; F: tip force, δ: membrane's center deflection), pressurization using the surrounding gas requires a lower force for determining Young's modulus and distributes the load over the membrane, minimizing the chance of membrane failure. The method also reaches the nonlinear regime suitable for estimating Young's modulus with substantially less deflections and stresses, thus making it a more practical method for characterizing brittle nanomaterials such as polysilicon (see appendix 4.A1). Furthermore, unlike nonlinear dynamic characterization, which uses large driving signals to push the membrane into a nonlinear Duffing regime and requires proper calibration of the vibration amplitude [11], this method is independent of the vibration amplitude and only measures the resonance frequency as a function of the applied pressure.

It is worth noting that the low aspect ratio of ultra-thin membranes is an inherent feature of nanomechanical systems, which accounts for their display of nonlinear dynamics even at small amplitudes. In cases where a higher aspect ratio is present, plate models can be utilized instead of the membrane model proposed in this study. Yet, it is important to note that the bending rigidity essentially re-scales the linear stiffness of these systems, and in high-pressure regimes, the nonlinear stretching factors caused by pressure continue to dominate the Young's modulus characterization.

Several points should be kept in mind when employing the proposed method for characterization. First, in an optical detection scheme, the cavity depth has to be optimized so that the photodiode voltage is still linearly related to the motion at high amplitudes [35]. Moreover, gas leakage through the clamped boundaries and poor adhesion forces between the nanodrum and substrate should be avoided to ensure negligible leakage rates and to prevent significant variations of the internal cavity pressure during the measurement [21, 36, 37]. We note that the present model does not account for morphological imperfections such as wrinkles [38] and boundary slippage [39], that are proven to affect the stiffness of 2D material membranes.

Furthermore, when $P_{cav} > 0$, the cavity pressure change with the membrane's static deflection, and the squeeze film effect [40] may influence the dynamics of pressurized ultra-thin drums. Although both effects contribute significantly to the tension induced in the membrane, their cumulative effect on the drum's frequency shift near 1 bar and in the high-pressure regime is negligible for our polysilicon nanodrums, keeping the extracted value of Young's modulus unchanged. We also note that neglecting the squeeze-film effect and the bending rigidity of a relatively thick membrane may result in an over-

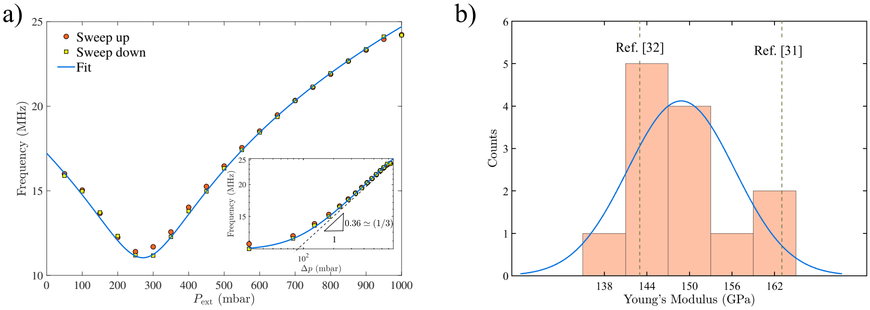

Figure 4.7: Experimental result obtained for polysilicon drums. a) Pressure-frequency of a drum in both sweeping up and down of pressure, fitted with our model with E = 155 GPa. b) Histogram of the Young's moduli obtained through fitting the experimental data with the average value of 148 GPa, and standard deviation of 7 GPa.

estimation of pre-tension; therefore, accounting for these two effects can enhance the accuracy of the anticipated pre-tension value which was estimated to be high in our analysis due to neglecting these effects. As discussed in the appendix 4.A2, by accounting for these two effects, the pre-tension value drops from 1.6 N/m to 1.1 N/m.

Other than material characterization, the model developed in this work can be used for estimating the deflection and resonance frequency shifts of pressurized membranes. These include 2D material resonant pressure sensors [4], microphones [41], and biosensors [6], where correct estimation of deflection due to surrounding fluid is important for probing the stiffness of the membrane. Furthermore, the analytical models provided here are also useful for accurate estimation of the mass-density of 2D membranes [42], which is often achieved by fitting the resonance frequency curves of the membrane as a function of pressure with tension and mass-density as the fit parameters.

4.5. CONCLUSION

In summary, attempts to use frequency shifts of pressurized nanodrums for characterization purposes were inaccurate previously due to lack of appropriate mathematical models. To resolve this, a multi-mode continuum model for predicting the dynamics of ultra-thin pre-tensioned drums subjected to high pressures is presented here. By maintaining in-plane and out-of-plane membrane deformations, we investigate the pressure-dependent resonance frequency and mode shapes and illustrate the crucial importance of mid-plane stretching in the high-pressure regime. We highlight the discrepancies by comparing the model's accuracy to previously reported analytical models and FEM simulations. By fitting the resonance frequency measurements of a series of polysilicon drums as a function of the applied pressure as determined by laser interferometry, we demonstrate the model's validity and applicability for determining Young's modulus of ultra-thin nanomaterial membranes using on-resonance high-frequency characterization. Since pressurization results in a distributed stress field compared to indentation, this method could be utilized as an effective toolset for determining the Young's modulus of brittle nanomaterials.

APPENDIX

4.A1. IDEAL FORCING REGIMES FOR CHARACTERIZATION

In this section, we use FEM simulations to compare the loading required to obtain Young's modulus using AFM and our proposed technique. To this end, we perform simulations for a pre-tensioned membrane ($n_0 = 0.3\,\mathrm{N\,m^{-1}}$) with a radius of 5 μm and a thickness of 20 nm, composed of polysilicon with Young's modulus of 160 GPa, density of 2330 kg/m3, and Poisson's ratio of 0.22. It is important to note that the indentation simulation is carried out assuming a cylindrical indenter with a tip radius of $R_{tip} = 8\,\mathrm{nm}$. Furthermore, we expect that the membrane will adhere to the indentor during the indentation and that there will be no slippage between the two.

By indenting a pre-tensioned membrane with a sharp tip, a large force is applied to a small area, resulting in substantial stress in the contact region. As established in the literature, this problem does not have an analytical solution over the entire range of indentations; instead, it converges to a linear response at small indentations and a cubic response at large indentations [43–45]. However, there is a plausible estimate based on linear and cubic terms for predicting Young's modulus and pre-tension as follows [46]:

$$F = \left[\frac{4\pi E}{3\left(1-\nu^2\right)}\frac{h^3}{R^2} + \pi n_0\right]\delta + \left[\frac{Eh}{R^2\left(1.05-0.15\nu-0.16\nu^2\right)^3}\right]\delta^3, \tag{4.A1}$$

where δ is the center deflection. This equation holds, only if the experimental data contains the entire range of indentations, culminating in a cubic stiffness. By plotting the $F-\delta$ response in log-log coordinates and evaluating the response's slope, one can determine whether it contains the cubic regime ($F \propto \delta^3$).

As illustrated in figure 4.A1(a, b), the same membrane approaches the cubic regime at a maximum indentation of 400 nm but reaches the nonlinear pressure-frequency domain ($f \propto \Delta p^{1/3}$) at a maximum pressure difference of 200 mbar, resulting in only about 100 nm of center deflection. If we fit these two sets of data using equation (4.A1) and the pressure-frequency model established in this study, the fitting values are identical; however, the maximum stress created in the indented nanodrum is significantly larger (see figure 4.A1(c, d)). Sharpe et al. [47] collected fracture strength data for polysilicon from several publications and determined that, depending on the size and testing technique, fracture strength values range from 1 to 5 GPa. Based on our basic FEM simulation, the polysilicon drum with the given material and geometrical parameters will fail prior to reaching the required stress regimes for extracting Young's modulus via AFM. As a result, utilizing the pressure-frequency response for extracting Young's modulus of brittle nanomaterials such as polysilicon can be more practical than AFM.

4.A2. CAVITY PRESSURE AND THE SQUEEZE FILM EFFECT

As indicated in the main text, deflection of the membrane results in changes in the volume of the cavity beneath it, which in turn yields a change in gas pressure. The difference between the external and cavity pressure makes the membrane bulge up/down, leading to an increase/decrease of cavity volume and decrease/increase of cavity pressure. Thus, we must include these effects to analyze their importance in determining Young's modulus and pre-tension of the membrane.

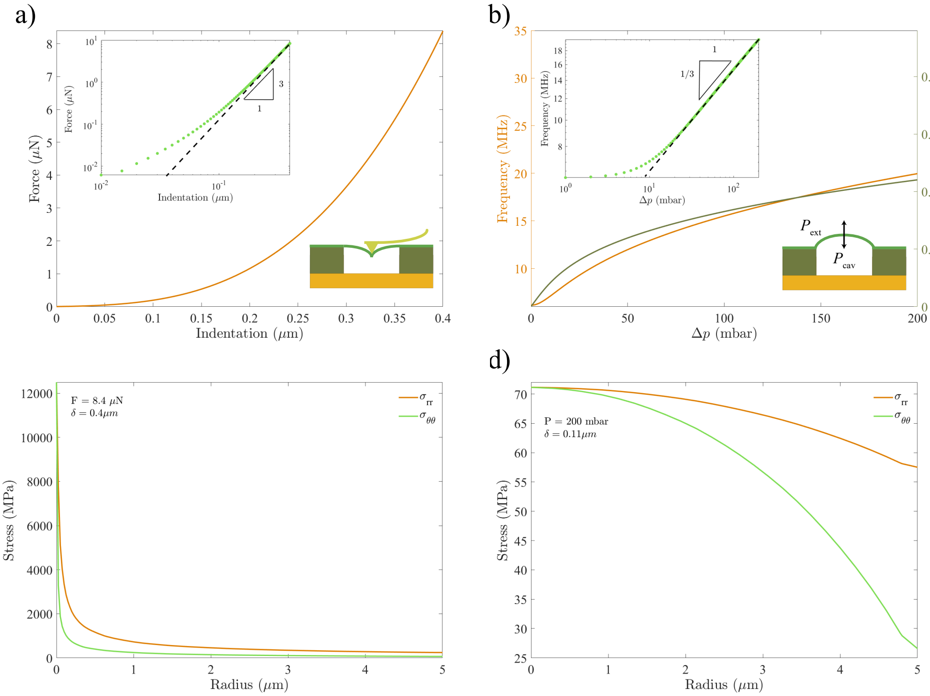

Figure 4.A1: **Comparison of the minimum loading required for approaching the nonlinear regime for determining Young's modulus in AFM, and pressurization.** a) Force-indentation curve of the center of a membrane under indentation, approaching the cubic stiffness necessary for characterization at 400 nm; b) variations of the fundamental frequency while increasing pressure, reaching one-third stiffness necessary for characterization at 200 mbar; c) Stress distribution in the membrane shown in subfigure (a), highlighting increased stresses near the contact area in AFM technique; d) stress distribution in the membrane shown in subfigure (b), highlighting more uniformly-distributed stress throughout the membrane.

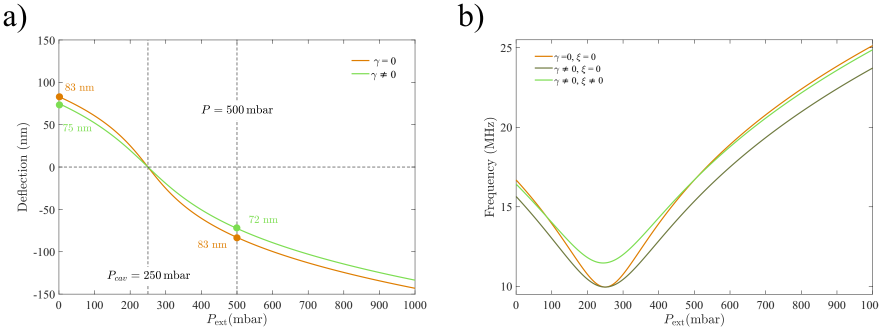

Figure 4.A2: **Influence of cavity pressure change and squeeze film effect.** a) Membrane deflection with ($\gamma \neq 0$) and without ($\gamma = 0$) cavity pressure change, which exhibits a slight asymmetry around the flat configuration when pressure variations are considered; b) the pressure-frequency response of a membrane considering cavity pressure change ($\gamma \neq 0$) and squeeze film effect ($\xi \neq 0$). The simulations are performed for a pre-tensioned ($n_0 = 1.1\,\mathrm{N\,m^{-1}}$) with a radius of 5 μm and a thickness of 33 nm, composed of polysilicon with Young's modulus of 148 GPa, density of 2330 kg/m3, and Poisson's ratio of 0.22.

Notably, since we are employing single-transverse-mode approximation in this section, the equations can be solved analytically. The equations and parameters used in this section are all in dimensional form.

Using the ideal gas law, we have the following expression:

$$P_{\text{cav}} V_1 = \left(P_{\text{cav}} - \delta p\right) V_2, \tag{4.A2}$$

where δp is the decrease in pressure due membrane buldging. Rewriting equation (4.A2) in integral form leads to:

$$\int_0^{2\pi}\int_0^R P_{\text{cav}} g r \mathrm{d}r \mathrm{d}\theta = \int_0^{2\pi}\int_0^R \left(P_{\text{cav}} - \delta p\right)\left(g + w\left(r,t\right)\right) r \mathrm{d}r \mathrm{d}\theta, \tag{4.A3}$$

where g represents the cavity depth, and $w(r,t)$ denotes the deflection of the membrane. Considering axisymmetric deflections, equation (4.A3) yields:

$$\frac{1}{2} g R^2 \delta p = \left(P_{\text{cav}} - \delta p\right) \int_0^R w\left(r,t\right) r \mathrm{d}r. \tag{4.A4}$$

Employing Bessel-form deflections (equation (8) of the main text), and setting $N_w = 1$ for the sake of simplicity, one can find:

$$\delta p = \frac{\gamma\, \tilde{q}_1\left(t\right)}{g + \gamma\, \tilde{q}_1\left(t\right)} P_{\text{cav}}, \tag{4.A5}$$

where $\gamma = 0.4318$. The total pressure difference is the subtraction of external pressure from the cavity pressure:

$$\Delta p = P_{\text{cav}} - \delta p - P_{\text{ext}} = \left(\frac{g}{g + \gamma \tilde{q}_1}\right) P_{\text{cav}} - P_{\text{ext}}. \tag{4.A6}$$

Inserting equation (4.A6) in equation (3) of the main text and following the procedure detailed out in the main text for $N_u \to \infty$ and $N_w = 1$ yields:

$$\ddot{\tilde{q}}_1 + \bar{\omega}_1^2 \tilde{q}_1 + \bar{\alpha}\left(\tilde{q}_1\right)^3 = \bar{\beta}\left(\frac{g^2}{\left(g + \gamma \tilde{q}_1\right)^2} P_{\text{cav}} - P_{\text{ext}}\right), \tag{4.A7}$$

where

$$\bar{\omega}_1 = \frac{2.4048}{R}\sqrt{\frac{n_0}{\rho h}}, \quad \bar{\alpha} = 1.181\varpi(\nu)\frac{E}{\rho R^4}, \quad \bar{\beta} = \frac{1.6019}{\rho h}. \tag{4.A8}$$

We can use equation (15) of the main text and obtain the following equation for the static bulged configuration:

$$\bar{\omega}_1^2 \tilde{q}_1^s + \bar{\alpha}\left(\tilde{q}_1^s\right)^3 = \bar{\beta}\left(\frac{g^2}{\left(g + \gamma \tilde{q}_1^s\right)^2} P_{\text{cav}} - P_{\text{ext}}\right). \tag{4.A9}$$

By expanding equation (4.A7) using Taylor series (up to first order in $\tilde{q}_1$) and accounting for the squeeze film effect, the equation of motion then becomes [48]:

$$\ddot{\tilde{q}}_1^d + \left[\bar{\omega}_1^2 + 3\bar{\alpha}\left(\tilde{q}_1^s\right)^2 + \xi\right] \tilde{q}_1^d = 0, \tag{4.A10}$$

where

$$\xi = \frac{2\gamma\bar{\beta}g^2}{\left(g+\gamma\tilde{q}_1^s\right)^3}P_{\text{cav}}, \tag{4.A11}$$

represents the increased stiffness due to the squeeze film effect. Thus, adding these two effects to equation (26) of the main text, leads to:

$$\left(\frac{g}{g+\gamma\tilde{q}_1^s}\right)P_{\text{cav}} - P_{\text{ext}} = 3.61\frac{n_0}{R^2}\tilde{q}_1^s + 0.737\varpi(\nu)\frac{Eh}{R^4}\left(\tilde{q}_1^s\right)^3, \tag{4.A12a}$$

$$f = \frac{2.4048}{2\pi R}\sqrt{\frac{n_0}{\rho h} + 0.612\varpi(\nu)\frac{E}{\rho R^2}\left(\tilde{q}_1^s\right)^2 + \frac{2\gamma\bar{\beta}g^2}{\left(g+\gamma\tilde{q}_1^s\right)^3}P_{\text{cav}}} \tag{4.A12b}$$

where $\tilde{q}_1^s$ is the static deflection at the center of the membrane. By solving Eqs. (4.A9) and (4.A10), we may derive the pressure-frequency response of a pressurized pre-tensioned membrane while accounting for cavity pressure change and squeeze film effect. As can be observed (see Eqs. (4.A9) and (4.A11)), both of these effects are significantly mitigated when the cavity pressure is low, which is also more favorable. Additionally, both phenomena result in asymmetric behavior around the flat configuration, meaning that for a given $|\Delta p|$, the deflection and hence the resonance frequency will be different, as shown in figure 4.A2. However, this asymmetry is negligible. At least for the studied case, figure 4.A2 illustrates that combining both phenomena does not significantly modify the response of our experiments at high pressures. This negligible difference will also diminish significantly if we maintain a low cavity pressure.

In contrast, ignoring squeeze-film effect at low pressures, results in an overestimation of the pre-tension in the membrane. The membrane's bending rigidity, which is not accounted for in our model, is another parameter that can influence the pre-tension estimation for thicker membranes ($h/R \geq 0.001$). For instance, the predicted pre-tension value ($n_0 = 1.6$ N/m) extracted from the fitting procedure for the sample shown in figure 5(a) of the main text, might be inaccurate owing to the aforementioned physical phenomena. The main contributions to this difference could be the added stiffness due to squeeze film effect and the bending rigidity that are not accounted for in the model. If we include the squeeze film effect, pre-tension reduces to $n_0 = 1.2$ N/m (see Eqs. (4.A12). If we also account for the effects of bending rigidity on the pressure-frequency response at the minimum point ($\Delta p = 0$) (see Ref. [49]), we find a membrane tension value of $n_0 = 1.15$ N/m.

BIBLIOGRAPHY

[1] Gupta, R. K., Alqahtani, F. H., Dawood, O. M., Carini, M., Criado, A., Prato, M., Migliorato, M. A. (2020). Suspended graphene arrays for gas sensing applications. 2D Materials, 8(2), 025006.

[2] Varghese, S. S., Lonkar, S., Singh, K. K., Swaminathan, S., Abdala, A. (2015). Recent advances in graphene based gas sensors. Sensors and Actuators B: Chemical, 218, 160-183.

[3] Koenig, S. P., Wang, L., Pellegrino, J., Bunch, J. S. (2012). Selective molecular sieving through porous graphene. Nature nanotechnology, 7(11), 728-732.

[4] Dolleman, R. J., Cartamil-Bueno, S. J., van der Zant, H. S., Steeneken, P. G. (2016). Graphene gas osmometers. 2D Materials, 4(1), 011002.

[5] Dolleman, R. J., Davidovikj, D., Cartamil-Bueno, S. J., van der Zant, H. S., Steeneken, P. G. (2016). Graphene squeeze-film pressure sensors. Nano letters, 16(1), 568-571.

[6] Rosłoń, I.E., Japaridze, A., Steeneken, P.G., Dekker, C. Alijani, F., (2022). Probing nanomotion of single bacteria with graphene drums. Nature Nanotechnology, pp.1-6.

[7] Castellanos-Gomez, A., Singh, V., van der Zant, H. S., Steele, G. A. (2015). Mechanics of freely-suspended ultrathin layered materials. Annalen der Physik, 527(1-2), 27-44.

[8] Akinwande, D., Brennan, C. J., Bunch, J. S., Egberts, P., Felts, J. R., Gao, H., Zhu, Y. (2017). A review on mechanics and mechanical properties of 2D materials—Graphene and beyond. Extreme Mechanics Letters, 13, 42-77.

[9] Los, J. H., Fasolino, A., Katsnelson, M. I. (2017). Mechanics of thermally fluctuating membranes. npj 2D Materials and Applications, 1(1), 1-5.

[10] Isacsson, A., Cummings, A. W., Colombo, L., Colombo, L., Kinaret, J. M., Roche, S. (2016). Scaling properties of polycrystalline graphene: a review. 2D Materials, 4(1), 012002.

[11] Davidovikj, D., Alijani, F., Cartamil-Bueno, S.J., van der Zant, H.S., Amabili, M. Steeneken, P.G., (2017). Nonlinear dynamic characterization of two-dimensional materials. Nature communications, 8(1), pp.1-7.

[12] Sajadi, B., Alijani, F., Davidovikj, D., Goosen, J., Steeneken, P.G. van Keulen, F., (2017). Experimental characterization of graphene by electrostatic resonance frequency tuning. Journal of Applied Physics, 122(23), p.234302.

[13] Sajadi, B., Wahls, S., van Hemert, S., Belardinelli, P., Steeneken, P.G. Alijani, F., (2019). Nonlinear dynamic identification of graphene's elastic modulus via reduced order modeling of atomistic simulations. Journal of the Mechanics and Physics of Solids, 122, pp.161-176.

[14] Lee, C., Wei, X., Kysar, J. W., Hone, J. (2008). Measurement of the elastic properties and intrinsic strength of monolayer graphene. Science, 321(5887), 385-388.

[15] Rega, G. and Settimi, V., (2021). Global dynamics perspective on macro-to nano-mechanics. Nonlinear Dynamics, 103(2), pp.1259-1303.

[16] Boddeti, N. G., Koenig, S. P., Long, R., Xiao, J., Bunch, J. S., Dunn, M. L. (2013). Mechanics of adhered, pressurized graphene blisters. Journal of Applied Mechanics, 80(4), 040909.

[17] Sajadi, B., Alijani, F., Goosen, H. and van Keulen, F., (2018). Effect of pressure on nonlinear dynamics and instability of electrically actuated circular micro-plates. Nonlinear Dynamics, 91(4), pp.2157-2170.

[18] Verbiest, G.J., Goldsche, M., Sonntag, J., Khodkov, T., von den Driesch, N., Buca, D. Stampfer, C., (2021). Tunable coupling of two mechanical resonators by a graphene membrane. 2D Materials, 8(3), p.035039.

[19] Ilyas, S., Alfosail, F.K., Bellaredj, M.L. and Younis, M.I., (2019). On the response of MEMS resonators under generic electrostatic loadings: experiments and applications. Nonlinear Dynamics, 95(3), pp.2263-2274.

[20] Nayfeh, A. H., Younis, M. I., and Abdel-Rahman, E. M. (2007). Dynamic pull-in phenomenon in MEMS resonators. Nonlinear dynamics, 48(1), 153-163.

[21] Lee, M., Davidovikj, D., Sajadi, B., Siskins, M., Alijani, F., Van Der Zant, H. S., Steeneken, P. G. (2019). Sealing graphene nanodrums. Nano letters, 19(8), 5313-5318.

[22] Komaragiri, U., Begley, M. R., Simmonds, J. G. (2005). The mechanical response of freestanding circular elastic films under point and pressure loads. J. Appl. Mech., 72(2), 203-212.

[23] Dolleman, R. J., Graphene Based Pressure Sensors (2014), Master's thesis, Delft University of Technology, the Netherlands.

[24] Bunch, J. S. (2008). Mechanical and electrical properties of graphene sheets. Ithaca, NY: Cornell University.

[25] Lee, J., Wang, Z., He, K., Shan, J., Feng, P. X. L. (2014). Air damping of atomically thin MoS2 nanomechanical resonators. Applied Physics Letters, 105(2), 023104.

[26] Mansfield, E. (1989). The Bending and Stretching of Plates. Cambridge University Press.

[27] Amabili, M. (2008). Nonlinear vibrations and stability of shells and plates. Cambridge University Press.

[28] A. Givois, A. Grolet, O. Thomas, J. F. De u (2019), On the frequency response computation of geometrically nonlinear flat structures using reduced-order finite element models, Nonlinear Dynamics 97, 174781.

[29] Guillot, L., Cochelin, B., and Vergez, C. (2019). A generic and efficient Taylor series–based continuation method using a quadratic recast of smooth nonlinear systems. International Journal for numerical methods in Engineering, 119(4), 261-280.

[30] Shoshani, O., and Shaw, S. W. (2021). Resonant modal interactions in micro/nanomechanical structures. Nonlinear Dynamics, 104(3), 1801-1828.

[31] Hemker, K. J., Sharpe Jr, W. N. (2007). Microscale characterization of mechanical properties. Annu. Rev. Mater. Res., 37, 93-126.

[32] Corigliano, A., De Masi, B., Frangi, A., Comi, C., Villa, A., Marchi, M. (2004). Mechanical characterization of polysilicon through on-chip tensile tests. Journal of Microelectromechanical Systems, 13(2), 200-219.

[33] Timoshenko, S. and Woinowsky-Krieger, S., 1959. Theory of plates and shells.

[34] Landau, L.D., Pitaevskii, L.P., Kosevich, A.M. and Lifshitz, E.M., 2012. Theory of elasticity: volume 7 (Vol. 7). Elsevier.

[35] Keşkekler, A., Shoshani, O., Lee, M., van der Zant, H. S., Steeneken, P. G., and Alijani, F. (2021). Tuning nonlinear damping in graphene nanoresonators by parametric–direct internal resonance. Nature communications, 12(1), 1-7.

[36] Bunch, J. S., Verbridge, S. S., Alden, J. S., Van Der Zande, A. M., Parpia, J. M., Craighead, H. G., McEuen, P. L. (2008). Impermeable atomic membranes from graphene sheets. Nano letters, 8(8), 2458-2462.

[37] Lee, M., Robin, M. P., Guis, R. H., Filippozzi, U., Shin, D. H., Van Thiel, T. C., Steeneken, P. G. (2022). Self-sealing complex oxide resonators. Nano letters, 22(4), 1475-1482.

[38] Sarafraz, A., Arjmandi-Tash, H., Dijkink, L., Sajadi, B., Moeini, M., Steeneken, P.G. and Alijani, F., 2021. Nonlinear elasticity of wrinkled atomically thin membranes. Journal of Applied Physics, 130(18), p.184302.

[39] Davidovitch, B. and Guinea, F., 2021. Indentation of solid membranes on rigid substrates with van der Waals attraction. Physical Review E, 103(4), p.043002.

[40] Ishfaque, A., and Kim, B. (2017). Analytical solution for squeeze film damping of MEMS perforated circular plates using Green's function. Nonlinear Dynamics, 87(3), 1603-1616.

[41] Baglioni, G., Pezone, R., Vollebregt, S., Zobenica, K.C., Spasenović, M., Todorovic, D., Liu, H., Verbiest, G., van der Zant, H.S. and Steeneken, P.G., 2023. Ultra-sensitive graphene membranes for microphone applications. Nanoscale.

[42] Chen, C., Rosenblatt, S., Bolotin, K.I., Kalb, W., Kim, P., Kymissis, I., Stormer, H.L., Heinz, T.F. and Hone, J., 2009. Performance of monolayer graphene nanomechanical resonators with electrical readout. Nature nanotechnology, 4(12), pp.861-867.

[43] Komaragiri, U., Begley, M.R. and Simmonds, J.G., 2005. The mechanical response of freestanding circular elastic films under point and pressure loads. J. Appl. Mech., 72(2), pp.203-212.

[44] Wan, K.T., Guo, S. and Dillard, D.A., 2003. A theoretical and numerical study of a thin clamped circular film under an external load in the presence of a tensile residual stress. Thin Solid Films, 425(1-2), pp.150-162.

[45] Vella, D. and Davidovitch, B., 2017. Indentation metrology of clamped, ultra-thin elastic sheets. Soft Matter, 13(11), pp.2264-2278.

[46] Castellanos-Gomez, A., Poot, M., Steele, G.A., Van Der Zant, H.S., Agraït, N. and Rubio-Bollinger, G., 2012. Elastic properties of freely suspended MoS2 nanosheets. arXiv preprint arXiv:1202.4439.

[47] Sharpe, W.N., Jackson, K.M., Hemker, K.J. and Xie, Z., 2001. Effect of specimen size on Young's modulus and fracture strength of polysilicon. Journal of Microelectromechanical systems, 10(3), pp.317-326.

[48] Dolleman, R.J., Chakraborty, D., Ladiges, D.R., Van Der Zant, H.S., Sader, J.E. and Steeneken, P.G., 2021. Squeeze-film effect on atomically thin resonators in the high-pressure limit. Nano Letters, 21(18), pp.7617-7624.

[49] Steeneken, P.G., Dolleman, R.J., Davidovikj, D., Alijani, F. and Van der Zant, H.S., 2021. Dynamics of 2D material membranes. 2D Materials, 8(4), p.042001.

5

5

CONCLUSION AND OUTLOOK

This chapter summarizes the dissertation's important findings and key results. Following that, future research directions are explored, beginning with an investigation of edge wrinkling in ultra-thin suspended membranes under external pressure. Subsequently, the investigation expands to look into the impact of inter-layer shear in multilayered membranes. Furthermore, the theoretical modeling of folds in 2D materials and its consequences for nonlinear mechanics are discussed. Then, the importance of interactions with the environment and the commonly disregarded effects of thermodynamics in the mechanical response of ultra-thin membranes are highlighted. The chapter finishes with a look at theoretical approaches for tuning geometric nonlinearity in ultra-thin membranes and other small-scale structures, including optimization techniques and machine learning algorithms.

5.1. CONCLUDING REMARKS

This dissertation investigated the nonlinear mechanics that govern the behavior of ultra-thin suspended membranes. We performed in-depth studies utilizing continuum mechanics (CM) theory and molecular dynamics (MD) simulations. Chapter 1 laid the framework for studying nonlinear mechanics of membranes, identifying sources of nonlinearity, and introducing the approaches used throughout the dissertation. Chapters 2 and 3 challenged the commonly held assumptions of flatness and uniform pre-tension in ultra-thin membranes and discussed the role of wrinkles and non-uniform stress on the nonlinear mechanics and dynamics of ultra-thin membranes. Then, in Chapter 4, we investigated the effect of pressure on the resonance behavior of these membranes.

NONLINEAR MECHANICS OF WRINKLED MEMBRANES

In Chapter 2, we investigated the complicated relationship between wrinkles and the mechanical behaviour of graphene membranes using MD simulations. We created wrinkle patterns utilizing two different sources: pre-strain and atomic defects. Under biaxial loading, these wrinkled membranes demonstrated subtle stress-strain behavior, with two linear regions separated by an apparent transition. Notably, the sharpness of this transition differed with the origin of the wrinkle: more pronounced for wrinkles resulting from unequal stresses at their edges, and smoother for those generated by crystal defects.

To fully comprehend the observed stress-strain anomaly we developed a practical phenomenological model based on empirically measurable parameters. This model accurately quantifies the impact of wrinkles on thin membrane mechanics and is validated by fitting to MD-simulated nonlinear responses from various membranes. Our model demonstrates that the sharpness of the transition in the stress-strain profile is a valid predictor of wrinkle type. This approach not only improves our fundamental understanding of the complex mechanical behavior of wrinkled membranes, but it also gives a practical method for quantifying and categorizing wrinkle effects based on the sharpness of observed transitions in the stress-strain response.

QUANTIFYING STRESS DISTRIBUTION IN SUSPENDED MEMBRANES

In Chapter 3, the widely accepted assumption of uniform pre-stress in the mechanical modeling of ultra-thin drum membranes was investigated. Our focus was on suspended drums made from 2D materials, which have great potential for sensing applications. Non-uniform stress distributions frequently hinder industrialization of these ultra-thin devices due to inherent device-to-device variability in the manufacturing process. In order to study this issue, a theoretical method was developed to extract stress distribution from the mode shapes and frequencies of a membrane. To check the applicability of the method, experimental mode shapes of ultra-thin graphene membranes were utilized.

Our methodology entailed a thorough examination of the experimentally obtained mode shapes and frequencies from these large graphene drums. A Föppl-von Kármán plate model is used to obtain the governing equations. We derived static deformations and stress distributions based on mode shapes and frequency using an iterative technique utilizing governing equations. Notably, our findings called into question the validity of the uniform pre-stress assumption, highlighting the need for caution when applying this assumption to mechanical models of ultra-thin membranes.

PRESSURE EFFECTS ON RESONANCE FREQUENCY OF SUSPENDED MEMBRANES

In Chapter 4, we analyzed the dynamics of pressurized ultra-thin membranes. To address this issue, we established a predictive model for pressure-frequency responses based on three fundamental assumptions: recognizing the impact of statically deformed configurations on stiffness, acknowledging the importance of midplane stretching with increasing pressure, and incorporating changes in mode shapes during static deformation. Using this model, we examined experimental pressure-frequency data from polysilicon drums to determine their Young's modulus. Notably, the obtained Young's modulus values were consistent with published literature, demonstrating the robustness of our predictive approach.

This chapter presented a multi-mode continuum model intended to capture the nonlinear pressure-frequency response of pre-tensioned membranes under large deflections ($w/h \gg 1$, where w denotes center deflection and h shows the membrane thickness). Validation from experiments on polysilicon nanodrums subjected to opto-thermal excitation and pressure variations called into question conventional theories on pressurized nanomaterial membranes. The findings highlighted the necessity of measuring not just pressure-induced changes in nanodrum tension, but also changes in membrane static shape, mid-plane stretching, and the contributions of higher modes. Overall, Chapter 4 presented a high-frequency mechanical characterization method that offers a rapid and non-contact approach for determining Young's modulus in ultra-thin membranes.

5.2. PROSPECTIVE RESEARCH

The primary purpose of this thesis is to investigate the inherent complexities with nonlinear mechanics in ultra-thin suspended membranes. To that end, we examined a wide range of field-related challenges, resulting in the development of suitable analytical techniques. Throughout the four-year Ph.D. program, a number of other intriguing topics associated with nonlinear mechanics analysis were identified, too. The following discussion will expand on these selected subjects, outlining their significance and proposing new avenues for future research.

EDGE WRINKLING

Compressive stresses are the most prevalent root of buckling, especially when the entire structure is compressed uniformly. As a result, it is commonly believed that structures under tension do not exhibit buckling behavior. However, localized compressive strains can cause localized buckling or wrinkling even in tensioned membranes. Edge wrinkling is particularly notable in this respect, as it can be seen even in membranes under uniform stress. This behavior arises when a sufficiently large out-of-plane force, such as pressure from a gas or liquid, acts in the presence of inadequate in-plane tension, inducing azimuthal compressive stress along the edge and resulting in local buckling or edge wrinkling [1].

This observation caught our attention when proposing a model for the dynamics of pressurized membranes, which focused on modeling the effect of pressure on mem-

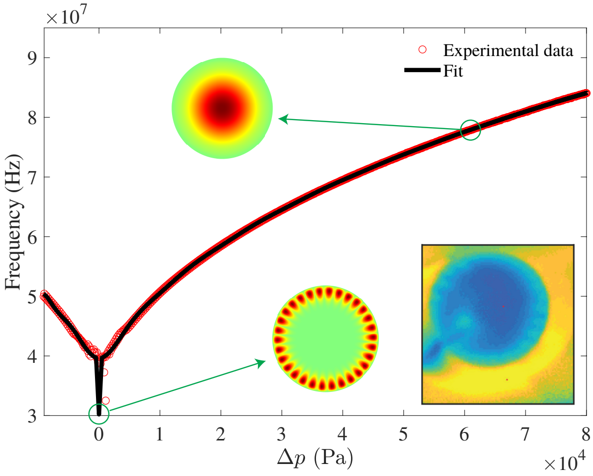

Figure 5.1: Pressure-frequency response of a sealed graphene membrane and corresponding FEM fitting. As illustrated, the fundamental mode shape transitions to a local mode when the pressure difference is zero $\Delta p = 0$. The membrane under investigation has a radius of $R = 2.5$ μm and a thickness of $h = 7.6$ nm. The FEM fitting is obtained using Young's modulus of $E = 350$ GPa and a uniform compression of $n_0 = -0.71$ N·m. The inset shows the Raman mapping of the sealed drum with subtly apparent edge wrinkles [2].

brane resonance frequency. Our initial attempts on modelling relied on experimental data from sealed graphene membranes, aimed at preventing gas leakage [2]. Despite AFM data suggesting flatness, the emergence of edge wrinkles under external pressure, as revealed by Raman spectroscopy images, underscored the need for further investigation [2]. As an initial step, a trial-and-error fitting process was conducted using the finite element method (FEM) to simulate the fundamental resonance of pressurized membranes under uniform tension or compression. While this method yielded satisfactory results for the studied drum (See figure 5.1), challenges persisted. Experimentation with FEM simulations revealed that under high compression and initial buckling, the fundamental mode shape could change shape, with vibrations around the edge of the membrane rather than the whole surface of the membrane.

Despite these preliminary efforts to understand the impact of edge wrinkling, additional controlled experiments should be conducted to offer sufficient evidence for validation of future potential theoretical research. To allow the model described in chapter 4 to predict edge wrinkling as well, one must drop the assumption of only retaining axisymmetric mode shapes and include asymmetric mode shapes as well.

INTER-LAYER SHEAR FORCES

Traditional membrane and plate models, which rely on the assumption of continuity, encounter deviations in the context of multi-layer 2D materials. Generally, few-layer 2D materials are treated as homogeneous solid membranes, assuming that the layers are bonded together without sliding. However, it is important to note that these layers are bonded with weak van der Waals forces. These interactions are nonlinear and anhar-

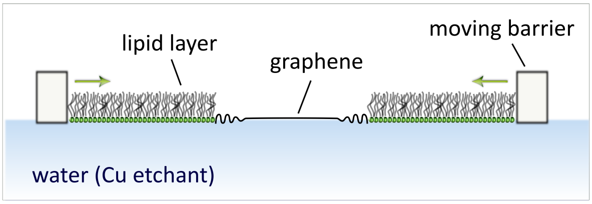

Figure 5.2: Schematic outlining the experimental method for straining the graphene membrane.

monic, rendering the modeling of few-layer 2D materials as homogeneous solids prone to errors.

Recent studies have provided new insights into the influence of inter-layer shear on the mechanical properties of layered structures. Inter-layer shear effects have been shown to induce changes in bending rigidity and alter bending mechanisms, challenging traditional continuum models [3]. Furthermore, the impact of inter-layer shear on damping mechanisms has received attention, with studies investigating sliding motion between layers during deformation, leading to energy dissipation and inherent damping capacity in the material [4–6]. However, the proposed models are empirical fits to the physics and need more investigation.

MD simulations offer a powerful approach to investigating the effects of inter-layer shear on the damping mechanism and bending rigidity of structures. One of the main advantages of MD simulations in addressing these challenges is their ability to manipulate inter-layer shear strength through the use of the Lennard-Jones potential between layers. By adjusting the number of layers and van der Waals interaction strength, it becomes feasible to validate whether the observed bending rigidity or dissipation observed in experiments are genuine and not influenced by other factors. Moreover, MD simulations enable the verification and examination of the widely-assumed friction-like slipping mechanism between layers, providing valuable insights for developing continuum-based models of layered membranes. Additionally, simulations involving bi- or multi-layer graphene membranes with varying inter-layer bonding strengths can be conducted to explore these effects, akin to simulations carried out in Chapter 5.

NONLINEAR MECHANICS OF FOLDS IN THE LIQUID-SOLID INTERACCE

The presence of folds, whether unintended or engineered, in 2D material membranes can significantly alter their mechanical behavior. Theoretical studies have suggested that surface corrugations such as folds may enhance the bending rigidity of membranes; however, rigorous experimental validation is still needed [7, 8]. An intriguing avenue of research could involve quantifying the increase in bending rigidity of a cantilever made of folded graphene. Exciting the cantilever and measuring its resonance frequency could enable the determination of the bending rigidity of the folded graphene cantilever and estimation of the extent of this enhancement using a simple continuum mechanics model.

Recent efforts have developed an experimental procedure for inducing wrinkles and folds in graphene membranes, providing a valuable opportunity to investigate the nonlinear mechanics of folds through experiments. In this method, graphene grown via

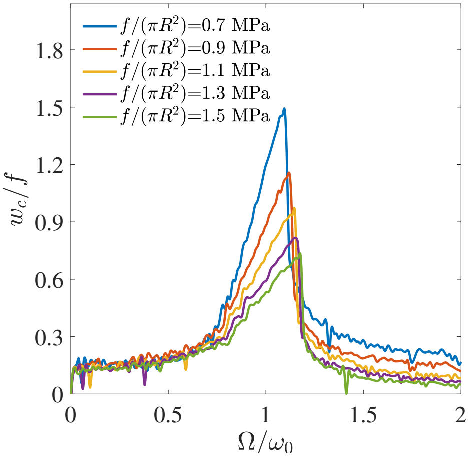

Figure 5.3: Normalized frequency-response of graphene membrane resonators under various forcing amplitudes. The decrease in peak amplitude indicates nonlinear damping forces due to the coupling with a Nosé-Hoover thermostat. Here, Ω and ω_0 denote the excitation frequency and fundamental resonance frequency, respectively, while f denotes the non-dimensionalized excitation force amplitude.

chemical vapor deposition (CVD) on a copper foil is immersed in a solution of water and copper etchant. Subsequently, the edges of the graphene membrane are affixed to large lipid layers, which are then attached to rigid barriers on the opposite side. By adjusting the positions of these barriers, compression strains can be induced in the graphene membrane. A schematic of the experimental setup is illustrated in Figure 5.2.

An alternative to conducting experiments is to simulate the same setup using molecular dynamics (MD) simulations. One can create a network of folds in a 2D material membrane [9] and then excite the structure and study the resonance frequency shifts due to increase of bending rigidity resulting from the creation of the fold network compared to a flat membrane.

NONLINEAR DAMPING DUE TO HEAT BATH INTERACTIONS

Energy dissipation in 2D material membranes can stem from both internal and external sources. While 2D resonators exhibit low dissipation at low temperatures [10, 11], their low-quality factors at room temperature [12, 13] remain unexplained. Nonlinear, amplitude-dependent dissipation is also not well understood [14], with various sources identified, including anelasticity [15], Akheizer relaxation [16, 17], intermodal interactions [18, 19], and environmental coupling [20]. These multiple origins complicate efforts to isolate and understand each contribution. As a result, a theoretical approach combining physical concepts, modeling, and simulations is essential. Studies on nonlinear damping in 2D materials [11] have shown that interactions with a heat bath may significantly influence amplitude-dependent damping. A microscopic perspective can offer further insight into how this coupling contributes to nonlinear dissipation.

In the course of this PhD studies, MD simulations were performed to study the damp-

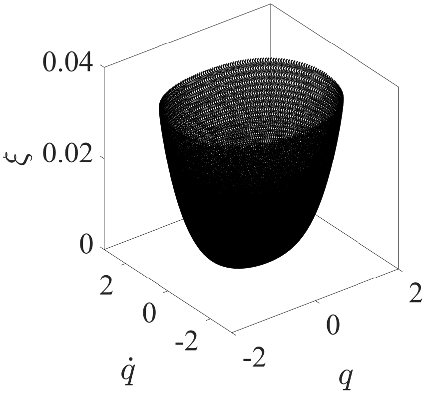

Figure 5.4: Nonlinear characteristics of damping induced by coupling with a heat bath. Damping surface ξ as a function of q and $\dot{q}$, illustrating higher-order damping behaviors.

ing behavior of an ultra-thin membrane when coupled to a Nosé-Hoover thermostat, often used to model heat baths in simulations. The results indicated nonlinear dissipation, evident from the frequency response curves that show a decrease in peak amplitude with increasing forcing amplitude, as shown in Fig. 5.3.

While MD simulations provide insights into these nonlinear effects, the Nosé-Hoover thermostat alone does not fully capture the complexities of membrane-substrate interactions. To simplify the analysis and validate the observed nonlinear damping, a theoretical model based on a single degree of freedom Nosé-Hoover oscillator was developed. The governing equations for the membrane-heat bath system are derived using energy conservation, leading to the following equations of motion:

$$m_{\text{eff}}\ddot{q} + m_{\text{eff}}\xi\dot{q} + k_1 q + k_3 q^3 = F_{\text{eff}}\cos(\Omega t), \tag{5.1a}$$

$$\dot{\xi} = \frac{2}{M}\left(\frac{1}{2}m_{\text{eff}}\dot{q}^2 - \frac{3}{2}Nk_b T_\infty\right), \tag{5.1b}$$

where m_{eff}, F_{eff}, and the constants k_1, k_3 are defined as before. These equations describe the interaction between the membrane and the thermostat and capture the essential dynamics responsible for nonlinear damping.

To determine the damping coefficient ξ as a function of q and $\dot{q}$, we simulate the Nosé-Hoover membrane model by integrating Eqs. (5.1) over time. A linear chirp is used to vary the excitation frequency and analyze the system's response. The results, plotted as ξ versus q and $\dot{q}$, reveal a 3D surface showing amplitude- and velocity-dependent damping (Fig. 5.4).

Fitting the surface of ξ as a function of q and $\dot{q}$, this system can be approximated by the following equation of motion for the membrane, incorporating the nonlinear damping terms:

$$\ddot{q} + \xi_{0,1}\dot{q} + \xi_{2,1}q^2\dot{q} + \xi_{0,3}\dot{q}^3 + \xi_{4,1}q^4\dot{q} + q + \alpha q^3 = F_{\text{eff}}\cos(\Omega t)\,. \tag{5.2}$$

To assess the realism of the Nosé-Hoover thermostat in modeling this interaction, it is worth noting that the model is idealized. A more accurate representation would involve graphene membranes coupled to a silicon substrate, where the substrate is thermostatted and the membrane vibrates in an NVE ensemble while interacting with the substrate through van der Waals forces. This would offer a more realistic approximation of heat bath interactions and provide further insights into the role of substrate coupling in nonlinear damping. However, these results reveal the value of theoretical methods such as molecular dynamics and continuum mechanics in unraveling the mechanisms of nonlinear damping, which could inform future studies aiming to resolve this complex phenomenon.

TUNING OF GEOMETRIC NONLINEARITY

The fast activation of geometric nonlinearities under piconewton forces in 2D material membranes emphasizes the necessity of method to control, nullify or enhance mechancial nonlinearities. Although current methods for controlling nonlinearity primarily involve using external nonlinear forces like electrostatic loading, our numerical simulations in previous chapters emphasize the significant influence of geometric parameters and tension on geometric nonlinearity. This suggests the potential for controlling the nonlinearity of 2D materials through geometric design.

While existing literature often focuses on analytical models based on standard geometries (e.g., circles, squares, ovals) for slender devices, the effectiveness of these models varies depending on the underlying geometry. As such, there is a need to develop tools capable of effectively handling intricate geometries.

Although the utilization of commercial Finite Element packages in conjunction with established shape or topology optimization algorithms may initially seem like a viable solution, the substantial computational costs associated with nonlinear dynamic simulations and optimization techniques pose significant challenges. To address these challenges, reduced-order modeling techniques based on Finite Element Analysis (FEA), such as the STiffness Evaluation Procedure (STEP) method [21], offer a promising approach by reducing the number of degrees of freedom involved.

To illustrate this approach, efforts have been made to develop a method for accurately modifying the nonlinear stiffness of circular ultra-thin membranes by intentionally introducing circular holes. By employing the STEP method for reduced-order modeling and utilizing the particle swarm optimization (PSO) algorithm, the nonlinear stiffness of the device was adjusted. Figure 5.5 outlines the study's structure, with a detailed flowchart available in [22]. The algorithm begins by generating N distinct membrane configurations with random numbers of holes at varying locations and with different radii. Subsequently, the STEP method reduces each membrane structure to a mass-spring system consisting of linear and nonlinear springs. The nonlinear stiffness associated with each membrane configuration is then evaluated to determine whether an optimum within predefined constraints has been achieved. If not, the algorithm iteratively generates new configurations based on previous ones until the optimum is reached.

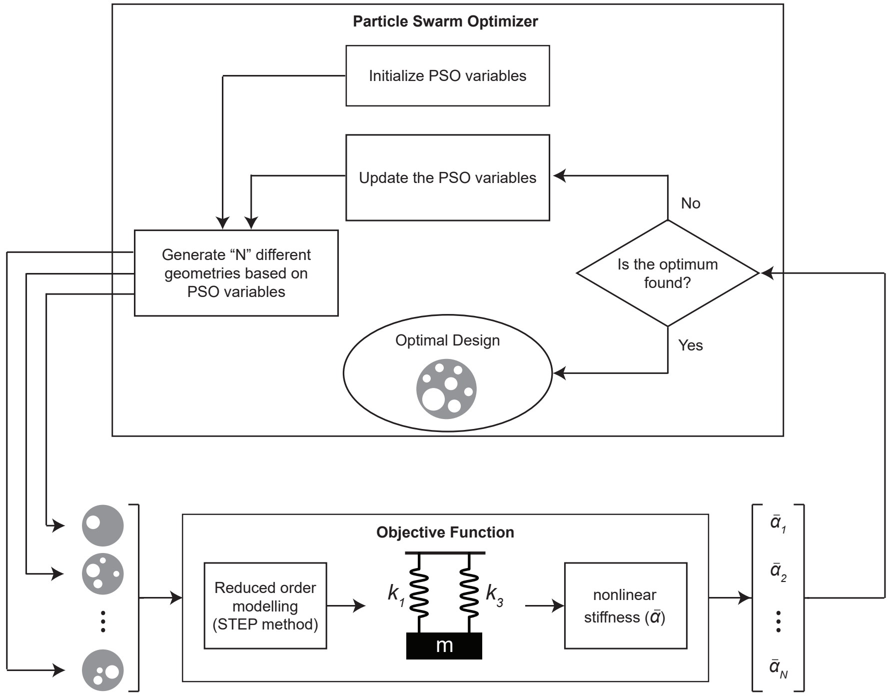

Figure 5.5: Flowchart depicting the combined PSO-STEP algorithm for tuning nonlinear stiffness. The approach involves initializing PSO variables, generating multiple membrane configurations, simplifying the full membrane model into a mass-spring model, calculating the nonlinear stiffness for each configuration, and subsequently assessing whether the best solution meeting all predefined criteria has been obtained. This iterative process continues until the optimal solution is achieved.

BIBLIOGRAPHY

[1] King, H., Schroll, R.D., Davidovitch, B. and Menon, N., 2012. Elastic sheet on a liquid drop reveals wrinkling and crumpling as distinct symmetry-breaking instabilities. Proceedings of the National Academy of Sciences, 109(25), pp.9716-9720.

[2] Lee, M., Davidovikj, D., Sajadi, B., Siskins, M., Alijani, F., Van Der Zant, H.S. and Steeneken, P.G., 2019. Sealing graphene nanodrums. Nano letters, 19(8), pp.5313-5318.

[3] Han, E., Yu, J., Annevelink, E., Son, J., Kang, D.A., Watanabe, K., Taniguchi, T., Ertekin, E., Huang, P.Y. and van der Zande, A.M., 2020. Ultrasoft slip-mediated bending in few-layer graphene. Nature materials, 19(3), pp.305-309.

[4] Ferrari, P.F., Kim, S. and Van Der Zande, A.M., 2021. Dissipation from interlayer friction in graphene nanoelectromechanical resonators. Nano letters, 21(19), pp.8058-8065.

[5] Wei, X., Meng, Z., Ruiz, L., Xia, W., Lee, C., Kysar, J.W., Hone, J.C., Keten, S. and Espinosa, H.D., 2016. Recoverable slippage mechanism in multilayer graphene leads to repeatable energy dissipation. ACS nano, 10(2), pp.1820-1828.

[6] Lahiri, D., Das, S., Choi, W. and Agarwal, A., 2012. Unfolding the damping behavior of multilayer graphene membrane in the low-frequency regime. ACS nano, 6(5), pp.3992-4000.

[7] Blees, M.K., Barnard, A.W., Rose, P.A., Roberts, S.P., McGill, K.L., Huang, P.Y., Ruyack, A.R., Kevek, J.W., Kobrin, B., Muller, D.A. and McEuen, P.L., 2015. Graphene kirigami. Nature, 524(7564), pp.204-207.

[8] Sajadi, B., van Hemert, S., Arash, B., Belardinelli, P., Steeneken, P.G. and Alijani, F., 2018. Size-and temperature-dependent bending rigidity of graphene using modal analysis. Carbon, 139, pp.334-341.

[9] Zhang, K. and Arroyo, M., 2014. Understanding and strain-engineering wrinkle networks in supported graphene through simulations. Journal of the Mechanics and Physics of Solids, 72, pp.61-74.

[10] Iao, T., Yeom, S., Wang, P., Standley, B. and Bockrath, M., 2014. Graphene nanoelectromechanical systems as stochastic-frequency oscillators. Nano letters, 14(6), pp.2982-2987.

[11] Eichler, A., Moser, J., Chaste, J., Zdrojek, M., Wilson-Rae, I. and Bachtold, A., 2011. Nonlinear damping in mechanical resonators made from carbon nanotubes and graphene. Nature nanotechnology, 6(6), pp.339-342.

[12] Morell, N., Reserbat-Plantey, A., Tsioutsios, I., Schadler, K.G., Dubin, F., Koppens, F.H. and Bachtold, A., 2016. High quality factor mechanical resonators based on WSe2 monolayers. Nano letters, 16(8), pp.5102-5108.

[13] Xu, X., Pereira, L.F., Wang, Y., Wu, J., Zhang, K., Zhao, X., Bae, S., Tinh Bui, C., Xie, R., Thong, J.T. and Hong, B.H., 2014. Length-dependent thermal conductivity in suspended single-layer graphene. Nature communications, 5(1), p.3689.

[14] Barton, R.A., Ilic, B., Van Der Zande, A.M., Whitney, W.S., McEuen, P.L., Parpia, J.M. and Craighead, H.G., 2011. High, size-dependent quality factor in an array of graphene mechanical resonators. Nano letters, 11(3), pp.1232-1236.

[15] Han, X. and Wang, M., 2009. General decay of energy for a viscoelastic equation with nonlinear damping. Mathematical Methods in the Applied Sciences, 32(3), pp.346-358.

[16] Kumar, S., Rebari, S., Pal, S.P., Yadav, S.S., Kumar, A., Aggarwal, A., Indrajeet, S. and Venkatesan, A., 2021. Temperature-dependent nonlinear damping in palladium nanomechanical resonators. Nano Letters, 21(7), pp.2975-2981.

[17] Atalaya, J., Kenny, T.W., Roukes, M.L. and Dykman, M.I., 2016. Nonlinear damping and dephasing in nanomechanical systems. Physical Review B, 94(19), p.195440.

[18] Keşkekler, A., Shoshani, O., Lee, M., van der Zant, H.S., Steeneken, P.G. and Alijani, F., 2021. Tuning nonlinear damping in graphene nanoresonators by parametric–direct internal resonance. Nature communications, 12(1), p.1099.

[19] Güttinger, J., Noury, A., Weber, P., Eriksson, A.M., Lagoin, C., Moser, J., Eichler, C., Wallraff, A., Isacsson, A. and Bachtold, A., 2017. Energy-dependent path of dissipation in nanomechanical resonators. Nature nanotechnology, 12(7), pp.631-636.

[20] Zaitsev, S., Shtempluck, O., Buks, E. and Gottlieb, O., 2012. Nonlinear damping in a micromechanical oscillator. Nonlinear Dynamics, 67, pp.859-883.

[21] Muravyov, A.A. and Rizzi, S.A., 2003. Determination of nonlinear stiffness with application to random vibration of geometrically nonlinear structures. Computers & Structures, 81(15), pp.1513-1523.

[22] Nasirshoaibi, M., 2023. Tuning nonlinear stiffness of circular membranes by design optimization. M.Sc. thesis, Delft University of Technology.

ACKNOWLEDGMENTS

During the past four years of my PhD journey at TU Delft, life has presented me with a splendid opportunity for growth and learning. This period has been invaluable, not only in terms of acquiring technical knowledge but also in developing various social and personal skills that have enriched my life in ways beyond measure. I am truly grateful for the presence and support of numerous people who have contributed to making this experience so rewarding. Therefore, I would like to take this moment to express my gratitude to each and every one of them.

I extend my heartfelt thanks to **Farbod**, my promotor and supervisor, for his unwavering support and guidance throughout my four-year journey. Farbod, your dedication has been truly remarkable. We've had numerous meetings, often exceeding three per week, and I can't recall a week without our insightful discussions. Your role has went beyond that of a supervisor; you've been a guiding presence, akin to a supportive older brother, helping me get used to a new country and navigate its challenges. Your expertise in teaching, supervision, and research has been invaluable, and I am immensely grateful for your contribution to my success. Thank you for everything!

I would want to thank **Peter**, my promotor, for his vital presence in making this project a success. Peter, your exceptional ability to see the bigger picture while having expertise in multiple disciplines is extremely impressive. Your leadership in scientific research is outstanding, and I am grateful for your advice and support along this journey. Thank you for your invaluable contributions to this project.

I must also thank **Gerard** for his unexpected yet crucial involvement in my PhD quest. Gerard, I must admit that at the start of my PhD, I could not have imagined your considerable engagement in more than half of my projects. However, your support and insights have proven to be some of the most valuable contributions to my research. Thank you for your invaluable help and insight.

Throughout these four years, I've had the privilege of being a part of the Dynamics of Micro and Nanosystems (DMN) team. It's been an enriching experience learning from such talented individuals and enjoying our time together. I want to give a special thanks to **Curry**. Our discussions were always enjoyable, and your insights were truly valuable. We've shared many coffees and collaborated on two papers, all thanks to your tendency for simplifying the paper-writing process. And let's not forget your amazing cooking skills – your Chinese dishes were the best I've ever had. I'd also like to thank the rest of the group: **Dongil**, **Martin** (Robin), **Matthijs**, **Martin** (Lee), **Makars**, **Kautuk**, **Ruben**, and **Maurits**. Our weekly DMN meetings were invaluable, providing important insights into the field. As a mechanical engineer delving into more fundamental physics projects, these meetings helped broaden my understanding. A big thank you to everyone who participated and contributed to my learning journey, especially **Richard**, **Sabina**, **Wouter**, and **Saurabh**. And to those whose names slip my mind, your support has been greatly appreciated.

Working on the Enigma project has been the most enjoyable work experience I've had. Our lengthy meetings with Farbod, where we updated each other on our progress, were particularly memorable. **Irek**, you taught me so much about bacteria and showed me just how brave (or maybe a little crazy) a researcher can be by experimenting with wild ideas. Our desk setup allowed us to work eye to eye for almost three and a half years, and I'll always remember being able to ask for a coffee just by seeing you through the space between my monitors. I hope you the bests with your startup SoundCell! **Ata**, you researched and simulated everything I wanted to explore. Not only are you skilled in research, but you also showcase your talents in playing musical instruments, singing, sports, and numerous other endeavors. You truly embody the concept of a multi-dimensional individual. I hope you the bests in the rest of your academic career! **Xianfeng**, seeing your excitement about levitation every week was inspiring. Your high ambitions for your work always stood out to me. Hope you the bests in Singapore! **Arthur**, your calm manner conceals a genuine enthusiasm for mathematics that was contagious. Your ability to simplify hard mathematical concepts and make them understandable to others was genuinely impressive. Without your tremendous support, our paper would not have been possible. Best wishes to your new career as an assistant professor. Continue to inspire others with your passion of math and your cello skills. **Zichao**, you're one of the few people who tried to learn Persian from me, and your enthusiasm for learning something new, even if you may never use it, was truly exemplary. I hope to see you again next time in your defence. **Hadi**, you were instrumental in teaching me the complexities of writing a high-quality journal manuscript and provided valuable insights into the world of wrinkling in graphene. Though our collaboration was limited due to the pandemic's limits, your guidance had a long-term influence. I wish you and your family all the best in your future pursuits. **Abhilash**, your outstanding talent and expertise were undeniable, even if you weren't able to join us in our Enigma meetings. Your reputation as the department's AFM guy spoke volumes about your ability and understanding. As you move to ASML, I am confident that you will continue to shine as brightly as you did at TU.

Let's not forget to mention my office mates, who made our office hours fun and enjoyable. **Tomas**, despite being a fan of Real Madrid!, I appreciated your shared enthusiasm for the sport. Your positive attitude and willingness to help at the start of my PhD journey were truly uplifting. **Satadal**, your brilliant mind for science was evident in every conversation we had. It was rare to catch you discussing anything other than scientific facts or explaining daily occurrences using science. **Minxing**, although you were mostly in the labs, your occasional presence in the office always provided me with reassurance that I was on track to complete my PhD on time. Your encouragement was truly heartwarming. **Pieter**, thank you for organizing so many department activities, even though

I regrettably missed many of them. I'm still looking forward to the day you join us for a board game night gathering. **Andrea**, spending two whole days together at the ASML PhD masterclass allowed me to see firsthand how brilliant, thoughtful, and modest you are. I also want to extend my gratitude to all the other individuals who contributed to making our office times more enjoyable: **Elyas**, **Xiliang**, **Inge**, **Nils**, **Tufan**, **Vincent**, **Qais**, **Megha**, **Murat**, **Dilek**, **Simona**, and **Sabiju**.

I'd also like to convey my sincere thanks to my friends, who made life outside of university enjoyable and helped ease academic stress. **Amirabbas & Zahra**, **Davood & Afagh**, **Ali & Azar**, **Gurhan & Parinaz**, **Irek & Martina**, thank you for making my life enjoyable and memorable. Your friendship has been a source of joy and support. **Francesco**, I wonder whether you were Iranian in a prior life! Thanks for being present in our parties and it was nice to see you learning our language and culture so easily. I would also like to extend my special thanks to **Saleh & Mahnaz**, **Ali & Shahrzad**, **Ali & Zahra**, **Ghobad**, and **Amir** for their wonderful presence in our gatherings. Whether we were playing board games, partying, or having barbeques, your company made every moment special. Saleh, I want to particularly thank you for playing a big brother role in my life from the first day of my PhD. Your desk being next to mine made you my go-to person for both scientific and daily life questions. You made the transition period of my migration easier and supported me in many aspects of my life. Ali, I also want to express my gratitude to you for being there from the beginning. From showing me around the university, the neighborhood, and the city to helping me buy my first bike and car. It's the little things you did that made our friendship feel like a strong bond.

I'd want to take this moment to convey profound gratitude to my dear parents, **Mohammad & Sadri**. Your support and endless love have been the foundation of my path. You implanted in me the principles of determination, commitment, and kindness from early on in life. You were the first ones to believe in me, standing by my side through every challenge and setback. Your sacrifices, both big and small, have paved the way for my success, and I am forever thankful for your constant dedication to my well-being and happiness. Your love and support have shaped me into the person I am today, and I am forever indebted to you for your endless generosity and unwavering devotion. Thank you, from the bottom of my heart, for being the most extraordinary parents one could ever hope for.

I'd want to convey my heartfelt appreciation to my close friend and wife, **Shaghayegh**, who has been a source of comfort and encouragement during the difficult and stressful times of my PhD journey. Our paths crossed unexpectedly on a train from Mashhad to Tehran, and we had no idea that this accidental encounter would lead to a lifelong relationship. Shaghayegh, your presence in my life has brought immense joy and comfort. Thank you for your constant kindness and understanding, and for patiently listening to my work-related complaints, despite the fact that mechanical engineering is not your area of expertise as a midwife. Your support means the world to me. As we navigate through life together, my heartfelt wish is to be as good a partner to you as you have been to me. Thank you for being my rock and for sharing this journey with me.

CURRICULUM VITÆ

Ali SARAFRAZ

16-05-1993 Born in Mashhad, Iran.

EDUCATION

2019-2023 PhD in Mechanical Engineering
Delft University of Technology, Delft, the Netherlands
Thesis: Nonlinear mechanics of suspended ultra-thin membranes
Promotors: Prof. dr. P. G. Steeneken & Dr. F. Alijani

2015-2017 MSc in Mechanical Engineering
Amirkabir University of Technology, Tehran, Iran
MSc thesis: Nonlinear vibration analysis of cylindrical nanoshells including surface free energy effects
Supervisor: Prof. dr. M. M. Aghdam

2011-2015 B.Sc. in Aerospace Engineering
Sharif University of Technology, Tehran, Iran
BSc thesis: Analysis of elastomeric expansion joints
Supervisor: Dr. R. D. Firouz-abadi

EXPERIENCE

2024-Present Quantitative Risk Analyst (Data Scientist)
ABN AMRO Bank N.V., Amsterdam, the Netherlands

2017- 2019 Research Assistant
Amirkabir University of Technology, Tehran, Iran

2015 Mechanical Analysis Engineer (Internship)
Havakhorshid Institute - Ferdowsi University of Mashhad, Iran

LIST OF PUBLICATIONS

JOURNAL ARTICLES

6. P. Belardinelli, E. R. Hernandez, **A. Sarafraz**, F. Alijani, *Temperature dependence of energy transfer between vibrational modes in CNTs*, Research ongoing.

5. **A. Sarafraz**, F. Alijani, *Temperature-dependent nonlinear damping in a graphene Nosé-Hoover resonator*, Manuscript under preparation.

4. Z. Li, F. Alijani, **A. Sarafraz**, M. Xu, R. Norte, M.A. Aragorn, P.G. Steeneken, *Finite Element-based Nonlinear Dynamic Optimization of Nanomechanical Resonators*, Microsystems & Nanoengineering, 11(1), p.16 (2025).

3. **A. Sarafraz**, H. Liu, K. Cvetanović, M. Spasenović, S. Vollebregt, T.M. Garcia, P.G. Steeneken, F. Alijani, G.J. Verbiest, *Quantifying stress distribution in ultra-large graphene drums through mode shape imaging*, npj 2D Materials and Applications, 8(1), p.45 (2024).

2. **A. Sarafraz**, A. Givois, I.E. Rosłoń, H.Liu, H.Brahmi, G.Verbiest, P.G.Steeneken, and F.Alijani, *Pressure-induced nonlinear resonance frequency changes for extracting Young's modulus of nanodrums*, Nonlinear Dynamics 111, 14751–14761 (2023).

1. **A. Sarafraz**, H. Arjmandi-Tash, L. Dijkink, B. Sajadi, M. Moeini, P.G. Steeneken, F. Alijani, *Nonlinear elasticity of wrinkled atomically thin membranes*, Journal of Applied Physics 130, (18) (2021).